

Springer Theses

Recognizing Outstanding Ph.D. Research

Matthias Maasch

Tunable Microwave Metamaterial Structures



Springer

Springer Theses

Recognizing Outstanding Ph.D. Research

Aims and Scope

The series “Springer Theses” brings together a selection of the very best Ph.D. theses from around the world and across the physical sciences. Nominated and endorsed by two recognized specialists, each published volume has been selected for its scientific excellence and the high impact of its contents for the pertinent field of research. For greater accessibility to non-specialists, the published versions include an extended introduction, as well as a foreword by the student’s supervisor explaining the special relevance of the work for the field. As a whole, the series will provide a valuable resource both for newcomers to the research fields described, and for other scientists seeking detailed background information on special questions. Finally, it provides an accredited documentation of the valuable contributions made by today’s younger generation of scientists.

Theses are accepted into the series by invited nomination only and must fulfill all of the following criteria

- They must be written in good English.
- The topic should fall within the confines of Chemistry, Physics, Earth Sciences, Engineering and related interdisciplinary fields such as Materials, Nanoscience, Chemical Engineering, Complex Systems and Biophysics.
- The work reported in the thesis must represent a significant scientific advance.
- If the thesis includes previously published material, permission to reproduce this must be gained from the respective copyright holder.
- They must have been examined and passed during the 12 months prior to nomination.
- Each thesis should include a foreword by the supervisor outlining the significance of its content.
- The theses should have a clearly defined structure including an introduction accessible to scientists not expert in that particular field.

More information about this series at <http://www.springer.com/series/8790>

Matthias Maasch

Tunable Microwave Metamaterial Structures

Doctoral Thesis accepted by
Technische Universität Darmstadt, Germany

Author

Dr. Matthias Maasch
Terahertz Sensors Group
Department of Electrical Engineering
and Information Technology
Technische Universität Darmstadt
Darmstadt
Germany

Supervisor

Prof. Christian Damm
Department of Electrical Engineering
and Information Technology
Technische Universität Darmstadt
Darmstadt
Germany

ISSN 2190-5053

Springer Theses

ISBN 978-3-319-28178-0

DOI 10.1007/978-3-319-28179-7

ISSN 2190-5061 (electronic)

ISBN 978-3-319-28179-7 (eBook)

Library of Congress Control Number: 2015958545

© Springer International Publishing Switzerland 2016

This work is subject to copyright. All rights are reserved by the Publisher, whether the whole or part of the material is concerned, specifically the rights of translation, reprinting, reuse of illustrations, recitation, broadcasting, reproduction on microfilms or in any other physical way, and transmission or information storage and retrieval, electronic adaptation, computer software, or by similar or dissimilar methodology now known or hereafter developed.

The use of general descriptive names, registered names, trademarks, service marks, etc. in this publication does not imply, even in the absence of a specific statement, that such names are exempt from the relevant protective laws and regulations and therefore free for general use.

The publisher, the authors and the editors are safe to assume that the advice and information in this book are believed to be true and accurate at the date of publication. Neither the publisher nor the authors or the editors give a warranty, express or implied, with respect to the material contained herein or for any errors or omissions that may have been made.

Printed on acid-free paper

This Springer imprint is published by SpringerNature

The registered company is Springer International Publishing AG Switzerland

Parts of this thesis have been published in the following journal articles:

Journal Contributions

C. Damm, M. Maasch, M. Schüßler, and R. Jakoby, "Double Series and Double Parallel Unit Cells for Transmission Line Metamaterials," *Electronics Letters*, vol. 46, no. 2, pp. 112–113, Jan. 2010.

M. Gil, C. Damm, M. Sazegar, M. Maasch, A. Giere, M. Schuessler, F. Aznar, A. Velez, J. Bonache, R. Jakoby, and F. Martin, "Tunable Sub-Wavelength Resonators based on Barium-Strontium-Titanate Thick-Film Technology," *IET Microwaves, Antennas & Propagation*, vol. 5, no. 3, pp. 316–323, Feb 2011.

M. Puentes, M. Maasch, M. Schüßler, and R. Jakoby, "Frequency Multiplexed 2-Dimensional Sensor Array based on Split-Ring Resonators for Organic Tissue Analysis," *IEEE Transactions on Microwave Theory and Techniques*, vol. 60, no.6, pp. 1720–1727, June 2012.

M. Roig, M. Maasch, C. Damm, and R. Jakoby, "Liquid Crystal-based Tunable CRLH-Transmission Line for Leaky Wave Antenna Applications at Ka-Band," *International Journal of Microwave and Wireless Technologies*, vol. 6, Special Issue 3–4, pp 325–330, June 2014.

M. Maasch, M. Roig, C. Damm, and R. Jakoby, "Voltage Tunable Artificial Gradient-Index Lens based on a Liquid Crystal Loaded Fishnet Metamaterial," *IEEE Antennas and Wireless Propagation Letters*, vol.13, pp. 1581–1584, 2014.

Conference and Workshop Contributions

M. Maasch, C. Damm, M. Schüßler, and R. Jakoby, "Electrically Controllable Double Series (DS) Line with Left- or Right-Handed Propagation," in *39th European Microwave Conference (EuMC)*, 2009, pp. 516–519, 29 Sept. 29–1 Oct. 2009.

C. Damm, M. Maasch, R. Gonzalo, and R. Jakoby, "Tunable Composite Right/Left-Handed Leaky Wave Antenna based on a Rectangular Waveguide using Liquid Crystals," in *IEEE MTT-S International Microwave Symposium Digest (MTT)*, 2010, 23–28 May 2010.

M. Maasch, C. Damm, E. González-Rodríguez, and R. Jakoby, "Measurement Setup for Effective Material Parameter Extraction of DC Biased Artificial Material Structures," in *41st European Microwave Conference (EuMC)*, 2011, pp. 357–360, 10–13 Oct. 2011.

M. Maasch, C. Damm, M. Schüßler, E. González-Rodríguez, and R. Jakoby, "Varactor Loaded Tunable Split Ring Resonators with Simple Biasing Network," in *German Microwave Conference (GeMIC)*, 2011, March 2011.

M. Maasch, O. Karabey, C. Damm, M. Roig, and R. Jakoby, "Investigation on the Beam-Scanning Capability of a Gradient Index Fishnet Structure," in *IEEE Antennas and Propagation Society International Symposium (APSURSI)*, 2012, pp. 1–2, 8–14 July 2012.

M. Maasch, A. Groudass, O. H. Karabey, C. Damm, and R. Jakoby, "Electrically Tunable Open Split-Ring Resonators based on Liquid Crystal Material," in *6th International Congress on Advanced Electromagnetic Materials in Microwaves and Optics (METAMATERIALS)*, 2012, 17–20 Sept. 2012.

M. Maasch, M. Roig, C. Damm, and R. Jakoby, "Planar Metamaterial with Separately Voltage Tunable Electric and Magnetic Dispersion based on Liquid Crystal," in *7th International Congress on Advanced Electromagnetic Materials in Microwaves and Optics (METAMATERIALS)*, 2013, pp. 556–559, 16–21 Sept. 2013.

M. Maasch, M. Roig, C. Damm, and R. Jakoby, "Efficient Farfield Computation from Eigenmode Simulations for Leaky-Wave Antennas," in *IEEE Antennas and Propagation Society International Symposium (APSURSI)*, 2013, pp. 1656–1657, 7–13 July 2013.

M. Maasch, M. Roig, C. Damm, and R. Jakoby, "Realization of a Voltage Tunable Gradient-Index Fishnet Loaded with Liquid Crystal," in *8th International Congress on Advanced Electromagnetic Materials in Microwaves and Optics (METAMATERIALS)*, 2014, pp. 196–198, 25–28 Aug. 2014.

Supervisor's Foreword

I have the honor to introduce Dr.-Ing. Matthias Maasch, who worked with great success on his Ph.D. thesis under my guidance in the field of tunable metamaterials. Dr. Maasch was born in 1980 in Herzberg/Elster, Germany. After his professional training as communications and radio technician, he studied Electrical Communication Engineering at the Hochschule Mannheim, where he received the Dipl.-Ing. (FH) degree in July 2007 as the best student of the semester. He decided to start working on his Ph.D. thesis at the Technische Universität Darmstadt and obtained a one-year qualification scholarship from the German Research Foundation (DFG) to prepare for his Ph.D. thesis. Thereafter he received a 3-year DFG scholarship meant to foster excellent Ph.D. candidates within the graduate school GRK 1037 TICMO coordinated by Prof. Jakoby at the Technische Universität Darmstadt, Institute of Microwave Engineering and Photonics, where he worked under my guidance on tunable microwave metamaterial structures. After an excellent Ph.D. defense with the highest possible mark *summa cum laude* in December 2014 he continued his work in my group as postdoc.

The presented thesis is a well-balanced mixture of theory and experiments. It deals with fundamental concepts and practical realizations of tunable microwave components based on metamaterials and liquid crystals. Possible applications are tunable components like filters, matching networks, antennas, and general beam forming devices for communication applications. Future mobile communication with strongly increasing data rates on multiple frequency bands and increasing operation frequencies will require more and more reconfigurable and tunable components. A simple example is an antenna with beam steering capabilities, where the beam can follow a moving end user to ensure a high signal quality and high data rate. Known approaches for such beam steering are not satisfying, especially not for higher frequencies, e.g., for 60 GHz future Wi-Fi applications. The presented work demonstrates several promising solutions for this problem which are enabled by the combination of the two new concepts of metamaterials and liquid crystals for electric tuning and reconfiguration.

The original contribution with the highest impact is to my humble opinion the design and demonstration of the electrically tunable gradient-index lens based on liquid crystals, which to the best of my knowledge has not been shown by anybody else before. The candidate demonstrates impressively the mastery of numerous scientific methods for the well-directed development of liquid crystal-based tunable components using fishnet unit cells as metamaterial building block. A beam steering of $\pm 5^\circ$ is already demonstrated with the built prototype, and a way to overcome the present angular steering limitation using a Fresnel lens approach is provided and confirmed by simulations, enabling beam steering of nearly $\pm 90^\circ$. This original contribution is of great value due to the inherent suitability of the fishnet approach combined with liquid crystal technology for mm- and even THz-wave applications. For the future market of mobile communication with ever-increasing transfer rates and operation frequencies, the developed concept seems a unique solution for beam steering and beam forming applications. Both the presented concept and the developed method of far-field calculation have the potential to pave the way for these new agile communication system components.

Darmstadt
October 2015

Prof. Christian Damm

Acknowledgments

This dissertation is the result of my time as doctoral student at the Institute for Microwave Engineering and Photonics at Technische Universität Darmstadt. Since such a work would not have been possible without the support and guidance of colleagues and partners, I would like to thank those people who contributed to this work.

First and foremost, I would like to express my gratitude toward my supervisor Prof. Dr.-Ing. Christian Damm for the trust placed in me and the continuous support of my research. Furthermore, I would like to thank Prof. Ferran Martín for taking over the co-examination of my work. Besides, I would like to thank Prof. Dr.-Ing. Rolf Jakoby for the encouragement and support during my time in his research group, particularly during my qualification year.

My sincere thanks goes to my colleagues at the Institute for Microwave Engineering and Photonics, in particular Dr.-Ing. María Roig Parras, Dr.-Ing. Erick González Rodríguez, but also Dr.-Ing. Margarita Puentes, Dr.-Ing. Holger Maune, and Dr.-Ing. Martin Schüßler for the fruitful scientific discussions but also for sharing enjoyable experiences beyond the scientific activities. Furthermore, I would like to thank Peter Kießlich, Andreas Semrad, and Karin Boye for their support concerning the practical aspects of my work.

Finally, I would like to thank my family for their support, especially my parents who always supported me on my chosen paths through life.

Darmstadt
October 2015

Matthias Maasch

Contents

1	Introduction	1
	References	3
2	Wave Propagation in Periodic Structures	7
2.1	Material Parameters of Distributed Periodic Structures	7
2.2	Dispersion Functions and Transmission Line Model	9
2.3	Causality and Its Consequences on Dispersion	14
2.3.1	Application to Different Unit Cell Configurations	17
2.3.2	Kramers–Kronig Relation for Phase Reconstruction	22
2.4	Effective Material Parameters of Discrete Periodic Structures	24
	References	33
3	Implementation of Three-Dimensional Lorentz-Drude-Materials	35
3.1	Wire Lattice	35
3.2	Split-Ring Resonator	38
3.3	Hollow Waveguides	43
	References	46
4	Extraction of Dispersion Parameters	49
4.1	Extraction from Scattering Parameters	49
4.1.1	Nicolson–Ross–Weir Extraction Method with Phase Reconstruction	49
4.1.2	Consideration of Higher Order Modes in Scattering Parameters	53
4.1.3	Eigenmode Determination from Simulated Scattering Parameters	57
4.2	Fullwave Eigenmode Computation	59
4.2.1	Bloch Impedance Extraction by Field Averaging	59
4.2.2	Farfield Computation from Eigenmode Results	63
	References	71

5 Tunable Transmission Line Metamaterials	73
5.1 Tunable Double Series Transmission Line.	74
5.2 Liquid Crystals for Voltage Tunable Components	80
5.3 Tunable Artificial Transmission Line Using Liquid Crystal	83
5.4 Tunable Open Split-Ring Resonator	88
References	92
6 Artificial Gradient-Index Lens	95
6.1 Gradient-Index Structures for Beam Scanning	95
6.2 Tunable Split-Ring Resonator	98
6.3 Tunable Omega Resonator	105
6.4 Tunable Fishnet Structure	111
6.4.1 Static Gradient-Index Fishnet Structure.	114
6.4.2 Voltage Tunable Gradient-Index Fishnet Structure	121
References	126
7 Conclusion and Outlook.	129
Appendix	133

About the Author



Matthias Maasch was born in Herzberg/Elster, Germany in 1980. After his professional training as Communications and Radio Technician, he studied Electrical Communication Engineering at Hochschule Mannheim, where he received the Dipl. Ing. (FH) degree in 2007. After a DFG scholarship within the graduate school GRK 1037 TICMO and working as a research assistant at Technische Universität Darmstadt, Institute for Microwave Engineering and Photonics, he received the Dr.-Ing. degree with *summa cum laude* from Technische Universität Darmstadt in 2014. His current research activities focus on the

design of tunable microwave metamaterials for antenna applications as well as on terahertz sensors for biomedical analysis and process and environmental monitoring.

Symbols

\mathbf{a}_i	Normalized incident power wave
\mathbf{A}	Chain parameter matrix
AF	Array factor
α	Attenuation constant
\mathbf{b}_i	Normalized reflected power wave
\mathbf{B}	Magnetic flux density
β	Phase constant
C, C'	Capacitance, capacitance normalized to unit length
c_0	Speed of light in vacuum: $c_0 \approx 299.792 \cdot 10^6$ m/s
χ_m, χ_e	Complex magnetic, electric susceptibility
\mathbf{D}	Electric flux density
D	Antenna directivity
$\delta_\mu, \delta_\varepsilon$	Magnetic, electric damping frequency of the Lorentz/Drude dispersion model
\mathbf{E}	Electric field strength
e	Charge of an electron $e \approx 1.602 \cdot 10^{-19}$ C
ε_0	Vacuum permittivity: $\varepsilon_0 \approx 8.854 \cdot 10^{-12}$ F/m
$\varepsilon, \varepsilon_{\text{eff}}, \tilde{\varepsilon}$	Complex permittivity, effective permittivity, permittivity of a continuous material
$\bar{\varepsilon}$	Complex permittivity tensor of an anisotropic material
$\varepsilon_{r,\text{LC}\parallel}, \varepsilon_{r,\text{LC}\perp}$	Relative parallel, vertical permittivity of liquid crystal
ϵ	Relative error
η_0	Vacuum wave impedance: $\eta_0 \approx 376.73 \Omega$
\mathbf{f}	Plane wave spectrum
f	Frequency
$\mathcal{F}\{\}$	Fourier transform
Φ	Magnetic flux
ϕ	Phase shift
G, G'	Conductance, conductance normalized to unit length

γ	Complex propagation constant
H	Magnetic field strength
$\mathcal{H}\{\}$	Hilbert transform
HPBW	Half-power beam width
I	Current
j	Imaginary unit
J_n	n -th order Bessel function
k , k	Complex wavevector, complex wavenumber
k_x, k_y, k_z	x, y, z component of the wavevector
k_0	Wavenumber in vacuum
\tilde{k}	Complex wavenumber in a continuous material
L, L'	Inductance, inductance normalized to unit length
λ	Wavelength
m_e	Mass of an electron: $m_e \approx 9.109 \cdot 10^{-31}$ kg
M	Magnetic polarization
M	Mutual inductance
μ_0	Vacuum permeability: $\mu_0 \approx 1.257 \cdot 10^{-6}$ H/m
$\mu, \mu_{\text{eff}}, \tilde{\mu}$	Complex permeability, effective permeability, permeability of a continuous material
$\bar{\mu}$	Complex permeability tensor of an anisotropic material
n	Director
N_m, N_e	Number of molecules per unit volume, number of electrons per volume
ω	Angular frequency
$\omega_{0\mu}, \omega_{0\varepsilon}$	Angular magnetic, electric resonance frequency of the Lorentz dispersion model
$\omega_{t\mu}, \omega_{t\varepsilon}$	Angular magnetic, electric transition frequency of the Lorentz dispersion model
$\omega_{p\mu}, \omega_{p\varepsilon}$	Angular magnetic, electric plasma frequency of the Drude dispersion model
P	Electric polarization
P	Power
ψ	Radiation direction
R, R'	Resistance, resistance normalized to unit length
S	Poynting vector or scattering parameter matrix
\bar{S}	Time averaged Poynting vector
S	Magnetic coupling factor, orientational order parameter
S_ϵ	Normalized mean squared error
σ	Electric conductivity
T	Scattering transfer matrix
t	Time
V	Voltage
v_p, v_g, v_e	Velocity of phase, group, energy
ξ	Magnetoelectric coupling

Y	Admittance parameter matrix
Y'	Complex admittance normalized to unit length
Z	Impedance parameter matrix
Z_B, Z_w, Z_c	Complex Bloch impedance, complex wave impedance of a homogenous material, complex characteristic impedance of a transmission line
Z'	Complex impedance normalized to unit length
Z_0	Complex reference impedance of a two-port network

Chapter 1

Introduction

Metamaterials are artificial, engineered materials consisting of periodic arrangements of sub-wavelength unit cells, whose electromagnetic properties are primarily determined by their structure. Such artificially fabricated particles are able to generate an electromagnetic response that can be tailored independently for the electric and magnetic component of a wave. Hence, a periodic arrangement of these particles can be treated as an effective material described by a set of material parameters. This allows to create electromagnetic responses at a desired frequency that are not possible with naturally available materials. For example, at microwave frequencies the variety of magnetic materials is very limited. However, a magnetic response can be mimicked by using periodic arrangements of metallic rings.

The description of artificial materials or artificial dielectrics by use of the effective refractive index has been established by Kock when designing radio frequency (RF) lenses consisting of metal stripes [1]. A first description of the effective material parameters of wire lattices with negative effective permittivity (artificial plasmas) has been done by Rotman [2]. In 1968, Veselago [3] theoretically considered double-negative materials with simultaneously negative permeability and permittivity exhibiting a negative phase velocity. Although this is physically possible, no natural material with a negative permeability and permittivity at the same frequency exists. After 30 years, the topic has been revised by Pendry et al. [4, 5] by characterizing the RF response of lattices of wires and rings. These works were the basis for the first experimentally confirmed medium with simultaneously negative effective permittivity and permeability by Smith et al. [6].

Direct manipulation of non-guided waves can be realized with three-dimensional metamaterials. The two basic elements for non-planar metamaterials are wires and split-ring resonators. A wire lattice parallel to the electric field component of an incident plane wave creates a Drude or Lorentz response for the effective permittivity [4] while split-ring resonators perpendicular to the magnetic field component create a Lorentz response for the effective permeability [5]. These elements are the basis for configurations that can be fabricated at microwave frequencies and with variations up to optical frequencies. With parallel gold nanorods [7] or the fishnet [8, 9], a double-negative response has been demonstrated in the infrared region.

These three-dimensional unit elements allow the implementation of gradient-index metamaterials [10] and complex electromagnetic transformations like cloaking [11] or beam steering [12]. By exploiting voltage tunable materials and components, the spatial distribution of effective material parameters can be reconfigured. With this, artificial lenses with a tunable phase response, e.g. to change the focal point or the radiation direction, can be implemented. Since the electric and magnetic response can be manipulated independently of each other, the phase distribution of a gradient-index metamaterial can be tuned while keeping its impedance constant. Very promising for the implementation of such tunable metamaterials are liquid crystal materials since investigations of dedicated microwave mixtures have shown suitable properties in terms of tunability and losses for frequencies up to at least 4 THz [13, 14].

Manipulation of guided waves is possible with transmission line metamaterials [15–17], where dispersion characteristics can be tailored by loading a host transmission line with lumped elements. Applications of non-resonant transmission line metamaterials include leaky-wave antennas [18, 19], small antennas [20], phase shifters [21, 22], and delay lines [23, 24]. By loading the host transmission line with resonant structures such as split-ring resonators and its variations, miniaturized components like compact filters [25–27] and phase shifters [28] can be realized.

A general aim of the metamaterial theory is the use of dispersion parameters such as effective material parameters, or wavenumber and Bloch impedance to describe the response of a periodic arrangement of unit cells to an incident wave. These dispersion parameters are obtained from the geometry of a single unit cell. One reason for that is to increase the simulation efficiency: often, the electromagnetic simulation of a large, three-dimensional configuration which consists of unit cells with a high level of details is time consuming or even impossible due to computational constraints. Based on the analysis of scattered waves or on the determination of propagating eigenmodes and the corresponding field distribution, different methods exist to predict the response of a complex array from the simulation of a single unit cell. Furthermore, since the electromagnetic response of a unit cell and periodic array is described by a set of dispersion parameters and not by the local distribution of electric and magnetic fields inside the unit cell, concepts like transmission line transformation can be applied independent of the actual physical implementation of the unit cell. However, effects like spatial dispersion and higher order mode propagation have to be taken into account.

In this work, the concept of metamaterials, where the wave propagation in periodic lattices is described by a set of dispersion parameters, is applied to design voltage tunable microwave components. These include artificial transmission lines with tunable properties for applications such as phase shifters, filters, and planar leaky-wave antennas. Furthermore, voltage tunable three-dimensional unit cells for free-space applications are designed. Their applicability is demonstrated with a tunable artificial gradient-index lens which permits an adaptive scanning of an incident beam. Aspects such as impact of discretization or physical realizability are considered and their effect on the dispersion properties is investigated for general discrete periodic configurations. Due to the large simulation effort for large arrays with small geometrical

details, methods for prediction of large arrays based on the simulation of a single unit cell are presented and compared with existing methods.

Thesis Outline

In the present work, tunable transmission line metamaterials and three-dimensional metamaterial configurations for microwave frequencies are designed, investigated, and manufactured. In Chap. 2, the connection between wave propagation in conventional materials and periodic structures is demonstrated and transmission line models for different dispersion models are derived. Furthermore, the impact of physical restrictions such as causality and a finite unit cell size are considered for the transmission line model and dispersion parameters.

In Chap. 3, implementations of three dimensional metamaterials and their unit cell configurations are presented. The investigated particles are continuous and cut wires as well as split-ring resonators. Additionally, the transmission line circuit to describe the propagation of different modes in rectangular hollow waveguides is derived.

Since it is desired to describe periodic structures with dispersion parameters like wavenumber and Bloch impedance or with effective material parameters, Chap. 4 introduces different methods for the extraction of these parameters from arbitrary geometries and circuits. These methods are based on the simulation of scattering parameters for one or multiple modes, or on the field distribution of propagating eigenmodes. Furthermore, a farfield prediction method, that uses the eigenmode field distribution to obtain detailed information about the radiation properties, is derived.

In Chap. 5, different voltage tunable transmission line metamaterials are outlined. The concept of artificial transmission lines with tunable properties is demonstrated by employing semiconductor varactors as well as liquid crystal varactors. Furthermore, an artificial transmission line with independently voltage tunable electric and magnetic response in the Ka-band is demonstrated.

Consequently, in Chap. 6, the previously set out principles are used to design and implement voltage tunable artificial lenses for beam scanning applications. Voltage tunability is applied to different three-dimensional metamaterial geometries and their properties are investigated. Finally, a voltage tunable fishnet metamaterial infiltrated with liquid crystal and its beam scanning capabilities are demonstrated in the Ka-band.

The presented thesis is finalized with a conclusion of the work and its results followed by an outlook to future research based on the presented results.

References

1. W. Kock, Metal-lens antennas. *Proc. IRE* **34**, 828–836 (1946)
2. W. Rotman, Plasma simulation by artificial dielectrics and parallel-plate media. *IRE Trans. Antennas Propag.* **10**, 82–95 (1962)
3. V.G. Veselago, The electrodynamics of substances with simultaneously negative values of ϵ and μ . *Soviet Physics Uspekhi* **10**(4), 509 (1968)

4. J.B. Pendry, A.J. Holden, D.J. Robbins, W.J. Stewart, Low frequency plasmons in thin-wire structures. *J. Phys. Condens. Matter* **10**(22), 4785 (1998)
5. J. Pendry, A. Holden, D. Robbins, W. Stewart, Magnetism from conductors and enhanced nonlinear phenomena. *IEEE Trans. Microw. Theory Tech.* **47**, 2075–2084 (1999)
6. D.R. Smith, W.J. Padilla, D.C. Vier, S.C. Nemat-Nasser, S. Schultz, Composite medium with simultaneously negative permeability and permittivity. *Phys. Rev. Lett.* **84**, 4184–4187 (2000). May
7. V.M. Shalaev, W. Cai, U.K. Chettiar, H.-K. Yuan, A.K. Sarychev, V.P. Drachev, A.V. Kildishev, Negative index of refraction in optical metamaterials. *Opt. Lett.* **30**, 3356–3358 (2005)
8. S. Zhang, W. Fan, N.C. Panoiu, K.J. Malloy, R.M. Osgood, S.R.J. Brueck, Experimental demonstration of near-infrared negative-index metamaterials. *Phys. Rev. Lett.* **95**, 137404 (2005). Sep
9. S. Zhang, W. Fan, K.J. Malloy, S. Brueck, N.C. Panoiu, R.M. Osgood, Near-infrared double negative metamaterials. *Opt. Express* **13**, 4922–4930 (2005). Jun
10. D.R. Smith, J.J. Mock, A.F. Starr, D. Schurig, Gradient index metamaterials. *Phys. Rev. E* **71**, 036609 (2005)
11. D. Schurig, J.J. Mock, B.J. Justice, S.A. Cummer, J.B. Pendry, A.F. Starr, D.R. Smith, Metamaterial electromagnetic cloak at microwave frequencies. *Science* **314**(5801), 977–980 (2006)
12. H. Chen, L. Ran, J. Huangfu, T.M. Grzegorzczuk, J.A. Kong, Equivalent circuit model for left-handed metamaterials. *J. Appl. Phys.* **100**(2), 024915 (2006)
13. C. Weickhmann, R. Jakoby, E. Constable, R. Lewis, Time-domain spectroscopy of novel nematic liquid crystals in the terahertz range, in *2013 38th International Conference on Infrared, Millimeter, and Terahertz Waves (IRMMW-THz)*, pp. 1–2, Sept 2013
14. R. Dudley, M. Naftaly, Thz optical constants of liquid crystals bl037 and gt3-23001, in *Millimeter Waves and THz Technology Workshop (UCMMT), 2013 6th UK, Europe, China*, pp. 1–2 Sept 2013
15. C. Caloz T. Itoh, Application of the transmission line theory of left-handed (lh) materials to the realization of a microstrip “lh line”, in *Antennas and Propagation Society International Symposium, 2002. IEEE*, vol. 2, pp. 412–415 (2002)
16. A.A. Oliner, A periodic-structure negative-refractive-index medium without resonant elements. *IEEE-APS/URSI Int’l Symp. Digest* **41**, 2002 (2002)
17. G. Eleftheriades, A. Iyer, P. Kremer, Planar negative refractive index media using periodically l-c loaded transmission lines. *IEEE Trans. Microw. Theory Tech.* **50**, 2702–2712 (2002)
18. L. Liu, C. Caloz, T. Itoh, Dominant mode leaky-wave antenna with backfire-to-endfire scanning capability. *Electron. Lett.* **38**, 1414–1416 (2002)
19. C. Allen, C. Caloz, T. Itoh, Leaky-waves in a metamaterial-based two-dimensional structure for a conical beam antenna application. *2004 IEEE MTT-S Int. Microw. Symp. Dig.* **1**, 305–308 (2004)
20. M. Schler, C. Damm, J. Freese, R. Jakoby, Realization concepts for compact microstrip antennas with periodically loaded lines, in *Proceedings of IEEE MTT-S International Microwave Symposium Digest*, p. 4 (2005)
21. M. Antoniadis, G. Eleftheriades, Compact, linear, lead/lag phase shifters using negative refractive index metamaterials, in *IEEE Antennas and Propagation Society International Symposium, 2003*, vol. 3, pp. 367–370 (2003)
22. C. Damm, M. Schler, M. Oertel, R. Jakoby, Compact tunable periodically lc loaded microstrip line for phase shifting applications, in *Proceedings of IEEE MTT-S International Microwave Symposium Digest*, p. 4 (2005)
23. M. Schler, C. Damm, R. Jakoby, Periodically lc loaded lines for rfid backscatter applications, in *Proceedings of the 1st Metamaterial Conference, Rome, Italy* (2007)
24. M. Schler, C. Damm, M. Maasch, R. Jakoby, Performance evaluation of left-handed delay lines for rfid backscatter applications, in *Proceedings of IEEE MTT-S International Microwave Symposium Digest*, pp. 177–180 (2008)
25. J. Bonache, I. Gil, J. Garca-Garca, F. Martn, Novel microstrip bandpass filters based on complementary split-ring resonators. *IEEE Trans. Microw. Theory Tech.* **54**, 265–271 (2006)

26. I. Gil, J. Garca-Garca, J. Bonache, F. Martn, M. Sorolla, R. Marqus, Varactor-loaded split ring resonators for tunable notch filters at microwave frequencies. *Electron. Lett.* **40**, 1347–1348 (2004)
27. I. Gil, J. Bonache, J. Garca-Garca, F. Martn, Tunable metamaterial transmission lines based on varactor-loaded split-ring resonators. *IEEE Trans. Microw. Theory Tech.* **54**, 2665–2674 (2006)
28. A. Vlez, J. Bonache, F. Martn, Metamaterial transmission lines with tunable phase and characteristic impedance based on complementary split ring resonators. *Microw. Opt. Tech. Lett.* **51**(8), 1966–1970 (2009)

Chapter 2

Wave Propagation in Periodic Structures

Wave propagation in periodic structures is closely related to propagation of waves in continuous media. Thus, dispersion parameters such as wavenumber and wave impedance or permeability and permittivity, can be used to describe the propagation of waves in one-dimensional periodic structures like loaded or artificial transmission lines and waveguides, and in two- and three-dimensional structures like artificial lenses, transmit arrays and meta surfaces. In this chapter, the connection between transmission line theory and effective material parameters, that can be used to describe the propagation of waves in periodic lattices, is investigated. Furthermore, based on a general form of a transmission line model and effective material parameters, a physical limitation for dispersion characteristics and corresponding equivalent circuit are derived. Finally, the effect of discretization and finite unit cell size in periodic structures on effective material parameters is considered.

2.1 Material Parameters of Distributed Periodic Structures

The propagation of a wave in a charge free material can be described by Maxwell's equations which in the frequency domain are [1]

$$\int_{\partial A} \mathbf{E}(\mathbf{r}, \omega) d\mathbf{s} = - \int_A j\omega \mathbf{B}(\mathbf{r}, \omega) d\mathbf{A} \Leftrightarrow \text{rot } \mathbf{E}(\mathbf{r}, \omega) = -j\omega \mathbf{B}(\mathbf{r}, \omega), \quad (2.1)$$

$$\int_{\partial A} \mathbf{H}(\mathbf{r}, \omega) d\mathbf{s} = \int_A j\omega \mathbf{D}(\mathbf{r}, \omega) d\mathbf{A} \Leftrightarrow \text{rot } \mathbf{H}(\mathbf{r}, \omega) = j\omega \mathbf{D}(\mathbf{r}, \omega), \quad (2.2)$$

$$\int_{\partial V} \mathbf{D}(\mathbf{r}, \omega) d\mathbf{A} = 0 \Leftrightarrow \text{div } \mathbf{D}(\mathbf{r}, \omega) = 0, \quad (2.3)$$

$$\int_{\partial V} \mathbf{B}(\mathbf{r}, \omega) d\mathbf{A} = 0 \Leftrightarrow \text{div } \mathbf{B}(\mathbf{r}, \omega) = 0 \quad (2.4)$$

with the material equations of a linear material

$$\mathbf{B}(\omega) = \mu_0 [\mathbf{M}(\omega) + \mathbf{H}(\omega)] = \mu_0 [\bar{\chi}_m(\omega) + 1] \mathbf{H}(\omega) = \bar{\mu}(\omega) \mathbf{H}(\omega), \quad (2.5)$$

$$\mathbf{D}(\omega) = \varepsilon_0 \mathbf{E}(\omega) + \mathbf{P}(\omega) = \varepsilon_0 [\bar{\chi}_e(\omega) + 1] \mathbf{E}(\omega) = \bar{\varepsilon}(\omega) \mathbf{E}(\omega). \quad (2.6)$$

Under the condition of an isotropic and homogeneous material, the material tensor $\bar{\mu}(\mathbf{r}, \omega)$ and $\bar{\varepsilon}(\mathbf{r}, \omega)$ reduce to scalar values and (2.1)–(2.4) can be combined to the Helmholtz equation

$$\begin{Bmatrix} \Delta \mathbf{E}(\mathbf{r}, \omega) \\ \Delta \mathbf{H}(\mathbf{r}, \omega) \end{Bmatrix} - k^2(\omega) \begin{Bmatrix} \mathbf{E}(\mathbf{r}, \omega) \\ \mathbf{H}(\mathbf{r}, \omega) \end{Bmatrix} = 0 \quad (2.7)$$

describing propagation in materials with the complex material properties μ and ε and the complex wavenumber

$$k(\omega) = \pm \omega \sqrt{\mu(\omega) \varepsilon(\omega)}. \quad (2.8)$$

The electric and magnetic field are related by the wave impedance Z_w so that

$$\mathbf{H}(\mathbf{r}, \omega) = \frac{1}{Z_w(\omega)} \cdot \frac{k}{|k|} \cdot \frac{\mathbf{S}}{|\mathbf{S}|} \times \mathbf{E}(\mathbf{r}, \omega) \quad (2.9)$$

with $\mathbf{S}/|\mathbf{S}|$ being the unit vector pointing in the direction of the energy flux of the wave. Hence, the wave impedance becomes

$$Z_w(\omega) = \pm \sqrt{\frac{\mu(\omega)}{\varepsilon(\omega)}}. \quad (2.10)$$

Similarly, the propagation of waves on a transmission line in z -direction is determined by [2]

$$\frac{\partial}{\partial z} \begin{Bmatrix} V(z, \omega) \\ I(z, \omega) \end{Bmatrix} - Z'_{se}(\omega) Y'_{sh}(\omega) \begin{Bmatrix} V(z, \omega) \\ I(z, \omega) \end{Bmatrix} = 0 \quad (2.11)$$

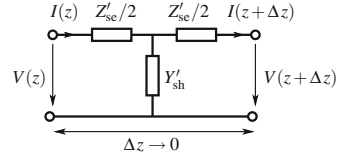
where the per unit length impedance and admittance Z'_{se} and Y'_{sh} are defined as in the equivalent circuit of an infinitesimal short transmission line section in Fig. 2.1. The propagation constant

$$\gamma = \alpha + j\beta = \pm \sqrt{Z'_{se}(\omega) Y'_{sh}(\omega)} \quad (2.12)$$

and the characteristic impedance

$$Z_c = \pm \sqrt{\frac{Z'_{se}(\omega)}{Y'_{sh}(\omega)}}. \quad (2.13)$$

Fig. 2.1 Infinitesimal short transmission line section



are used to describe the wave propagation on transmission lines.

Due to the equivalence between the wave equations and the impedance definition of the plane wave propagation and the propagation on the transmission line it can be defined

$$Z'_{se}(\omega) = \lim_{\Delta z \rightarrow 0} \frac{Z_{se}(\omega)}{\Delta z} = j\omega\mu_{\text{eff}}(\omega), \quad (2.14)$$

$$Y'_{sh}(\omega) = \lim_{\Delta z \rightarrow 0} \frac{Y_{sh}(\omega)}{\Delta z} = j\omega\varepsilon_{\text{eff}}(\omega), \quad (2.15)$$

i.e. the material parameters μ , ε and transmission line elements Z'_{se} , Y'_{sh} are mathematically equivalent [3, 4]. Since the resulting material parameters are not necessarily the parameters of an existing material, but describe the response of a periodic structure to the propagating electric and magnetic field of an arbitrary wave, they are denoted as effective material parameters μ_{eff} and ε_{eff} .

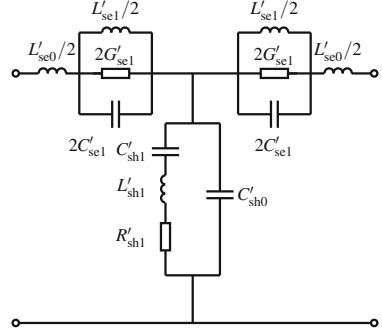
Propagation of a plane wave in a material can be described by the transmission line equivalent circuit in Fig. 2.1. On the other hand, wave propagation on a transmission line can be described by a wave propagating in an effective material with μ_{eff} and ε_{eff} . Hence, by adjusting the series impedance Z'_{se} and the shunt admittance Y'_{sh} , the frequency characteristic of the magnetic and electric response can be designed independently of each other for the case of a guided wave on a transmission line as well as for propagation of plane waves.

2.2 Dispersion Functions and Transmission Line Model

The Lorentz model, a damped mechanical oscillator model, represents an accurate description of lossy dielectric materials with resonant or relaxation effects, plasmas, or lossy metals and semiconductors with free charges. This classical quantum-mechanical dispersion model is based on the motion of electrons with the charge e and the mass m_e [1]

$$\varepsilon(\omega) = \varepsilon_0 \left(1 - \frac{N_m e^2}{\varepsilon_0 m_e} \sum_i \frac{A_i}{\omega^2 - \omega_{0\epsilon i}^2 - j\omega\delta_{\epsilon i}} \right), \text{ with } \sum_i A_i = N_e \quad (2.16)$$

Fig. 2.2 Transmission line model of a Lorentz–Lorentz material



where N_m is the number of molecules per unit volume with N_e electrons per molecule, ω_{0ei} is the resonance frequency, and δ_{ei} the collision frequency or damping factor.

Setting $\omega_{0e} = 0$ yields the Drude dispersion, e.g. of metals or plasmas with free electric charges [5]. On the contrary, the Debye dispersion where the collision frequency is in the range of the resonance frequency $\delta_e \approx \omega_{0e}$ describes relaxation effects, e.g. in dielectric or liquid materials [1]. The summation takes into account that a material can exhibit different resonance and relaxation effects based on different charges and their dipole moment. A material dispersion represented by the Lorentz equation is always causal since it is derived from a mechanical model that is per se causal [6].

With (2.14) and (2.15) it is possible to translate the Lorentz dispersion relation (2.16) into a transmission line model as in Fig. 2.1. For a single resonance of the permeability and permittivity, Fig. 2.2 shows a possible configuration of a transmission line model that yields a Lorentz dispersion for the effective permeability and permittivity. With (2.14) and (2.15), the effective material parameters become

$$\mu_{\text{eff}}(\omega) = \mu_{\infty} \frac{\omega^2 - \omega_{\mu}^2 - j\omega\delta_{\mu}}{\omega^2 - \omega_{0\mu}^2 - j\omega\delta_{\mu}}, \quad (2.17)$$

$$\varepsilon_{\text{eff}}(\omega) = \varepsilon_{\infty} \frac{\omega^2 - \omega_{\varepsilon}^2 - j\omega\delta_{\varepsilon}}{\omega^2 - \omega_{0\varepsilon}^2 - j\omega\delta_{\varepsilon}}, \quad (2.18)$$

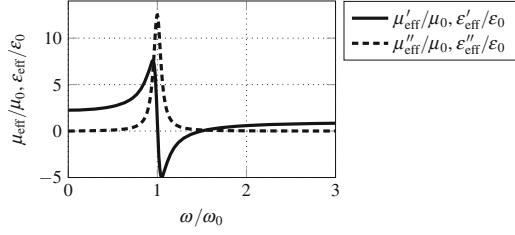
which is a rearranged form of (2.16) with a pole and a zero in the complex omega plane at

$$\omega_{\text{pole}} = j\frac{\delta}{2} \pm \sqrt{\omega_0^2 - \frac{\delta^2}{4}} \quad (2.19)$$

and

$$\omega_{\text{zero}} = j\frac{\delta}{2} \pm \sqrt{\omega_i^2 - \frac{\delta^2}{4}}. \quad (2.20)$$

Fig. 2.3 Effective material parameters of a Lorentz–Lorentz material



The resonance frequency ω_0 , the transition frequency ω_t , and the damping factor δ are determined by the element values:

$$\omega_{0\mu}^2 = \frac{1}{L'_{se1}C'_{se1}}, \quad \omega_{t\mu}^2 = \omega_{0\mu}^2 + \frac{1}{L'_{se0}C'_{se1}}, \quad \delta_\mu = \frac{G_{se1}}{C_{se1}}, \quad \mu_\infty = L'_{se0}, \quad (2.21)$$

$$\omega_{0\varepsilon}^2 = \frac{1}{L'_{sh1}C'_{sh1}}, \quad \omega_{t\varepsilon}^2 = \omega_{0\varepsilon}^2 + \frac{1}{L'_{sh1}C'_{sh0}}, \quad \delta_\varepsilon = \frac{R_{sh1}}{L_{sh1}}, \quad \varepsilon_\infty = C'_{sh0}. \quad (2.22)$$

Here, losses are assigned to the series capacitance C'_{se} and the shunt inductance L'_{sh} . However, losses in form of a series or parallel resistance can be added to each reactive element in the model which has an impact on the Lorentz parameters but not on the general dispersion equation.

Figure 2.3 shows the resulting complex effective material parameters for $\omega_t = 1.5\omega_0$ and $\delta = 0.1\omega_0$. At the resonance frequency ω_0 , due to the pole, the real part becomes very large with a change of the sign so that between the resonance and the transition frequency ω_t , the real part is negative. Furthermore, the imaginary part, i.e. the loss, has its maximum at the resonance frequency and stays significant in the negative region above the resonance frequency.

In the quantum-mechanical model described by (2.16), charges that are bound in the material, e.g. in a lattice, yield a resonance effect as in the Lorentz dispersion. If these charges are not bound but can move freely (only limited by losses, e.g. by collisions), the resonance frequency shifts to zero yielding the Drude dispersion model with

$$\mu_{\text{eff}}(\omega) = \mu_\infty \frac{\omega^2 - \omega_{p\mu}^2 - j\omega\delta_\mu}{\omega^2 - j\omega\delta_\mu}, \quad (2.23)$$

$$\varepsilon_{\text{eff}}(\omega) = \varepsilon_\infty \frac{\omega^2 - \omega_{p\varepsilon}^2 - j\omega\delta_\varepsilon}{\omega^2 - j\omega\delta_\varepsilon}. \quad (2.24)$$

It exhibits complex poles and zeros at

$$\omega_{\text{pole1}} = 0, \quad \omega_{\text{pole2}} = j\delta \quad (2.25)$$

Fig. 2.4 Transmission line model of a Drude–Drude material

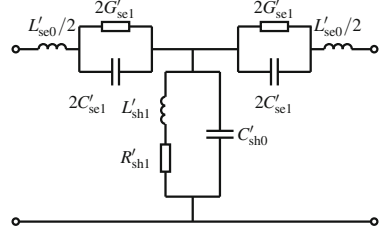
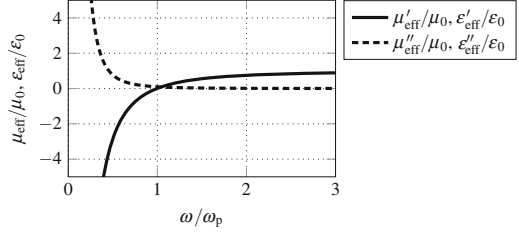


Fig. 2.5 Effective material parameters of a Drude–Drude material



and

$$\omega_{\text{zero}} = j \frac{\delta}{2} \pm \sqrt{\omega_p^2 - \frac{\delta^2}{4}}. \quad (2.26)$$

These dispersion properties can be translated into the transmission line model in Fig. 2.4 so that

$$\omega_{p\mu}^2 = \frac{1}{L'_{se0} C'_{se1}}, \quad \delta_\mu = \frac{G_{se1}}{C_{se1}}, \quad \mu_\infty = L'_{se0}, \quad (2.27)$$

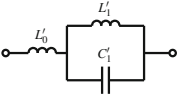
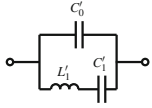
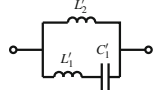
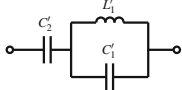
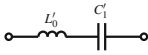
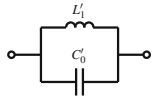
$$\omega_{p\epsilon}^2 = \frac{1}{L'_{sh1} C'_{sh0}}, \quad \delta_\epsilon = \frac{R_{sh1}}{L_{sh1}}, \quad \epsilon_\infty = C'_{sh0}. \quad (2.28)$$

For $\delta = 0.1\omega_p$, the effective material parameters are shown in Fig. 2.5. For frequencies below the plasma frequency ω_p , the real part is negative and continuously increasing while above ω_p it is positive. Compared to the Lorentz dispersion, the region of a negative real part is much wider due to the shift of the resonance frequency to zero. Furthermore, the loss is increasing for lower frequencies and has its maximum at zero.

The translation of the dispersion equation (2.16) into a transmission line model is not unambiguous if it exhibits one or more non-zero resonances or poles, i.e. the translation of (2.17) and (2.18) yields more than a single solution. Table 2.1 shows the series impedance Z'_{se} and shunt admittance Y'_{sh} for the lossless case¹ $\delta_\mu = \delta_\epsilon = 0$ to model the Lorentz and Drude dispersion with a transmission line model (2.16). It

¹Losses can be taken into account by adding a resistance to each necessary reactive element, yielding $\delta > 0$.

Table 2.1 Series and shunt branch impedances (without losses) which create a Drude and Lorentz dispersion

Dispersion model	series branch $Z'_{se} \rightarrow \mu_{\text{eff}}$	shunt branch $Y'_{sh} \rightarrow \epsilon_{\text{eff}}$
Lorentz: $\mu_{\text{eff}}, \epsilon_{\text{eff}} = A \frac{\omega^2 - \omega_0^2}{\omega^2 - \omega_p^2}$	 $A = L'_0$ $\omega_0^2 = \frac{1}{L'_1 C'_1}$ $\omega_p^2 = \omega_0^2 + \frac{1}{L'_0 C'_1}$	 $A = C'_0$ $\omega_0^2 = \frac{1}{L'_1 C'_1}$ $\omega_p^2 = \omega_0^2 + \frac{1}{L'_1 C'_0}$
	 $A = \frac{L'_1 L'_2}{L'_1 + L'_2}$ $\omega_0^2 = \frac{1}{(L'_1 + L'_2) C'_1}$ $\omega_p^2 = \frac{1}{L'_1 C'_1}$	 $A = \frac{C'_1 C'_2}{C'_1 + C'_2}$ $\omega_0^2 = \frac{1}{L'_1 (C'_1 + C'_2)}$ $\omega_p^2 = \frac{1}{L'_1 C'_1}$
Drude: $\mu_{\text{eff}}, \epsilon_{\text{eff}} = A \frac{\omega^2 - \omega_p^2}{\omega^2}$	 $A = L'_0$ $\omega_0^2 = 0$ $\omega_p^2 = \frac{1}{L'_0 C'_1}$	 $A = C'_0$ $\omega_0^2 = 0$ $\omega_p^2 = \frac{1}{L'_1 C'_0}$

can be seen that the Lorentz dispersion yields two solutions for each, the series and shunt branch, while the solution for the Drude dispersion is unambiguous.

With the effective material parameters, the wavenumber (2.8) can be determined. The sign of the square root determines, whether the phase is propagating in forward or backward direction with parallel or anti-parallel² wave vector \mathbf{k} and Poynting vector \mathbf{S} , respectively, so that

$$\frac{k}{|k|} \cdot \frac{\mathbf{S}}{|\mathbf{S}|} = \pm 1. \quad (2.29)$$

A positive product $\mu'_{\text{eff}} \epsilon'_{\text{eff}}$ yields forward propagation whereas for backward propagation, i.e. for a negative product, (2.29) becomes negative [8]. Hence, with the wavenumber (2.8), the phase velocity

$$v_p = \frac{\omega}{\text{Re}\{k(\omega)\}} \quad (2.30)$$

can take positive and negative values. However, for small losses

²In a two- or three-dimensional anisotropic material, the angle between the Poynting vector and wave vector can have arbitrary values [7].

$$\frac{\mu''_{\text{eff}}}{\mu'_{\text{eff}}}, \frac{\varepsilon''_{\text{eff}}}{\varepsilon'_{\text{eff}}} \ll 1 \quad (2.31)$$

the group velocity

$$v_g = \frac{\partial \omega}{\partial \text{Re}\{k\}} \quad (2.32)$$

corresponds to the energy velocity v_e which always has to be positive.

The transmission line model and (2.14) and (2.15) indicate that the effective material parameters can be set independently of each other. Hence, arbitrary configurations of the series and shunt branch are possible to create a required dispersion characteristic. In Sect. 2.4 it will be shown that this separation of the magnetic and electric response is only possible for an infinitesimal short transmission line section.

2.3 Causality and Its Consequences on Dispersion

In the previous section, the quantum-mechanical Lorentz model, and hence, a physically realizable model, was used to find the transmission line model of materials and metamaterials with dispersive characteristics. In this section, realizability of a transmission line model is investigated directly by taking the concept of stability and causality into account.

The effective material parameters of an arbitrary medium can be described by its magnetic and electric susceptibility $\chi_m(\omega)$ and $\chi_e(\omega)$ so that

$$\mu_{\text{eff}}(\omega) = \mu'_{\text{eff}} - j\mu''_{\text{eff}} = -j \frac{Z'_{\text{se}}(\omega)}{\omega} = a_m \mu_0 [\chi_m(\omega) + 1], \quad (2.33)$$

$$\varepsilon_{\text{eff}}(\omega) = \varepsilon'_{\text{eff}} - j\varepsilon''_{\text{eff}} = -j \frac{Y'_{\text{sh}}(\omega)}{\omega} = a_e \varepsilon_0 [\chi_e(\omega) + 1], \quad (2.34)$$

where a_m and a_e account the field distribution of the propagating wave different from a plane wave, e.g. if the host medium is a microstrip transmission line or a hollow wave guide. For plane wave propagation in vacuum $a_m = a_e = 1$. The susceptibility describes the polarization and magnetization of a material, i.e. in time domain the response to an external electric or magnetic field [9]

$$\mathbf{M}(t) = \chi_m(t) * \mathbf{H}(t) = [\chi'_m(t) - j\chi''_m(t)] * \mathbf{H}(t), \quad (2.35)$$

$$\mathbf{P}(t) = \varepsilon_0 \chi_e(t) * \mathbf{E}(t) = [\chi'_e(t) - j\chi''_e(t)] * \mathbf{E}(t). \quad (2.36)$$

Since investigation of causality and dispersion is equivalent for the magnetic and electric susceptibility, the general susceptibility $\chi(t)$ with its Fourier transform

$$\chi(\omega) = \mathcal{F}\{\chi(t)\} = \frac{1}{2\pi} \int_{-\infty}^{\infty} \chi(t) e^{-j\omega t} dt \quad (2.37)$$

is used for both quantities.

Without an external field, the considered material does not exhibit a polarization or magnetization. Hence, the time response $\chi(t)$ has to vanish for negative times which is a general condition for a causal system [10]. According to Titchmarsh's theorem [11, 12], if the square integrability

$$\int_{-\infty}^{\infty} |\chi(\omega)|^2 d\omega \leq C < \infty \quad (2.38)$$

is fulfilled, i.e. the total energy within the system is bounded and cannot be infinitely large [10], the following statements are equivalent, and if one of the conditions is met, all others are automatically fulfilled:

- (i) the time response of the susceptibility vanishes for negative times:

$$\chi(t) = 0 \quad \forall \quad t < 0, \quad (2.39)$$

- (ii) the real and imaginary part of the frequency response are connected by the Hilbert transform

$$\chi(\omega) = -j\mathcal{H}\{\chi(\omega)\} = -\frac{j}{\pi} \oint_{-\infty}^{\infty} \frac{\chi(\Omega)}{\omega - \Omega} d\Omega, \quad (2.40)$$

- (iii) the frequency response $\chi(\omega)$ is analytic in the lower half of the complex ω plane.

All three conditions distinguish a causal time response $\chi(t)$ under the condition of bounded energy (2.38). If $\chi(t)$ is a purely real time response (which is the case for a physical realizable time response), it can be split up into a real even and real odd part which yields together with (i) and the symmetry of the Fourier transform [9, 13]

$$\chi(-\omega) = \chi^*(\omega). \quad (2.41)$$

Thus, for a causal response, the real part $\chi'(\omega)$ has to be an even function while the imaginary part $-\chi''(\omega)$ has to be an odd function over frequency. With that, the integration in (2.38) is symmetric and

$$\int_{-\infty}^{\infty} |\chi(\omega)|^2 d\omega = 2 \int_0^{\infty} |\chi(\omega)|^2 d\omega \leq C < \infty. \quad (2.42)$$

To fulfill the bounded energy criterion (2.42) the susceptibility has to vanish in the high frequency limit so that

$$\lim_{\omega \rightarrow \infty} \chi(\omega) = 0. \quad (2.43)$$

Hence, with (2.33) and (2.34) the effective material parameters have to follow

$$\mu_\infty = \lim_{\omega \rightarrow \infty} \mu_{\text{eff}} = \lim_{\omega \rightarrow \infty} \frac{Z'_{\text{se}}(\omega)}{j\omega} = a_m \mu_0 := L'_0, \quad (2.44)$$

$$\varepsilon_\infty = \lim_{\omega \rightarrow \infty} \varepsilon_{\text{eff}} = \lim_{\omega \rightarrow \infty} \frac{Y'_{\text{sh}}(\omega)}{j\omega} = a_e \varepsilon_0 := C'_0, \quad (2.45)$$

so that at high frequencies the wave propagation is determined only by the host medium with

$$L'_0 = a_m \mu_0 > 0, \quad (2.46)$$

$$C'_0 = a_e \varepsilon_0 > 0. \quad (2.47)$$

Consequently it is not possible to realize arbitrary unit cell configurations. Instead, the unit cell has to consist of at least a series inductance and shunt admittance which do not vanish in the high frequency limit.

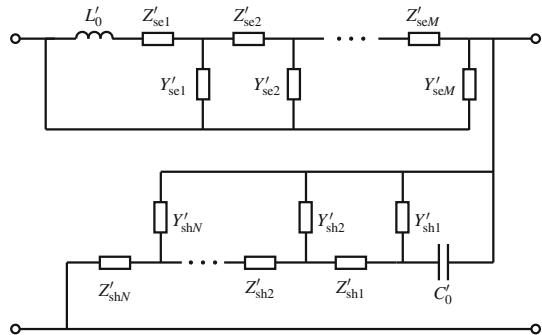
Based on that, the series and shunt branch of a general unit cell can be described as shown in Fig. 2.6 by the distributed complex impedance and admittance

$$Z'_{\text{se}}(\omega) = \frac{1}{Y'_{\text{se}M} + \frac{1}{Z'_{\text{se}M} + \dots \frac{1}{Y'_{\text{se}2} + \frac{1}{Z'_{\text{se}2} + Y'_{\text{se}1} + \frac{1}{Z'_{\text{se}1} + j\omega L'_0}}}}, \quad (2.48)$$

$$Y'_{\text{sh}}(\omega) = \frac{1}{Z'_{\text{sh}N} + \frac{1}{Y'_{\text{sh}N} + \dots \frac{1}{Z'_{\text{sh}2} + \frac{1}{Y'_{\text{sh}2} + Z'_{\text{sh}1} + \frac{1}{Y'_{\text{sh}1} + j\omega C'_0}}}}, \quad (2.49)$$

with the non-zero elements L'_0 and C'_0 . Furthermore, in the high frequency limit, the impact of all elements except L'_0 and C'_0 has to vanish, i.e.

Fig. 2.6 Series and shunt branch impedance and admittance including the minimal required elements L'_0 and C'_0 in the series and shunt branch



$$\lim_{\omega \rightarrow \infty} \frac{Z'_n(\omega)}{j\omega} = \lim_{\omega \rightarrow \infty} \frac{Y'_n(\omega)}{j\omega} = 0. \quad (2.50)$$

Z'_n and Y'_n are not restricted to purely reactive elements but can also contain resistive elements as long as the high frequency condition (2.44) and (2.45) is fulfilled.

Although other topologies for Z'_{se} and Y'_{sh} are possible, the high frequency condition (2.44) and (2.45), which ensures the square integrability (2.42), has to hold for any topology.

2.3.1 Application to Different Unit Cell Configurations

Different unit cell configurations exist to realize a desired dispersion characteristic. If investigated over frequency, not all of them follow (2.44) and (2.45). Thus, not all unit cell configurations fulfill the bounded energy criterion (2.38) and are physically realizable. By using condition (2.43) it is possible to find the physical equivalent circuit of arbitrary unit cell topologies or to test a given unit cell configuration for its realizability and to investigate its high frequency response.

As an example, below, different common unit cell configurations are investigated in terms of causality and their physical realizability.

Microstrip Transmission Line

A microstrip transmission line on a Rogers Duroid 5880 substrate with a copper metallization with a thickness of $17 \mu\text{m}$ and the dimensions as shown in Fig. 2.7a yields a characteristic impedance $Z_c = (50.16 - j84.66 \times 10^{-9}) \Omega$ and a phase constant $\gamma = (0.1456 + j290.8) \text{ m}^{-1}$ at a frequency of 10 GHz.

With (2.12) and (2.13) the distributed unit cell elements become

$$Z'_{se} = \gamma \cdot Z_c = 7.304 \Omega/\text{m} + j\omega 0.184 \mu_0, \quad (2.51)$$

$$Y'_{sh} = \gamma/Z_c = 2.903 \times 10^{-3} \text{ S/m} + j\omega 10.42 \varepsilon_0. \quad (2.52)$$

This corresponds to the transmission line equivalent circuit in Fig. 2.7b with a constant per unit length resistance and inductance in the series branch and a constant

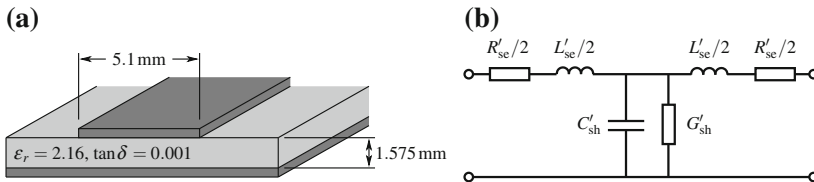


Fig. 2.7 Investigated microstrip transmission line: **a** Cross-section view, **b** transmission line equivalent circuit

per unit length conductance and capacitance in the shunt branch as expected from transmission line theory. Hence, (2.44) and (2.45) yield the high frequency limit

$$\mu_\infty = \lim_{\omega \rightarrow \infty} \left(\frac{R'_{se}}{j\omega} + L'_{se} \right) = L'_0 = a_m \mu_0 = 0.184 \mu_0, \quad (2.53)$$

$$\varepsilon_\infty = \lim_{\omega \rightarrow \infty} \left(\frac{G'_{sh}}{j\omega} + C'_{sh} \right) = C'_0 = a_e \varepsilon_0 = 10.42 \varepsilon_0, \quad (2.54)$$

i.e. the bounded energy criterion (2.42) is fulfilled and in the high frequency limit the dispersion is determined by the series inductance and shunt capacitance. Thus, the unit cell is realizable in its current form.

Left-Handed Unit Cell

A left-handed unit cell as depicted in Fig. 2.8 consists of a series capacitance and a shunt inductance [14]. Adding resistive losses yields the series impedance and shunt admittance

$$Z'_{se,LH}(\omega) = R'_{se} + \frac{1}{j\omega C'_{se}}, \quad (2.55)$$

$$Y'_{sh,LH}(\omega) = G'_{se} + \frac{1}{j\omega L'_{sh}}. \quad (2.56)$$

In the high frequency limit, the complex effective material parameters become

$$\mu_\infty = \lim_{\omega \rightarrow \infty} \frac{Z'_{se,LH}(\omega)}{j\omega} = \varepsilon_\infty = \lim_{\omega \rightarrow \infty} \frac{Y'_{sh,LH}(\omega)}{j\omega} = 0 \quad (2.57)$$

as shown for the effective permeability in Fig. 2.9. L'_0 and C'_0 in Eqs. (2.48) and (2.49) are zero and hence, the magnetic and electric susceptibility do not vanish for large frequencies. Thus, the square integrability (2.42) and the conditions (i)–(iii) are not fulfilled.

Fig. 2.8 Unit cell configuration of a lossy left-handed transmission line

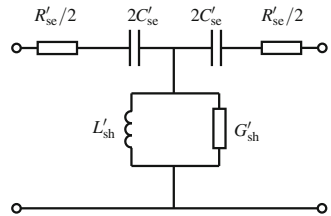


Fig. 2.9 Comparison of the effective permeability of a distributed purely LH and CRLH transmission line ($R'_{se} = 10 \text{ k}\Omega/\text{m}$, $L'_0 = 1 \text{ }\mu\text{H}/\text{m}$, $C'_{se} = 1 \text{ fF} \cdot \text{m}$)

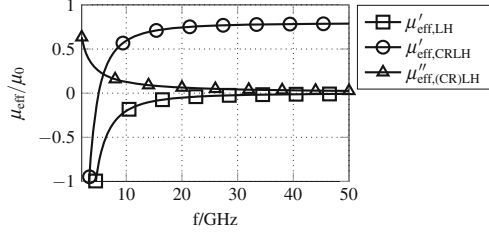
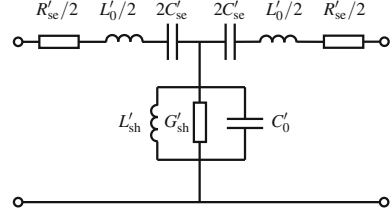


Fig. 2.10 Unit cell configuration of a lossy composite left-handed transmission line



Adding a non-zero L'_0 and C'_0 as in (2.48) and (2.49) yields the composite right/left-handed (CRLH) unit cell [15] as depicted in Fig. 2.10 with the Drude dispersion (2.23) and (2.24) created by

$$Z'_{se,CRLH} = R'_{se} + j \left(\omega L'_0 - \frac{1}{\omega C'_{se}} \right), \quad (2.58)$$

$$Y'_{sh,CRLH} = G'_{sh} + j \left(\omega C'_0 - \frac{1}{\omega L'_{sh}} \right). \quad (2.59)$$

The unit cell consists of a series resonator in the series branch and a parallel resonator in the shunt branch with the magnetic and electric plasma frequency

$$\omega_{p\mu} = \frac{1}{\sqrt{L'_0 C'_{se}}}, \quad \omega_{p\varepsilon} = \frac{1}{\sqrt{L'_{sh} C'_0}}. \quad (2.60)$$

Thus, a non-zero value of L'_0 and C'_0 ensures a finite magnetic and electric plasma frequency, respectively. For the high frequency limit that yields

$$\mu_{\infty} = \lim_{\omega \rightarrow \infty} \left(\frac{R'_{se}}{j\omega} + L'_0 - \frac{1}{\omega^2 C'_{se}} \right) = L'_0 \quad (2.61)$$

and

$$\varepsilon_{\infty} = \lim_{\omega \rightarrow \infty} \left(\frac{G'_{sh}}{j\omega} + C'_0 - \frac{1}{\omega^2 L'_{sh}} \right) = C'_0 \quad (2.62)$$

which can be seen for the effective permeability in Fig. 2.9. The effective permeability in the high frequency limit does not vanish but reaches a constant value. The same holds for the frequency response of the effective permittivity.

A more practical explanation takes the physical implementation and realizability of a unit cell into consideration. The elements C'_{se} and L'_{sh} have to be embedded in a host medium, e.g. a microstrip line, which can be described by a per unit length series inductance and shunt capacitance. Hence, the series inductance L'_0 and shunt capacitance C'_0 can be considered as parasitic effects created by the host medium.

Dual Composite Right/Left-Handed Unit Cell

The series impedance and shunt admittance of a dual composite right/left-Handed (D-CRLH) unit cell in Fig. 2.11, consisting of a parallel resonator in the series branch and a series resonator in the shunt branch [16], are

$$Z'_{se,DCRLH}(\omega) = \frac{1}{G'_{se} + j \left(\omega C'_{se} - \frac{1}{\omega L'_{se}} \right)}, \quad (2.63)$$

$$Y'_{sh,DCRLH}(\omega) = \frac{1}{R'_{sh} + j \left(\omega L'_{sh} - \frac{1}{\omega C'_{sh}} \right)}. \quad (2.64)$$

The high frequency limit becomes

$$\mu_{\infty} = \lim_{\omega \rightarrow \infty} \frac{Z'_{se,DCRLH}(\omega)}{j\omega} = \varepsilon_{\infty} = \lim_{\omega \rightarrow \infty} \frac{Y'_{sh,DCRLH}(\omega)}{j\omega} = 0 \quad (2.65)$$

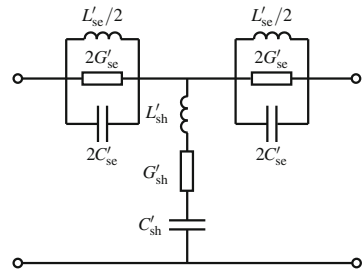
and the condition of square integrability (2.42) is not fulfilled.

The effective material parameters

$$\mu_{eff} = -\frac{1}{C'_{se}} \cdot \frac{1}{\omega^2 - \omega_{0\mu} - j\omega\delta_{\mu}}, \quad (2.66)$$

$$\varepsilon_{eff} = -\frac{1}{L'_{sh}} \cdot \frac{1}{\omega^2 - \omega_{0\varepsilon} - j\omega\delta_{\varepsilon}} \quad (2.67)$$

Fig. 2.11 Unit cell configuration of a lossy dual composite left-handed transmission line



reveal a Lorentz dispersion with the magnetic and electric resonance frequency

$$\omega_{0\mu} = \frac{1}{\sqrt{L'_{se}C'_{se}}}, \quad \omega_{0\varepsilon} = \frac{1}{\sqrt{L'_{sh}C'_{sh}}} \quad (2.68)$$

and the magnetic and electric damping factors

$$\delta_\mu = \frac{G'_{se}}{C'_{se}}, \quad \delta_\varepsilon = \frac{R'_{sh}}{L'_{sh}}. \quad (2.69)$$

However, a transition frequency, i.e. a zero in the dispersion equations where the sign of the real part changes from negative to positive, does not exist. Hence, above the resonance frequency, the real part of the effective material parameters is negative for all frequencies $\omega > \omega_0$.

Addition of the series inductance L'_0 in the series branch and the parallel capacitance C'_0 in the shunt branch yields the effective material parameters

$$\mu_{\text{eff}} = L'_0 \left(1 - \frac{\omega_{t\mu}^2 - \omega_{0\mu}^2}{\omega^2 - \omega_{0\mu}^2 - j\omega\delta_\mu} \right), \quad (2.70)$$

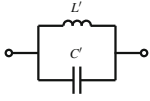
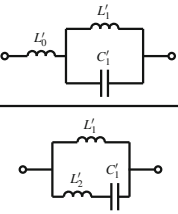
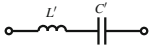
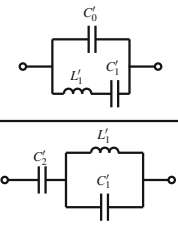
$$\varepsilon_{\text{eff}} = C'_0 \left(1 - \frac{\omega_{t\varepsilon}^2 - \omega_{0\varepsilon}^2}{\omega^2 - \omega_{0\varepsilon}^2 - j\omega\delta_\varepsilon} \right) \quad (2.71)$$

following the Lorentz dispersion (2.17) and (2.18). As for the CRLH unit cell, $L'_0 = \mu_\infty$ and $C'_0 = \varepsilon_\infty$ ensure the square integrability (2.42) as well as a finite magnetic and electric transition frequency

$$\omega_{t\mu} = \sqrt{\omega_{0\mu}^2 + \frac{1}{L'_0 C'_{se}}}, \quad \omega_{t\varepsilon} = \sqrt{\omega_{0\varepsilon}^2 + \frac{1}{C'_0 L'_{sh}}}. \quad (2.72)$$

The general configuration in Fig. 2.6 indicates that for the D-CRLH unit cell, the addition of the inductance in the series branch and capacitance in the shunt branch can be done at different positions of the unit cell to enforce the square integrability. As shown in Table 2.2, an inductance L'_0 and capacity C'_0 can be added in series and parallel of the original series and shunt branch, respectively, which has been done in the previous investigation. Another possibility is the addition of L'_2 and C'_2 , which also yields a correct Lorentz dispersion with a finite transition frequency and a positive high frequency limit (2.44) and (2.45). The corrected unit cell configurations correspond to the Lorentz- and Drude dispersion models derived before in Sect. 2.2. The number of possible positions is increased with the number of elements (M , N in (2.48) and (2.49)) in the unit cell. The resulting series impedance and shunt admittance are closely related to reactances and its negative reciprocals, respectively, in the form a Foster network [17]. The difference is that in the present topology, losses can be taken into account by the use of complex poles and zeros in the impedance and admittance function.

Table 2.2 D-CRLH unit cell elements with corrected series- and shunt impedance and admittance

	Original	Corrected
Series branch impedance Z'_{se}		
Shunt branch admittance Y'_{sh}		

2.3.2 Kramers–Kronig Relation for Phase Reconstruction

The Hilbert transform (2.40), also known as Kramers–Kronig relation [11, 12], relates the real and imaginary part of complex transfer functions of causal and stable systems. Here, these transfer functions are the magnetizability χ_m and polarizability χ_e of a continuous material or periodic structure.

The complex wavenumber k can be expressed by the material parameters so that

$$k^2(\omega) = k_0^2(\omega) [1 + \chi_m(\omega)] [1 + \chi_e(\omega)], \quad (2.73)$$

where k_0 is the free space wavenumber

$$k_0(\omega) = \omega \sqrt{\mu_0 \epsilon_0}. \quad (2.74)$$

For a causal and stable material, Titchmarsh's theorem and hence, the Kramers–Kronig relation (2.40) has to be fulfilled for $\chi_m(\omega)$ and $\chi_e(\omega)$. Since the symmetry (2.41) of the real and imaginary parts after the multiplication of both susceptibilities is maintained, the square of the wavenumber in the form

$$\frac{k^2(\omega)}{k_0^2(\omega)} - 1 = \chi_m(\omega) + \chi_e(\omega) + \chi_m(\omega)\chi_e(\omega) \quad (2.75)$$

is a causal spectrum so that the Kramers–Kronig relation can be applied and

$$\frac{k^2(\omega)}{k_0^2(\omega)} = 1 - \frac{j}{\pi} \oint_{-\infty}^{\infty} \frac{k^2(\Omega)/k_0^2(\Omega)}{\omega - \Omega} d\Omega. \quad (2.76)$$

The integral denotes the Cauchy principal value

$$\oint_a^b f(x)dx = \lim_{\epsilon \rightarrow 0+} \left(\int_a^{c-\epsilon} f(x)dx + \int_{c+\epsilon}^b f(x)dx \right). \quad (2.77)$$

A detailed derivation taking into account the symmetry (2.41) can be found in Appendix A.1.

The Kramers–Kronig relation can be applied to the square of the wavenumber $k^2(\omega)$ or to the square of the refractive index [18]

$$n^2(\omega) = \frac{k^2(\omega)}{k_0^2(\omega)} \quad (2.78)$$

while an application directly to the wavenumber as in extraction methods [19, 20] is in general not possible since the causality of $k(\omega)$ is not necessarily maintained by the square root [18]. For small susceptibilities, however, it can be approximated

$$k(\omega) \approx k_0(\omega) \left(1 + \frac{\chi_m(\omega)}{2} \right) \left(1 + \frac{\chi_e(\omega)}{2} \right) \quad (2.79)$$

which has, concerning the susceptibilities, the form of (2.73) so that the Kramers–Kronig relation can be approximated and

$$\frac{k(\omega)}{k_0(\omega)} \approx 1 - \frac{j}{\pi} \oint_{-\infty}^{\infty} \frac{k(\Omega)/k_0(\Omega)}{\omega - \Omega} d\Omega. \quad (2.80)$$

For the real part of the wavenumber this yields

$$\frac{\text{Re}\{k(\omega)\}}{k_0(\omega)} \approx 1 + \frac{1}{\pi} \oint_{-\infty}^{\infty} \frac{\text{Im}\{k(\Omega)\}/k_0(\Omega)}{\omega - \Omega} d\Omega. \quad (2.81)$$

With that, the wavenumber, which in many extraction methods is ambiguous, can be determined from the losses, expressed by the non-ambiguous imaginary part $\text{Im}\{k\}$. Due to the symmetry (2.41), integration only of the positive part of the spectrum is necessary

$$\frac{\text{Re}\{k(\omega)\}}{k_0(\omega)} \approx 1 + \frac{2}{\pi} \int_0^{\infty} \frac{\omega \text{Im}\{k(\Omega)\}/k_0(\Omega)}{\omega^2 - \Omega^2} d\Omega \quad (2.82)$$

which is used in phase reconstruction methods [19, 20] and later in extraction of effective material parameters in Sect. 4.1.

2.4 Effective Material Parameters of Discrete Periodic Structures

In passive, continuous media, Maxwell's equations (2.1)–(2.4) and the material relations (2.5) and (2.6) are defined for the same point \mathbf{r} in space. $\mathbf{D}(t, \mathbf{r})$ is determined by $\mathbf{E}(t', \mathbf{r})$ and $\mathbf{B}(t, \mathbf{r})$ by $\mathbf{H}(t', \mathbf{r})$ in the same point with a temporal dispersion caused by the material. However, in a discretized, effective material, this is not fulfilled anymore since the response in the point \mathbf{r} is determined by the field in the point \mathbf{r}' . The physical distance $|\mathbf{r} - \mathbf{r}'|$ between these two points causes a phase difference between $\mathbf{D}(t, \mathbf{r})$ and $\mathbf{E}(t', \mathbf{r}')$, and between $\mathbf{B}(t, \mathbf{r})$ and $\mathbf{H}(t', \mathbf{r}')$, respectively. Since this dispersion is caused by the spatial separation of the magnetic response and the electric response, it is called spatial dispersion [9].

The effect of spatial dispersion can be considered in the transmission line model. Up to this point it was assumed that the impedance and admittance to design a desired dispersion are distributed elements in an infinitesimal short unit cell, i.e. impedance and admittance can be defined over an infinitesimal short section. In a real implementation, such distributed elements cannot be realized since they cannot be arbitrarily scaled down in size but will always have a finite physical extent. Hence, lumped elements have to be used to approximate the distributed values

$$Z'_{\text{se}}(\omega) = \lim_{\Delta z \rightarrow 0} \frac{Z_{\text{se}}(\omega)}{\Delta z} \approx \frac{1}{\Delta z} Z_{\text{se}}(\omega), \quad (2.83)$$

$$Y'_{\text{sh}}(\omega) = \lim_{\Delta z \rightarrow 0} \frac{Y_{\text{sh}}(\omega)}{\Delta z} \approx \frac{1}{\Delta z} Y_{\text{sh}}(\omega). \quad (2.84)$$

Material parameters derived from field values at the interface of such discretized structures are non-local. Another explanation is based on the phase response of the unit cell. With increasing frequency, a periodic structure with distributed elements can provide an infinitely large phase shift since it consists of an infinite number of unit cells. If these distributed elements are replaced by lumped elements, the unit cell number in a certain physical length becomes finite and hence, the maximum phase shift is limited. Here, the impact of this discretization on effective material parameters, which has to be taken into account under certain conditions, is investigated.

The Bloch impedance, i.e. the characteristic impedance of periodic structures,

$$Z_B = \pm \sqrt{\frac{\mu_{\text{eff}}}{\varepsilon_{\text{eff}}}} \quad (2.85)$$

and the wavenumber

$$k = \pm \omega \sqrt{\mu_{\text{eff}} \varepsilon_{\text{eff}}} \quad (2.86)$$

can be used to describe the wave propagation in periodic, discrete structures equivalent to the propagation in homogenous materials [21]. Since for the discrete case

these parameters not only depend on the element values, but also on the unit cell configuration, different topologies are investigated.

Unit Cell in T-Configuration

Figure 2.12 shows an unsymmetric unit cell in T-configuration. The unit cell length p is finite and non-zero and using the chain parameters, the port voltages and currents of the n -th unit cell in an infinite array become

$$V[np] = V[(n+1)p](1 + Z_1 Y_2) + I[(n+1)p](Z_1 + Z_2 + Z_1 Y_2 Z_3), \quad (2.87)$$

$$I[np] = V[(n+1)p]Y_2 + I[(n+1)p](1 + Y_2 Z_3). \quad (2.88)$$

Due to the periodicity, the Floquet–Bloch theorem [21] with the periodic boundary condition

$$V[(n+1)p] = V[np]e^{-jk^{(T)}p}, \quad (2.89)$$

$$I[(n+1)p] = I[np]e^{-jk^{(T)}p} \quad (2.90)$$

yields

$$V[np] = V[np](1 + Z_1 Y_2)e^{-jk^{(T)}p} + I[np](Z_1 + Z_2 + Z_1 Y_2 Z_3)e^{-jk^{(T)}p}, \quad (2.91)$$

$$I[np] = V[np]Y_2 e^{-jk^{(T)}p} + I[np](1 + Y_2 Z_3)e^{-jk^{(T)}p}. \quad (2.92)$$

The Bloch impedance of a periodic structure is defined as the ratio of the voltage and current at each unit cell interface and has to be independent of the position n of the infinite array:

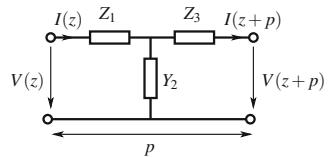
$$Z_B[np] = \frac{V[np]}{I[np]} \stackrel{!}{=} Z_B[(n+1)p] = \frac{V[(n+1)p]}{I[(n+1)p]}. \quad (2.93)$$

That yields the two conditions

$$Z_B^{(T)} = \frac{Z_1 + Z_3 + Z_1 Y_2 Z_3}{e^{jk^{(T)}p} - (1 + Z_1 Y_2)} \quad (2.94)$$

and

Fig. 2.12 Unsymmetric unit cell in T-configuration



$$Z_B^{(T)} = \frac{e^{jk^{(T)}p} - (1 + Y_2 Z_3)}{Y_2} \quad (2.95)$$

and thus,

$$Z_B^{(T)} = \frac{Z_1 - Z_3}{2} \pm \sqrt{\frac{(Z_1 - Z_3)^2}{4} + \frac{Z_1 + Z_3}{Y_2} + Z_1 Z_3}. \quad (2.96)$$

In an array of unsymmetric unit cells with $Z_1 \neq Z_3$, the Bloch impedance experienced by the propagating wave depends on its direction. Hence, the two solutions of the Bloch impedance correspond to the wave propagating in positive or negative direction of the periodic structure.

Furthermore, (2.94) and (2.95) yield the dispersion relation

$$e^{j2k^{(T)}p} - (2 + Z_1 Y_2 + Y_2 Z_3)e^{jk^{(T)}p} + 1 = 0 \quad (2.97)$$

so that

$$k^{(T)} = \pm \frac{1}{p} \left[\cos^{-1} \left(1 + \frac{(Z_1 + Z_3)Y_2}{2} \right) + 2m\pi \right]. \quad (2.98)$$

To obtain the same Bloch parameters for the forward and backward propagating wave, the unit cell has to be symmetric with $Z_1 = Z_3 = Z_{se}/2$ and $Y_2 = Y_{sh}$ so that (2.96) and (2.98) become

$$Z_{Bsym}^{(T)} = \pm \sqrt{\frac{4Z_{se} + Z_{se}^2 Y_{sh}}{4Y_{sh}}}, \quad (2.99)$$

$$k^{(T)} = \pm \frac{1}{p} \left[\cos^{-1} \left(1 + \frac{Z_{se} Y_{sh}}{2} \right) + 2m\pi \right]. \quad (2.100)$$

Using (2.85) and (2.86), the effective material parameters of the symmetric T-unit cell become

$$\mu_{eff}^{(T)}(\omega) = \pm \frac{1}{\omega p} \cos^{-1} \left(1 - \frac{(\omega p)^2}{2} \tilde{\mu} \tilde{\varepsilon} \right) \sqrt{\frac{\tilde{\mu}}{\tilde{\varepsilon}} - \left(\frac{\omega p \tilde{\mu}}{2} \right)^2} \quad (2.101)$$

$$\varepsilon_{eff}^{(T)}(\omega) = \pm \frac{1}{\omega p} \cos^{-1} \left(1 - \frac{(\omega p)^2}{2} \tilde{\mu} \tilde{\varepsilon} \right) \sqrt{\frac{\tilde{\mu}}{\tilde{\varepsilon}} - \left(\frac{\omega p \tilde{\mu}}{2} \right)^2}^{-1} \quad (2.102)$$

where $\tilde{\mu}$ and $\tilde{\varepsilon}$ denote the effective material parameters (2.14) and (2.15) of the distributed structure with $p \rightarrow 0$. It can be seen that for a finite unit cell length with $p > 0$, the effective material parameters are not only determined by the unit cell element values, but also by the unit cell length p and the wavenumber of the distributed structure

$$\tilde{k}(\omega) = \omega \sqrt{\tilde{\mu}(\omega) \tilde{\varepsilon}(\omega)}. \quad (2.103)$$

Furthermore, the effective material parameters are not independent of each other since both, the effective permeability and permittivity, are a function of both distributed material parameters and hence, of the series and shunt branch of the unit cell.

For a small unit cell length with $\omega p \ll \frac{1}{\sqrt{\tilde{\mu}(\omega)\tilde{\varepsilon}(\omega)}}$, the inverse cosine becomes

$$\lim_{\omega p \rightarrow 0} \frac{1}{\omega p} \cos^{-1} \left(1 - \frac{(\omega p)^2}{2} a \right) = \pm \sqrt{a} \quad (2.104)$$

so that for a small unit cell length compared to guided wavelength, the material parameters of the discrete periodic structure can be approximated by the effective material parameters of the distributed structure:

$$\lim_{\omega p \rightarrow 0} \mu_{\text{eff}}^{(\text{T})} = \tilde{\mu}, \quad (2.105)$$

$$\lim_{\omega p \rightarrow 0} \varepsilon_{\text{eff}}^{(\text{T})} = \tilde{\varepsilon}. \quad (2.106)$$

For large values of $|\tilde{\mu}(\omega) \cdot \tilde{\varepsilon}(\omega)|$, e.g. close to a Lorentz resonance or for low frequencies in a Drude material, this approximation is not valid and the deviation between the effective material parameters of the discrete and distributed structure becomes significant [22, 23].

Unit Cell in Π -Configuration

Equivalent to the T-configuration, the voltages and currents at the ports of an unsymmetric unit cell in Π -configuration as shown in Fig. 2.13 are

$$V[np] = V[(n+1)p](1 + Z_2 Y_3) + I[(n+1)p]Z_2, \quad (2.107)$$

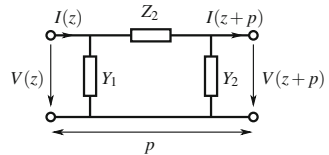
$$I[np] = V[(n+1)p](Y_1 + Y_1 Z_2 Y_3 + Y_3) + I[(n+1)p](1 + Y_1 Z_2). \quad (2.108)$$

The periodic boundary condition gives

$$V[np] = V[np](1 + Z_2 Y_3)e^{-jk^{(\text{T})}p} + I[np]Z_2 e^{-jk^{(\text{T})}p} \quad (2.109)$$

$$I[np] = V[np](Y_1 + Y_1 Z_2 Y_3 + Y_3)e^{-jk^{(\text{T})}p} + I[np](1 + Y_1 Z_2)e^{-jk^{(\text{T})}p} \quad (2.110)$$

Fig. 2.13 Unit cell in Π -configuration



and with (2.93)

$$Z_B^{(\Pi)} = \frac{Z_2}{e^{jk^{(\Pi)}p} - (1 + Z_2 Y_3)} \quad (2.111)$$

and

$$Z_B^{(\Pi)} = \frac{e^{jk^{(\Pi)}p} - (1 + Y_1 Z_2)}{Y_1 + Y_1 Z_2 Y_3 + Y_3}. \quad (2.112)$$

This yields the Bloch impedance of the unit cell in Π -configuration

$$Z_B^{(\Pi)} = \frac{Z_2(Y_3 - Y_1)}{2(Y_1 + Y_1 Z_2 Y_3 + Y_3)} \pm \sqrt{\left(\frac{Z_2(Y_3 - Y_1)}{2(Y_1 + Y_1 Z_2 Y_3 + Y_3)}\right)^2 + \frac{Z_2}{Y_1 + Y_1 Z_2 Y_3 + Y_3}}. \quad (2.113)$$

The phase terms give the dispersion relation

$$e^{j2k^{(\Pi)}p} - (2 + Y_1 Z_2 + Z_2 Y_3)e^{jk^{(\Pi)}p} + 1 = 0 \quad (2.114)$$

and thus

$$k^{(\Pi)} = \pm \frac{1}{p} \left[\cos^{-1} \left(1 + \frac{(Y_1 + Y_3)Z_2}{2} \right) + 2m\pi \right]. \quad (2.115)$$

As before for the T-configuration, a symmetric unit cell results in a Bloch impedance which is independent of the propagation direction so that with $Y_1 = Y_3 = Y_{\text{sh}}/2$ and $Z_2 = Z_{\text{se}}$ the Bloch impedance is

$$Z_{B\text{sym}}^{(\Pi)} = \pm \sqrt{\frac{4Z_{\text{se}}}{4Y_{\text{sh}} + Z_{\text{se}}Y_{\text{sh}}^2}} \quad (2.116)$$

and the wavenumber is

$$k^{(\Pi)} = \pm \frac{1}{p} \left[\cos^{-1} \left(1 + \frac{Z_{\text{se}}Y_{\text{sh}}}{2} \right) + 2m\pi \right] = k^{(\text{T})}. \quad (2.117)$$

With (2.85) and (2.86), the effective material parameters of the symmetric Π -unit cell become

$$\mu_{\text{eff}}^{(\Pi)}(\omega) = \pm \frac{1}{\omega p} \cos^{-1} \left(1 - \frac{(\omega p)^2}{2} \tilde{\mu} \tilde{\varepsilon} \right) \sqrt{\frac{\tilde{\varepsilon}}{\tilde{\mu}} - \left(\frac{\omega p \tilde{\varepsilon}}{2} \right)^2}^{-1} \quad (2.118)$$

$$\varepsilon_{\text{eff}}^{(\Pi)}(\omega) = \pm \frac{1}{\omega p} \cos^{-1} \left(1 - \frac{(\omega p)^2}{2} \tilde{\mu} \tilde{\varepsilon} \right) \sqrt{\frac{\tilde{\varepsilon}}{\tilde{\mu}} - \left(\frac{\omega p \tilde{\varepsilon}}{2} \right)^2} \quad (2.119)$$

which for a small guided wavelength become

$$\lim_{\omega p \rightarrow 0} \mu_{\text{eff}}^{(\Pi)} = \tilde{\mu}, \quad (2.120)$$

$$\lim_{\omega p \rightarrow 0} \varepsilon_{\text{eff}}^{(\Pi)} = \tilde{\varepsilon}. \quad (2.121)$$

Unit Cell in L-Configuration

The strongly unsymmetric unit cell in L-configuration is a special case of the T- and Π -configuration and can be derived from the T-configuration with the impedance Z_3 set to zero or from the Π -configuration with the admittance Y_1 set to zero. With $Z_1 = Z_2 = Z_{\text{se}}$, $Y_2 = Y_{\text{sh}}$ and $Y_1 = Z_3 = 0$ this yields

$$Z_B^{(\text{L})} = \frac{Z_{\text{se}}}{2} \pm \sqrt{\frac{Z_{\text{se}}^2}{4} + \frac{Z_{\text{se}}}{Y_{\text{sh}}}} \quad (2.122)$$

and

$$k^{(\text{L})} = \pm \frac{1}{p} \left[\cos^{-1} \left(1 + \frac{Z_{\text{se}} Y_{\text{sh}}}{2} \right) + 2m\pi \right]. \quad (2.123)$$

The effective material parameters after the discretization become

$$\mu_{\text{eff}}^{(\text{L})}(\omega) = \frac{1}{\omega p} \cos^{-1} \left(1 - \frac{(\omega p)^2}{2} \tilde{\mu} \tilde{\varepsilon} \right) \left(\frac{j\omega p \tilde{\mu}}{2} \pm \sqrt{\frac{\tilde{\mu}}{\tilde{\varepsilon}} - \left(\frac{\omega p \tilde{\mu}}{2} \right)^2} \right), \quad (2.124)$$

$$\varepsilon_{\text{eff}}^{(\text{L})}(\omega) = \frac{1}{\omega p} \cos^{-1} \left(1 - \frac{(\omega p)^2}{2} \tilde{\mu} \tilde{\varepsilon} \right) \left(\frac{j\omega p \tilde{\mu}}{2} \pm \sqrt{\frac{\tilde{\mu}}{\tilde{\varepsilon}} - \left(\frac{\omega p \tilde{\mu}}{2} \right)^2} \right)^{-1}. \quad (2.125)$$

It can be seen that, due to the unsymmetry of the unit cell, not only the Bloch impedance, but also the effective material parameters depend on the propagation direction, i.e. although a wave experiences the same phase shift for the forward and backward direction, the Bloch impedance and hence, the effective material parameters are different.

As for the T- and Π -configuration, the small wavelength approximation of the effective material parameters becomes

$$\lim_{\omega p \rightarrow 0} \mu_{\text{eff}}^{(\text{L})} = \tilde{\mu}, \quad (2.126)$$

$$\lim_{\omega p \rightarrow 0} \varepsilon_{\text{eff}}^{(\text{L})} = \tilde{\varepsilon}. \quad (2.127)$$

Discretization of a Lorentz–Drude Material

The impact of discretization on the dispersion parameters and the resulting spatial dispersion is demonstrated for an effective Lorentz–Drude material and a unit cell in T-, Π - and L-configuration. The Lorentz parameters for the effective permeability are $\omega_{0\mu} = 2\pi \cdot 1.1$ GHz, $\omega_{t\mu} = 2\pi \cdot 1.5$ GHz, $\delta_\mu = 100$ MHz, $\mu_\infty = \mu_0$ and the Drude parameters for the effective permittivity are $\omega_{pe} = 2\pi \cdot 2$ GHz, $\delta_e = 100$ MHz, $\varepsilon_\infty = 2\varepsilon_0$.

In the ideal case for an infinitesimal short unit cell, these parameters yield different propagation and stop bands. Below $\omega_{0\mu}$ the effective permeability and permittivity have different signs which results in a stop band due to the imaginary wavenumber (2.8). The same stop band behavior can be observed between $\omega_{t\mu}$ and ω_{pe} . In the frequency band between $\omega_{0\mu}$ and $\omega_{t\mu}$, both, μ'_{eff} and $\varepsilon'_{\text{eff}}$ simultaneously become negative yielding a backward wave band with a negative phase velocity $v_p < 0$. Above ω_{pe} , μ'_{eff} and $\varepsilon'_{\text{eff}}$ are positive resulting in a forward wave band with $v_p > 0$.

The dispersion parameters for the distributed unit cell with $p \rightarrow 0$ and for a unit cell length of 10 and 40 mm can be seen in Fig. 2.14 for the T-configuration and in Fig. 2.15 for the Π -configuration, respectively. Using the distributed model, the dispersion parameters are independent of the unit cell configuration. The effective permeability follows the Lorentz dispersion (2.17) whereas the permittivity follows the Drude dispersion (2.24). In the region of simultaneously negative μ'_{eff} and $\varepsilon'_{\text{eff}}$, the wavenumber k becomes negative, while for positive μ'_{eff} and $\varepsilon'_{\text{eff}}$, the wavenumber is positive.

The dispersion properties of the T- and Π -configuration differ when the unit cell length becomes larger. This becomes noticeable near the magnetic resonance frequency of 1.1 GHz, where the wavenumber (2.103) is large. Here, an anti-resonance or resonance occurs in the real part of the effective permittivity [23]. Furthermore, it can be seen that the shape of the effective permeability differs from its original form (2.17).

It can be seen in the plot of the unit cell phase shift that it is saturated at $kp = \pm\pi$, which is the maximum possible unit cell phase shift of a discrete Lorentz–Drude unit cell. Although in the distributed case, the phase shift becomes very large near the magnetic resonance frequency, it is bounded by the discretization and the maximum unit cell phase shift. Hence, the usable bandwidth of the backward wave transmission band becomes smaller with an increased unit cell length.

In Fig. 2.16, the real part of the Bloch impedance and the effective material parameters according to the two solutions of (2.122) of the unit cell in L-configuration are shown. For an infinitesimal short unit cell, both solutions, representing the forward and backward propagating wave, are identical. However, if the unit cell length is increased, the effect of spatial dispersion becomes apparent. As in the T- and Π -configuration, the shape of the effective material parameters differ from the ideal Lorentz–Drude dispersion and resonances occur in the effective permittivity. Furthermore, all dispersion parameters except the phase are different for waves in forward and backward direction.

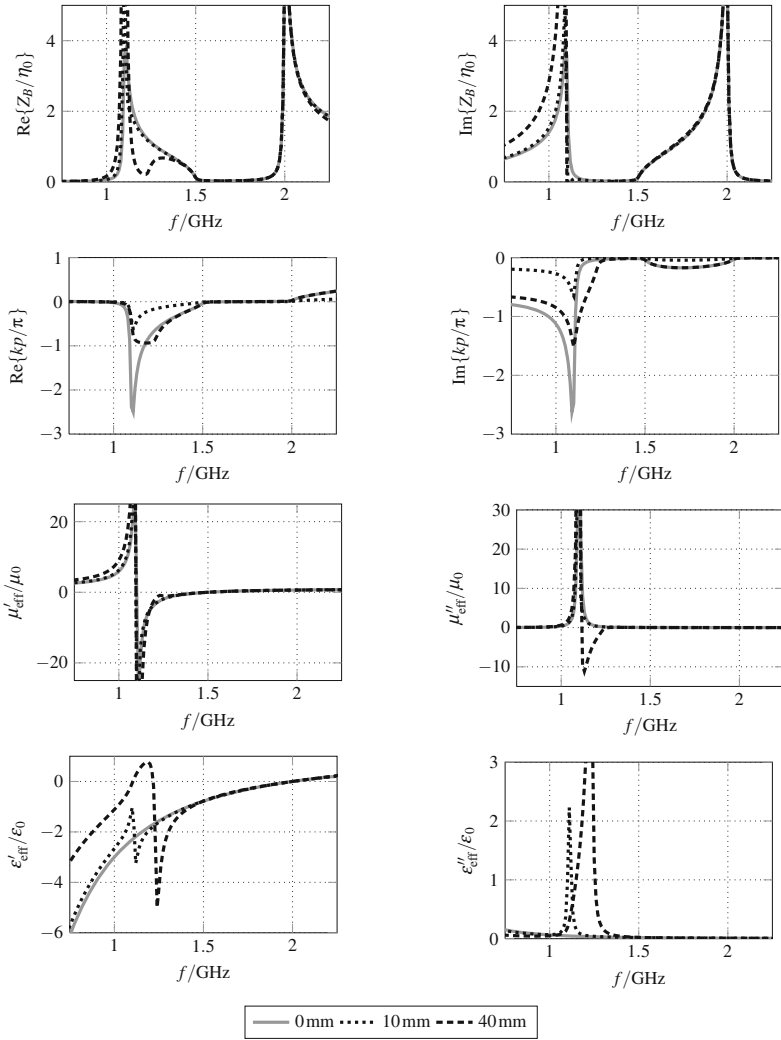


Fig. 2.14 Impact of the unit cell length on the dispersion parameters of a symmetric unit cell in T-configuration

Due to the equivalence between effective material parameters and transmission line parameters (2.85) and (2.86), the impact of discretization depends on the unit cell circuit and not on the geometry of the unit cell. Hence, the presented considerations are valid for one-dimensional artificial transmission lines as well as for two- and three-dimensional lattices.

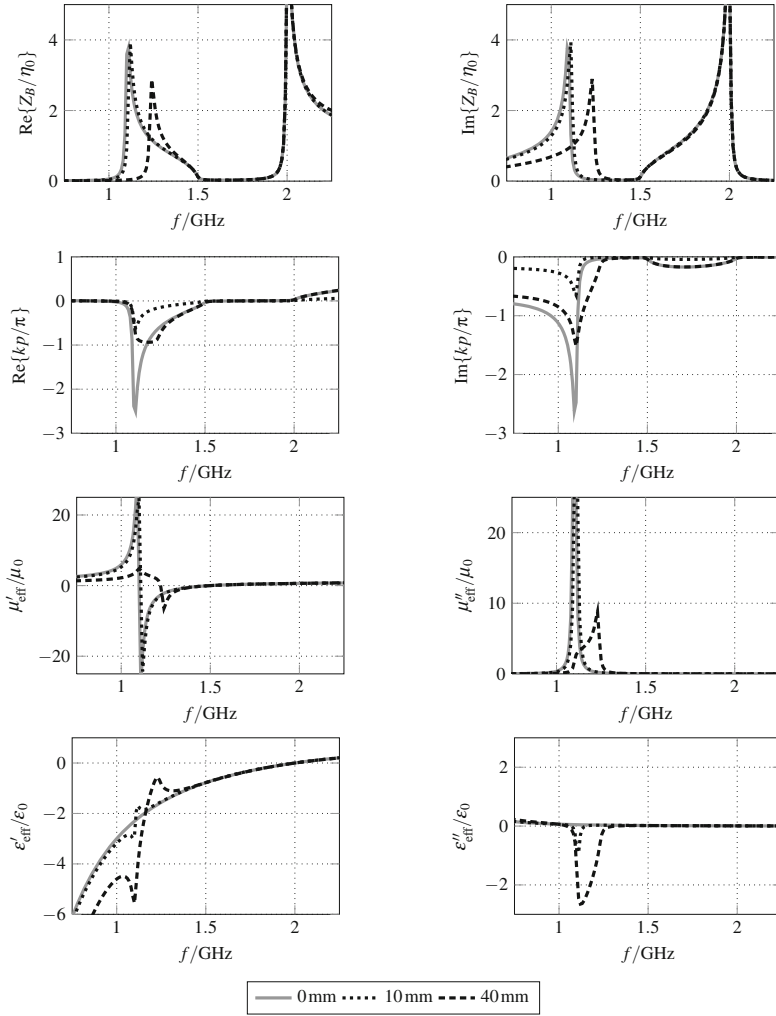


Fig. 2.15 Impact of the unit cell length on the dispersion parameters of a symmetric unit cell in Π -configuration

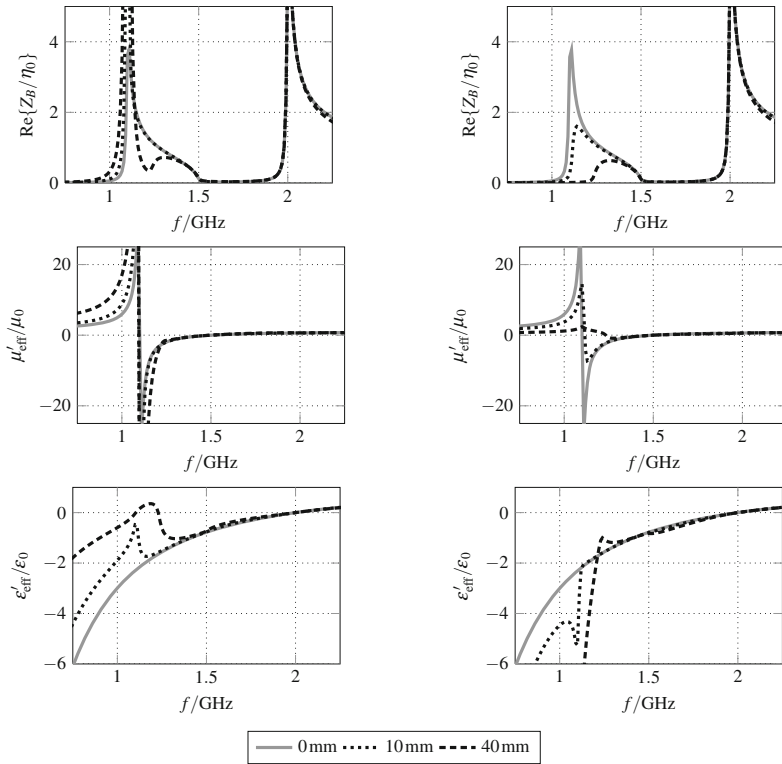


Fig. 2.16 Impact of the unit cell length on the real part of the Bloch impedance and the effective material parameters of a unit cell in unsymmetric L-configuration

References

1. J.D. Jackson, *Classical Electrodynamics*, 3rd edn. (Wiley, New York, 1998)
2. D. Pozar, *Microwave Engineering* (Wiley, New York, 2012)
3. G. Eleftheriades, A. Iyer, P. Kremer, Planar negative refractive index media using periodically L-C loaded transmission lines. *IEEE Trans. Microw. Theory Tech.* **50**, 2702–2712 (2002)
4. K.G. Eleftheriades, G.V. Balmain, *Negative-Refractive Metamaterials—Fundamental Principles and Applications* (Wiley, New York, 2005)
5. A.D. Rakić, A.B. Djurišić, J.M. Elazar, M.L. Majewski, Optical properties of metallic films for vertical-cavity optoelectronic devices. *Appl. Opt.* **37**, 5271–5283 (1998)
6. H.M. Nussenzweig, *Causality and Dispersion Relations* (Academic Press, New York, 1972)
7. T.M. Grzegorzczuk, M. Nikku, X. Chen, B.-I. Wu, J.A. Kong, Refraction laws for anisotropic media and their application to left-handed metamaterials. *IEEE Trans. Microw. Theory Tech.* **53**(4), 1443–1450 (2005)
8. V.G. Veselago, The electrodynamics of substances with simultaneously negative values of ϵ and μ . *Sov. Phys. Uspekhi* **10**(4), 509 (1968)
9. L.D. Landau, E.M. Lifshitz, A.L. King, Electrodynamics of continuous media. *Am. J. Phys.* **29**(9), 647–648 (1961)

10. B. Girod, R. Rabenstein, A. Stenger, Einführung in die Systemtheorie: Signale und Systeme in der Elektrotechnik und Informationstechnik. Lehrbuch Elektrotechnik (Vieweg+Teubner Verlag, 2007)
11. J.S. Toll, Causality and the dispersion relation: logical foundations. Phys. Rev. **104**, 1760–1770 (1956)
12. R.L. Weaver, Y.-H. Pao, Dispersion relations for linear wave propagation in homogeneous and inhomogeneous media. J. Math. Phys. **22**(9), 1909–1918 (1981)
13. R. Bracewell, *The Fourier Transform and Its Applications*, McGraw-Hill Series in Electrical and Computer Engineering (McGraw Hill, New York, 2000)
14. A. Iyer, G. Eleftheriades, Negative refractive index metamaterials supporting 2-d waves, in *2002 IEEE MTT-S International Microwave Symposium Digest*, vol. 2 (2002), pp. 1067–1070
15. A. Lai, T. Itoh, C. Caloz, Composite right/left-handed transmission line metamaterials. IEEE Microw. **5**(3), 34–50 (2004)
16. C. Caloz, Dual composite right/left-handed (D-CRLH) transmission line metamaterial. IEEE Microw. Wirel. Compon. Lett. **16**, 585–587 (2006)
17. R.M. Foster, A reactance theorem. Bell Syst. Tech. J. **3**(2), 259–267 (1924)
18. M.I. Stockman, Criterion for negative refraction with low optical losses from a fundamental principle of causality. Phys. Rev. Lett. **98**, 177404+ (2007)
19. V.V. Varadan, R. Ro, Unique retrieval of complex permittivity and permeability of dispersive materials from reflection and transmitted fields by enforcing causality. IEEE Trans. Microw. Theory Tech. **55**, 2224–2230 (2007)
20. Z. Szabo, G.-H. Park, R. Hedge, E.-P. Li, A unique extraction of metamaterial parameters based on Kramers–Kronig relationship. IEEE Trans. Microw. Theory Tech. **58**(10), 2646–2653 (2010)
21. R. Collin, I. Antennas, P. Society, Field theory of guided waves, in *The IEEE/OUP Series on Electromagnetic Wave Theory (Formerly IEEE Only)*. Series Editor Series (IEEE Press, 1991)
22. C.R. Simovski, S.A. Tretyakov, Local constitutive parameters of metamaterials from an effective-medium perspective. Phys. Rev. B **75**, 195111 (2007)
23. T. Cui, D. Smith, R. Liu, *Metamaterials: Theory, Design, and Applications* (Springer, New York, 2009)

Chapter 3

Implementation of Three-Dimensional Lorentz-Drude-Materials

The previous chapter has demonstrated how the magnetic and electric response of a periodic structure can be designed by adapting the elements of the unit cell. For transmission line metamaterials, where a guided wave propagates within a lattice, this can be done by employing lumped elements according to the desired magnetic and electric response. However, for three-dimensional transmission line metamaterials [1, 2], coupling to the incident wave in free space and technological complexity are limiting factors. An alternative approach is the use of rings, wires and combinations of them to form a lattice that is excited by an incident wave, to independently manipulate the magnetic and electric response, respectively.

In this chapter, different three-dimensional unit cell particles are investigated and their dispersion characteristics and transmission line equivalent circuits are derived. Two fundamental configurations to manipulate the electric and magnetic field with periodic structures, the wire medium [3, 4] and the split-ring resonator [5], are investigated. They are the basis for most unit cell particles, such as omega resonators [6] or the fishnet [7, 8], which are used later in this work. Additionally, dispersion experienced by waves propagating in hollow waveguides is investigated and described in terms of effective material parameters.

3.1 Wire Lattice

Figure 3.1a shows a section of a wire lattice [3, 4]. The cylindrical wires with the diameter d and the periodicity p in the xz -plane are continuous in y -direction. A lumped element representation of a single cubic unit cell with the side length p , where the lossy wire is modeled by the series connection of an inductor and resistor, is shown in Fig. 3.1b for the excitation with a plane wave and the electric field parallel to the wires.

Taking causality and the high frequency limit (2.44) and (2.45) into account, the unit cell equivalent circuit in Fig. 3.2 can be derived where the series inductance L_0 and shunt capacitance C_0 represent the permeability and permittivity of the host

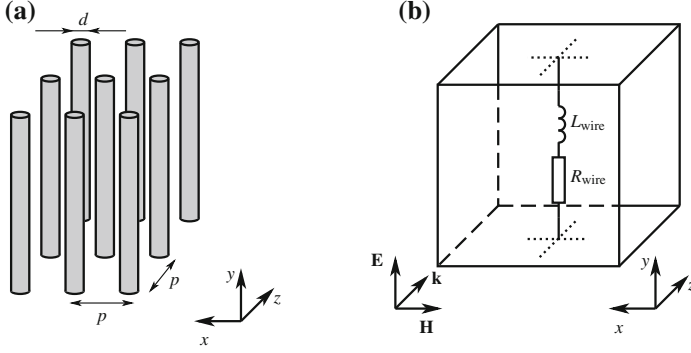
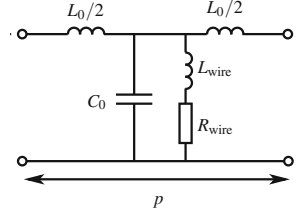


Fig. 3.1 **a** Section of a wire medium (3×3 unit cells) with continuous wire in y -direction, **b** Lumped element representation of the continuous wire medium

Fig. 3.2 Unit cell equivalent circuit of the continuous wire medium



material. For small losses of the host medium and a small unit cell length p , i.e. when the spatial dispersion is neglected, (2.83) and (2.84) yield the effective material parameters

$$\mu_{\text{eff}} = \frac{L_0}{p} = \mu_e, \quad (3.1)$$

$$\varepsilon_{\text{eff}} = \frac{1}{p} \left(C_0 + \frac{1}{j\omega R_{\text{wire}} - \omega^2 L_{\text{wire}}} \right) = \varepsilon_e \left(1 - \frac{\omega_{\text{pe}}^2}{\omega^2 - j\omega\delta_e} \right) \quad (3.2)$$

with a constant effective permeability and an effective permittivity following the Drude dispersion [3, 4]. μ_e and ε_e are the material parameters of the host medium. The Drude dispersion for the effective permittivity is observed since the electric field in y -direction can move free charges in the wire. Since the wire is continuous, charges can move freely (only bound by the wire geometry) in y -direction, equivalent to the free charges in a bulk metal or plasma.

With the per unit length inductance of the straight wire [9]

$$L'_{\text{wire}} = \frac{\mu_e}{2\pi} \ln \frac{2p}{d}, \quad (3.3)$$

the conductivity σ of the wires, and the geometry parameters, the electric plasma frequency and collision frequency (without considering the skin effect) become

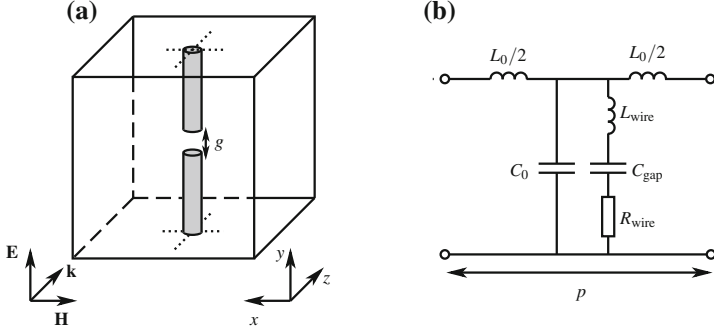


Fig. 3.3 **a** Unit cell of a cut wire medium, **b** Unit cell equivalent circuit of the cut wire medium

$$\omega_{pe} = \sqrt{\frac{2\pi}{\mu_e \epsilon_e p^2 \ln \frac{2p}{d}}}, \quad \delta_e = \frac{8}{\mu_e \sigma d^2 \ln \frac{2p}{d}}. \quad (3.4)$$

For a wire lattice in vacuum, the electric plasma frequency becomes [4]

$$\omega_{pe} = \sqrt{\frac{2\pi c_0^2}{p^2 \ln \frac{2p}{d}}}. \quad (3.5)$$

If the wire is cut as in Fig. 3.3a, the gap with length g introduces a capacitor in series with the wire inductance. This geometry yields the unit cell equivalent circuit in Fig. 3.3b. The effective permeability is not changed compared to the continuous wires while the effective permittivity has the Lorentz form

$$\epsilon_{\text{eff}} = \frac{1}{p} \left(C_0 + \frac{1}{j\omega R_{\text{wire}} - \omega^2 L_{\text{wire}} + 1/C_{\text{gap}}} \right) \quad (3.6)$$

$$= \epsilon_e \left(1 - \frac{\omega_{te}^2 - \omega_{0e}^2}{\omega^2 - \omega_{0e}^2 - j\omega\delta_e} \right). \quad (3.7)$$

The electric resonance frequency becomes

$$\omega_{0e} = \sqrt{\frac{8g}{\mu_e \epsilon_e d^2 p \ln \frac{2p}{d}}} \quad (3.8)$$

and the transition frequency

$$\omega_{te} = \sqrt{\omega_{0e}^2 + \omega_{pe}^2} = \sqrt{\frac{8gp + 2\pi d^2}{\mu_e \epsilon_e p^2 d^2 \ln \frac{2p}{d}}}. \quad (3.9)$$

The derived Drude or Lorentz dispersion only occurs for the electric field component in y -direction, i.e. for a wire orientation as shown in Figs. 3.1a and 3.3a. Hence, the response shows a uniaxial anisotropic behavior with the effective permittivity tensor

$$\bar{\bar{\epsilon}}_{\text{eff}} = \begin{pmatrix} \epsilon_e & 0 & 0 \\ 0 & \epsilon_{\text{wire}} & 0 \\ 0 & 0 & \epsilon_e \end{pmatrix}. \quad (3.10)$$

Additionally, for a not negligible unit cell length p , spatial dispersion has to be taken into account as described above in Sect. 2.4.

3.2 Split-Ring Resonator

A split-ring resonator (SRR) in a three-dimensional unit cell [5] is shown in Fig. 3.4a. With the ring inductance L_{SRR} , the total capacitance between the rings C_{SRR} and the loss resistance R_{SRR} , the unit cell can be described by the model in Fig. 3.4b [10].

If the magnetic field of the incident plane wave is oriented perpendicular to the rings, the unit cell equivalent circuit in Fig. 3.5a can be used to describe the dispersion created by a lattice of split-ring resonators. The rings are modeled by the lossy resonator with L_{SRR} and C_{SRR} . A part of the total magnetic flux Φ_{uc} of the incident wave over the unit cell excites a current in the rings, which is modeled by the transformer consisting of L_{SRR} , L_0 , and the coupling factor S . L_0 represents the permeability μ_e of the host medium. Due to causality (2.44) and (2.45), the shunt capacitance C_0 , which represents the host permittivity ϵ_e , has to be added in the shunt branch. An alternative form of the unit cell with the conversion of the transformer is shown in Fig. 3.5b where the mutual inductance is

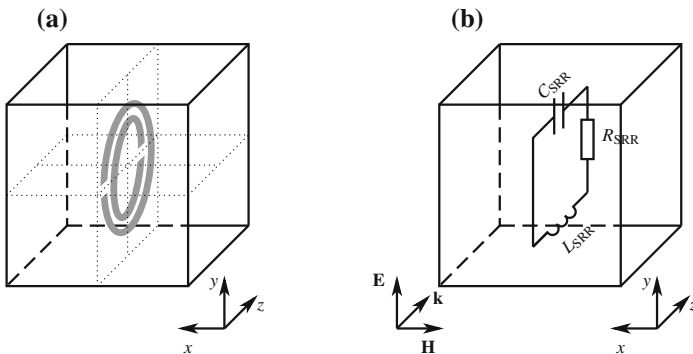


Fig. 3.4 **a** Unit cell of split-ring resonator medium, **b** Lumped element representation of the split-ring resonator

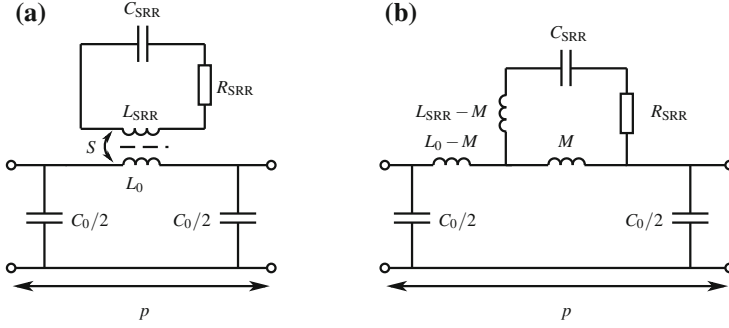


Fig. 3.5 **a** Unit cell equivalent circuit of the split-ring resonator, **b** Transformed unit cell

$$M^2 = S^2 L_0 L_{\text{SRR}}. \quad (3.11)$$

With this transformed unit cell and (2.83) and (2.84), the effective material parameters become (without considering spatial dispersion)

$$\mu_{\text{eff}} = \frac{L_0}{p} \left(1 - \frac{\omega^2 S^2}{\omega^2 - \omega_{0\mu}^2 - j\omega\delta_\mu} \right), \quad (3.12)$$

$$\varepsilon_{\text{eff}} = \frac{C_0}{p} = \varepsilon_e, \quad (3.13)$$

with a Lorentz dispersion for the effective permeability and a constant effective permittivity. The magnetic resonance frequency and damping factor are

$$\omega_{0\mu} = \sqrt{\frac{1}{L_{\text{SRR}} C_{\text{SRR}}}}, \quad \delta_m = \frac{R_{\text{SRR}}}{L_{\text{SRR}}}. \quad (3.14)$$

The transition frequency, where the real part of the effective permeability changes from negative to positive sign, is

$$\omega_{\text{t}\mu}^2 = \frac{\omega_{0\mu}^2}{1 - S^2} = \frac{1}{\left(L_{\text{SRR}} - \frac{M^2}{L_0} \right) C_{\text{SRR}}}. \quad (3.15)$$

It can be seen that the coupling factor S is an important parameter which determines the bandwidth of the negative permeability region as well as the strength of the Lorentz resonance, i.e. the magnitude of the effective permeability near the resonance frequency. S is the amount of magnetic flux coupled into the ring:

$$S = \frac{\Phi_{\text{SRR}}}{\Phi_{\text{uc}}} = \frac{\int_{A_{\text{SRR}}} \mathbf{B}(z) \cdot d\mathbf{A}}{\int_{A_{\text{uc}}} \mathbf{B}(z) \cdot d\mathbf{A}}. \quad (3.16)$$

The total magnetic flux in the yz -plane of the cubic unit cell is

$$\Phi_{\text{uc}} = \int_{z=-p/2}^{p/2} \int_{y=-p/2}^{p/2} B_0 e^{-j\omega\sqrt{\mu_e\epsilon_e}z} dydz \quad (3.17)$$

$$= \frac{2B_0 p}{\omega\sqrt{\mu_e\epsilon_e}} \sin(\omega\sqrt{\mu_e\epsilon_e}p/2). \quad (3.18)$$

The flux that is coupled into the split-ring resonator depends on its size and shape. For a rectangular shape with the length l_{SRR} and the height h_{SRR} , the flux in the ring becomes

$$\Phi_{\text{SRR}\square} = \int_{z=-l_{\text{SRR}}/2}^{l_{\text{SRR}}/2} \int_{y=-h_{\text{SRR}}/2}^{h_{\text{SRR}}/2} B_0 e^{-j\omega\sqrt{\mu_e\epsilon_e}z} dydz \quad (3.19)$$

$$= \frac{B_0 h_{\text{SRR}}}{\omega\sqrt{\mu_e\epsilon_e}} 2 \sin(\omega\sqrt{\mu_e\epsilon_e}l_{\text{SRR}}/2) \quad (3.20)$$

which yields the coupling factor

$$S_{\square} = \frac{h_{\text{SRR}}}{p} \cdot \frac{\sin(\omega\sqrt{\mu_e\epsilon_e}l_{\text{SRR}}/2)}{\sin(\omega\sqrt{\mu_e\epsilon_e}p/2)}. \quad (3.21)$$

In the case of a circular shape with the inner radius r_i , the flux in the ring is

$$\Phi_{\text{SRR}\circ} = \int_{z=-r_i}^{r_i} \int_{y=-\sqrt{r_i^2-z^2}}^{\sqrt{r_i^2-z^2}} B_0 e^{-j\omega\sqrt{\mu_e\epsilon_e}z} dydz = \frac{2\pi B_0 r_i J_1(\omega\sqrt{\mu_e\epsilon_e}r_i)}{\omega\sqrt{\mu_e\epsilon_e}} \quad (3.22)$$

with J_1 denoting the first order Bessel function and hence, the coupling factor becomes

$$S_{\circ} = \frac{\pi r_i}{p} \cdot \frac{J_1(\omega\sqrt{\mu_e\epsilon_e}r_i)}{\sin(\omega\sqrt{\mu_e\epsilon_e}p/2)}. \quad (3.23)$$

In the derivation of (3.21) and (3.23) it is assumed that the phase of the incident magnetic field advances over the length of the split-ring resonator. For a short unit cell with respect to the wavelength, the phase of the incident magnetic flux density $\mathbf{B}(z)$ can be assumed to be constant over the unit cell length p . Hence, the wavenumber of the host material $\omega\sqrt{\mu_e\epsilon_e}$ becomes small and (3.21) can be approximated by

$$S_{\square} \approx \frac{h_{\text{SRR}}l_{\text{SRR}}}{p^2} \quad (3.24)$$

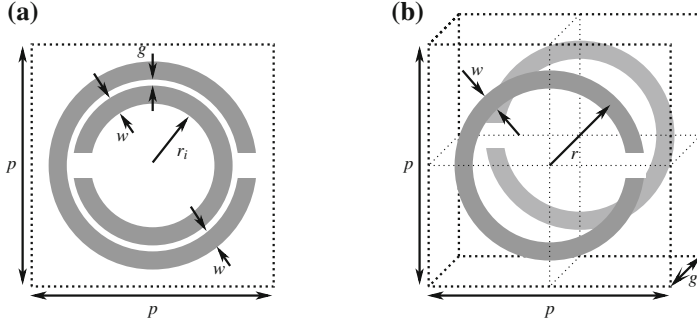


Fig. 3.6 **a** Edge coupled split-ring resonator, **b** Broadside coupled split ring resonator

and (3.23) by

$$S_o \approx \frac{\pi r_i^2}{p^2} \quad (3.25)$$

or independent of the shape [5]

$$S \approx \frac{A_{\text{SRR}}}{A_{\text{uc}}}. \quad (3.26)$$

For a small split length, the magnetic resonance frequency and the damping factor of the edge coupled split-ring resonator in Fig. 3.6a is [5]

$$\omega_{0\mu} = \sqrt{\frac{3p}{\mu_e \epsilon_e \pi r_i^3 \ln \frac{2w}{g}}}, \quad \delta_\mu = \frac{2p\sigma}{\mu_e r_i}, \quad (3.27)$$

by taking the total ring inductance and the gap capacitance between the rings.

For the broadside coupled configuration in Fig. 3.6b, the capacitance C_{SRR} is formed by the rings that face each other at a small distance g , yielding

$$\omega_{0\mu} = \sqrt{\frac{3gp}{2\mu_e \epsilon_e \pi^3 r^4}}. \quad (3.28)$$

A detailed comparison of the edge coupled and broadside coupled split-ring resonator in three-dimensional and planar configuration together with their equivalent circuit elements can be found in [11, 12].

Due to the orientation of the split-ring resonators, the Lorentz dispersion only affects the magnetic field component in x -direction which can be described by the effective uniaxial permeability tensor

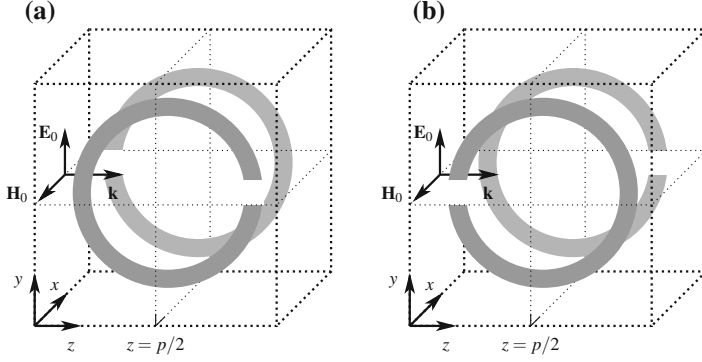


Fig. 3.7 Unit cell (broadside coupled split-ring resonator) with a quasi-symmetry: **a** Original unit cell, **b** Unit cell mirrored at the $z = p/2$ plane

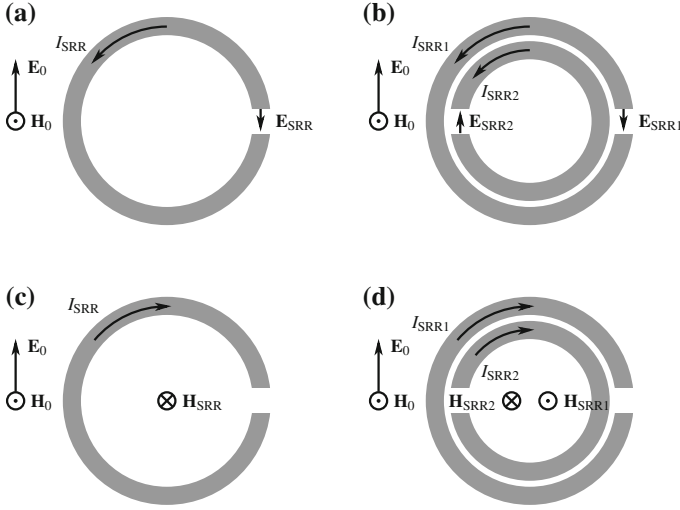


Fig. 3.8 **a/c**: Effect of bi-anisotropy in an unsymmetrical geometry, **b/d**: Cancellation of electromagnetic coupling in a (quasi-) symmetrical geometry

$$\bar{\bar{\mu}}_{\text{eff}} = \begin{pmatrix} \mu_{\text{SRR}} & 0 & 0 \\ 0 & \mu_e & 0 \\ 0 & 0 & \mu_e \end{pmatrix}. \quad (3.29)$$

As depicted in Fig. 3.7 for the broadside coupled split-ring resonator, the investigated unit cells show a geometric quasi-symmetry with respect to the plane $z = p/2$, i.e. the electromagnetic response is approximately the same for the original geometry (Fig. 3.7a) and the mirrored geometry (Fig. 3.7b). Without such a symmetry as in Fig. 3.8a, c, the effect of bi-anisotropy [13, 14] has to be considered. In the unsymmetric configuration, the incident magnetic field \mathbf{H}_0 induces a current I_{SRR} in the

ring which yields an electric field \mathbf{E}_{SRR} over the SRR gap (Fig. 3.8a). This superimposes with the incident electric field \mathbf{E}_0 . Equivalently, the incident electric field \mathbf{E}_0 drives a current in the ring which yields a magnetic field \mathbf{H}_{SRR} that superimposes with the incident magnetic field \mathbf{H}_0 (Fig. 3.8c). This magnetoelectric coupling [15] can be taken into account, if the material equations (2.5) and (2.6) are extended by the bi-anisotropy term ξ :

$$\mathbf{B}(\omega) = \mu_0 [\mathbf{M} + \mathbf{H}_0 + \mathbf{H}_{\text{SRR}}(\mathbf{E}_0)] = \mu_{\text{eff}}(\omega)\mathbf{H}_0 + \xi_{\mu\varepsilon}(\omega)\mathbf{E}_0, \quad (3.30)$$

$$\mathbf{D}(\omega) = \varepsilon_0 [\mathbf{E}_0 + \mathbf{E}_{\text{SRR}}(\mathbf{H}_0)] + \mathbf{P} = \varepsilon_{\text{eff}}(\omega)\mathbf{E}_0 + \xi_{\varepsilon\mu}(\omega)\mathbf{H}_0. \quad (3.31)$$

If the unit cell is geometrically symmetric in propagation direction as in Fig. 3.8b, the incident magnetic field \mathbf{H}_0 induces the same current in each ring which yields an electric field with $\mathbf{E}_{\text{SRR1}} \approx -\mathbf{E}_{\text{SRR2}}$ over each gap of the split-ring resonators. In the case of a small unit cell length, these fields cancel out so that (3.31) becomes

$$\mathbf{D}(\omega) = \varepsilon_0 [\mathbf{E}_0 + \mathbf{E}_{\text{SRR1}}(\mathbf{H}_0) + \mathbf{E}_{\text{SRR2}}(\mathbf{H}_0)] + \mathbf{P} \approx \varepsilon_0\mathbf{E}_0 + \mathbf{P} = \varepsilon_{\text{eff}}(\omega)\mathbf{E}_0. \quad (3.32)$$

As shown in Fig. 3.8d, the same occurs in the symmetric geometry for the incident electric field, where the generated magnetic fields $\mathbf{H}_{\text{SRR1}} \approx -\mathbf{H}_{\text{SRR2}}$ cancel out each other so that (3.30) becomes

$$\mathbf{B}(\omega) = \mu_0 [\mathbf{M} + \mathbf{H}_0 + \mathbf{H}_{\text{SRR1}}(\mathbf{E}_0) + \mathbf{H}_{\text{SRR2}}(\mathbf{E}_0)] \approx \mu_0(\mathbf{M} + \mathbf{H}_0) = \mu_{\text{eff}}(\omega)\mathbf{H}_0. \quad (3.33)$$

Although the effect of bi-anisotropy has been demonstrated here for a split-ring resonator, it has to be considered for any unit cell geometry where magnetoelectric coupling effects inside the unit cell do not cancel out.

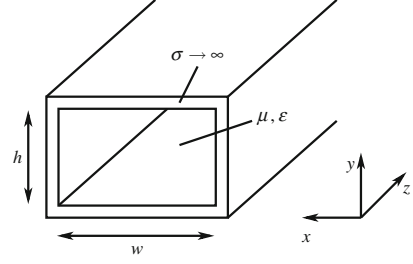
The presented equivalent circuits are valid for a three-dimensional unit cell configuration. However, it is also possible to exploit the split-ring resonator for planar transmission line metamaterials, which offers a further variation of the geometry and the dispersion properties due to the guided wave nature [12].

To manipulate the electric and magnetic response, the wire lattice and split-ring resonators can be combined. Under certain conditions, e.g. if spatial dispersion and bi-anisotropy can be neglected, both can be designed independently so that desired effective material parameters or impedance and phase response can be tailored.

3.3 Hollow Waveguides

The approaches above are based on the manipulation of the electric and magnetic field by the use of particles with a physically finite non-zero size. However, guided wave structures such as hollow waveguides also show frequency dependent properties which can be exploited to design a required electric or magnetic response. Here,

Fig. 3.9 Rectangular hollow waveguide



the description of waveguide dispersion is derived in terms of effective material parameters which can, due to the independent response to the electric and magnetic field of a propagating wave, be combined with the characteristics of the previously presented particles.

The dispersion relation of a rectangular hollow waveguide depicted in Fig. 3.9 for transversal electric (TE) and transversal magnetic (TM) modes is [16]

$$k_z^2 = \omega^2 \mu_{\text{eff}} \epsilon_{\text{eff}} = \omega^2 \mu \epsilon - k_x^2 - k_y^2 = \omega^2 \mu \epsilon - \left(\frac{m\pi}{w} \right)^2 - \left(\frac{n\pi}{h} \right)^2. \quad (3.34)$$

Here, μ and ϵ are the material parameters of the waveguide filling. The wave impedance differs for the TE and TM mode and is [16]

$$Z_{\text{TE}} = \frac{\omega \mu}{k_z}, \quad (3.35)$$

$$Z_{\text{TM}} = \frac{k_z}{\omega \epsilon}. \quad (3.36)$$

Using the relation between effective material parameters, wavenumber, and wave impedance (2.8), (2.10), the transmission line equivalent circuit and effective material parameters can be derived for each mode.

Effective Material Parameters and Transmission Line Model for TE Modes

With (2.8) and (2.10) the effective material parameters for TE modes are

$$\mu_{\text{TE}} = \mu, \quad (3.37)$$

$$\epsilon_{\text{TE}} = \epsilon - \frac{\left(\frac{m\pi}{w} \right)^2 + \left(\frac{n\pi}{h} \right)^2}{\omega^2 \mu} \quad (3.38)$$

with a constant effective permeability represented by the material permeability of the waveguide filling and a dispersive effective permittivity following the Drude dispersion (2.24). The electric plasma frequency

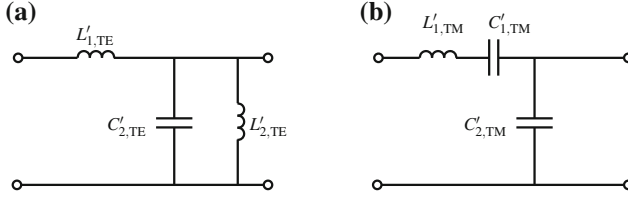


Fig. 3.10 Transmission line model for the wave propagation in a hollow waveguide: **a** TE modes, **b** TM modes

$$\omega_{pe} = \sqrt{\frac{1}{\mu\epsilon} \left[\left(\frac{m\pi}{w} \right)^2 + \left(\frac{n\pi}{h} \right)^2 \right]} \quad (3.39)$$

corresponds to the cutoff frequency of the TE_{mn} mode. Hence, for TE modes, the effective permittivity becomes negative below the cutoff frequency and positive above the cutoff frequency of the TE_{mn} mode.

The distributed impedance and admittance values of the transmission line equivalent circuit are

$$Z'_{se,TE}(\omega) = j\omega\mu_{TE} = j\omega\mu \quad (3.40)$$

representing a distributed inductance $L'_{1,TE}$ in the series branch, and

$$Y'_{sh,TE}(\omega) = j\omega\epsilon_{TE} = j \left(\omega\epsilon - \frac{\left(\frac{m\pi}{w} \right)^2 + \left(\frac{n\pi}{h} \right)^2}{\omega\mu} \right) \quad (3.41)$$

representing a parallel resonator in the shunt branch consisting of the distributed shunt elements $L'_{2,TE}$ and $C'_{2,TE}$ as shown in Fig. 3.10a. This yields the equivalent circuit elements

$$L'_{1,TE} = \mu, \quad (3.42)$$

$$L'_{2,TE} = \frac{\mu}{\left(\frac{m\pi}{w} \right)^2 + \left(\frac{n\pi}{h} \right)^2}, \quad (3.43)$$

$$C'_{2,TE} = \epsilon. \quad (3.44)$$

Effective Material Parameters and Transmission Line Model for TM Modes

Using (2.8) and (2.10), the effective material parameters for the TM_{mn} mode are

$$\mu_{TM} = \mu - \frac{\left(\frac{m\pi}{w} \right)^2 + \left(\frac{n\pi}{h} \right)^2}{\omega^2\epsilon}, \quad (3.45)$$

$$\epsilon_{TM} = \epsilon, \quad (3.46)$$

where the effective permittivity is constant with the filling permittivity, and the effective permeability follows the Drude dispersion (2.23). The magnetic plasma frequency becomes

$$\omega_{p\mu} = \sqrt{\frac{1}{\mu\epsilon} \left[\left(\frac{m\pi}{w} \right)^2 + \left(\frac{n\pi}{h} \right)^2 \right]} \quad (3.47)$$

which is equivalent to the cutoff frequency of the TM_{mn} mode.

The transmission line elements become

$$Z'_{\text{se, TM}}(\omega) = j\omega\mu_{\text{TM}} = j \left(\omega\mu - \frac{\left(\frac{m\pi}{a} \right)^2 + \left(\frac{n\pi}{b} \right)^2}{\omega\epsilon} \right), \quad (3.48)$$

i.e. a series resonators in the series branch, and

$$Y'_{\text{sh, TM}}(\omega) = j\omega\epsilon_{\text{TM}} = j\omega\epsilon \quad (3.49)$$

representing a shunt capacitance, so that the elements in Fig. 3.10b are

$$L'_{1, \text{TM}} = \mu, \quad (3.50)$$

$$C'_{1, \text{TM}} = \frac{\epsilon}{\left(\frac{m\pi}{a} \right)^2 + \left(\frac{n\pi}{b} \right)^2}, \quad (3.51)$$

$$C'_{2, \text{TM}} = \epsilon. \quad (3.52)$$

The hollow waveguide can be loaded, e.g. with particles presented in Sects. 3.1 and 3.2, to further manipulate the magnetic or electric response to the TE or TM mode in the waveguide [17–20].

References

1. M. Zedler, C. Caloz, P. Russer, A 3-d isotropic left-handed metamaterial based on the rotated transmission-line matrix (TLM) scheme. *IEEE Trans. Microw. Theory Tech.* **55**, 2930–2941 (2007)
2. P. Alitalo, S. Tretyakov, Broadband electromagnetic cloaking realized with transmission-line and waveguiding structures. *Proc. IEEE* **99**, 1646–1659 (2011)
3. W. Rotman, Plasma simulation by artificial dielectrics and parallel-plate media. *IRE Trans. Antennas Propag.* **10**, 82–95 (1962)
4. J.B. Pendry, A.J. Holden, D.J. Robbins, W.J. Stewart, Low frequency plasmons in thin-wire structures. *J. Phys. Condens. Matter* **10**(22), 4785 (1998)
5. J. Pendry, A. Holden, D. Robbins, W. Stewart, Magnetism from conductors and enhanced nonlinear phenomena. *IEEE Trans. Microw. Theory Tech.* **47**, 2075–2084 (1999)
6. M.M.I. Saadoun, N. Engheta, A reciprocal phase shifter using novel pseudochiral or ω medium. *Microw. Opt. Technol. Lett.* **5**(4), 184–188 (1992)
7. M. Kafesaki, I. Tsiapa, N. Katsarakis, T. Koschny, C.M. Soukoulis, E.N. Economou, Left-handed metamaterials: The fishnet structure and its variations. *Phys. Rev. B* **75**, (Jun 2007)

8. V.M. Shalaev, W. Cai, U.K. Chettiar, H.-K. Yuan, A.K. Sarychev, V.P. Drachev, A.V. Kildishev, Negative index of refraction in optical metamaterials. *Opt. Lett.* **30**, (December 2005)
9. K. Küpfmüller, *Einführung in die theoretische Electrotechnik*. (Springer, New York, 1959)
10. T. Cui, D. Smith, R. Liu, *Metamaterials: Theory, Design, and Applications*. (Springer, New York, 2009)
11. R. Marqués, F. Mesa, J. Martel, F. Medina, Comparative analysis of edge- and broadside-coupled split ring resonators for metamaterial design—theory and experiments. *IEEE Trans. Antennas Propag.* **51**(10), 2572–2581 (2003)
12. R. Marqués, F. Martín, M. Sorolla, *Metamaterials with Negative Parameters: Theory* (Wiley, Design and Microwave Applications. Wiley Series in Microwave and Optical Engineering, 2008)
13. A. Sihvola, *Electromagnetic Mixing Formulas and Applications* (IEE Publication Series, Institution of Electrical Engineers, 1999)
14. F. Capolino, *Theory and Phenomena of Metamaterials*, *Metamaterials Handbook* (Taylor and Francis, London, 2009)
15. B.D. Tellegen, The gyrator, a new electric network element. *Philips Res. Rep* **3**(2), 81–101 (1948)
16. R. Collin, I. Antennas, P. Society, *Field theory of guided waves*. The IEEE/OUP Series on Electromagnetic Wave Theory (Formerly IEEE Only), Series Editor Series (IEEE Press, New York, 1991)
17. R. Marqués, J. Martel, F. Mesa, F. Medina, Left-handed-media simulation and transmission of em waves in subwavelength split-ring-resonator-loaded metallic waveguides. *Phys. Rev. Lett.* **89**, 183901 (2002)
18. S. Hrabar, J. Bartolic, Z. Sipus, *Miniaturization of rectangular waveguide using uniaxial negative permeability meta-material*, vol. 2 (May 2004), pp. 495–498
19. G. Lubkowski, C. Damm, B. Bandlow, R. Schuhmann, M. Schüßler, T. Weiland, Broadband transmission below the cutoff frequency of a waveguide loaded with resonant scatterer arrays. *IET Microw. Antennas Propag.* **1**(1), 165–169 (2007)
20. M. Maasch, C. Damm, M. Schüßler, E. González-Rodríguez, R. Jakoby, Varactor loaded tunable split ring resonators with simple biasing network. *Ger. Microw. Conf. (GeMIC)* **2011**, 1–4 (2011)

Chapter 4

Extraction of Dispersion Parameters

As demonstrated previously, the propagation of waves in distributed and discrete periodic structures can be described by a set of dispersion parameters such as wavenumber and Bloch impedance or by effective material parameters. In this chapter, different methods to obtain these parameters from a given geometry are introduced and investigated. These methods are either based on the analysis of the scattering parameters of a single mode, from which effective material parameters are calculated, or on the determination of propagating eigenmodes within a periodic structure taking into account the effects of higher order modes not covered by scattering parameter methods.

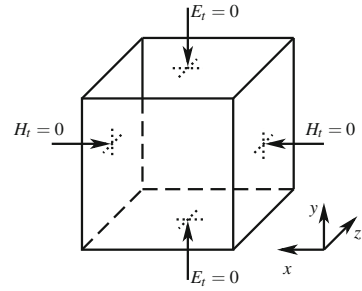
4.1 Extraction from Scattering Parameters

Scattering parameters used to extract dispersion parameters or effective material parameters usually originate from measurements or fullwave simulations. In fullwave simulations of a guided wave structure, the boundary conditions are set according to the host transmission line. For three-dimensional unit cells, the boundary conditions are set as shown in Fig. 4.1 for a plane wave excitation in z -direction. The plane wave excitation is created by perfect magnetic conductor (PMC) boundaries at x_{\min} and x_{\max} as well as perfect electric conductor (PEC) boundaries at y_{\min} and y_{\max} with the tangential components of the magnetic and electric field being zero, respectively. This is equivalent to an infinitely large lattice transversal to the propagation direction z .

4.1.1 *Nicolson–Ross–Weir Extraction Method with Phase Reconstruction*

In the Nicolson–Ross–Weir (NRW) method [1, 2] it is assumed that the region between the ports of a two-port network is filled with a homogenous material with μ_{eff}

Fig. 4.1 Boundary conditions for the scattering parameter simulation of three-dimensional unit cells



and ε_{eff} . This two-port network can be a guided wave circuit, e.g. a loaded microstrip line, but also a three-dimensional configuration such as a split-ring resonator unit cell. Using the relation between chain parameters and scattering parameters with the real reference impedance $Z_{01} = Z_{02} = Z_0$ and $\{Z_0\} = 0$ [3], the characteristic impedance and propagation constant become

$$Z_c = \pm Z_0 \sqrt{\frac{(1 + S_{11})^2 - S_{12}S_{21}}{(1 - S_{11})^2 - S_{12}S_{21}}} \quad (4.1)$$

and

$$\gamma l = \gamma n p = (\alpha + j\beta)l = \cosh^{-1} \frac{1 - S_{11}^2 + S_{21}^2}{2S_{21}} + j2m\pi \quad (4.2)$$

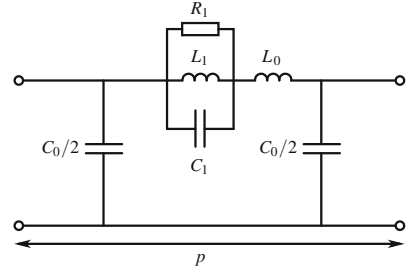
where l is the length of the extracted structure consisting of n unit cells with the periodicity p . The solution for the phase $\beta l = \beta n p$ is ambiguous with integer multiples of 2π due to the periodicity of the inverse hyperbolic cosine function for imaginary arguments. To find the correct phase branch, causality and the Kramers–Kronig relation (2.82) can be applied [4, 5]. The non-ambiguous attenuation constant α is used to predict the imaginary part β_{KK} of the propagation constant. For numerical data this can only be realized for a limited bandwidth yielding an approximation for $\beta_{\text{KK}} \approx \beta$. However, this approximation is tolerable because only the integer value m has to be found.

As an example, the extraction of effective material parameters is performed for the unit cell depicted in Fig. 4.2. The effective permeability follows the Lorentz dispersion while the effective permittivity is constant. Such a response can be created with an SRR loaded transmission line or an SRR array in a homogenous medium. Due to the constant effective permittivity and the resonant effective permeability and the negative permeability region, a stop band between 5.0 and 7.1 GHz is expected.

To obtain the effective material parameters, the scattering parameters of an array consisting of 12 unit cells (to investigate phase wrapping effects) are calculated¹ and the characteristic impedance (4.1) and propagation constant (4.2) with the unknown

¹These scattering parameters usually originate from fullwave simulations or measurements where they cannot be obtained analytically.

Fig. 4.2 Unitcell with Lorentz–Drude dispersion ($L_1 = L_0 = 1$ nH, $C_1 = 1$ pF, $R_1 = R_2 = 1000$ Ω , $C_0 = 3.65$ fF, $p = 0.4$ mm)



branch parameter m can be determined. From these the effective material parameters can be calculated with

$$\mu_{\text{eff}} = \frac{1}{j\omega l} Z_c \gamma p, \quad (4.3)$$

$$\varepsilon_{\text{eff}} = \frac{1}{j\omega l} \frac{\gamma p}{Z_c}. \quad (4.4)$$

For the unit cell in Fig. 4.2 this yields the phase and the effective material parameters in Fig. 4.3 for different phase branches $m = -2 \dots +2$ with the correct branch $m = 0$ for the considered frequency band. The unit cell phase shift βp is ambiguous with multiple of $2\pi/n = 2\pi/12$ as expected from (4.2). This strongly influences the effective material parameters where only the solution for $m = 0$ shows the correct dispersion with a constant effective permittivity and the correct magnetic resonance and transition frequency.

In Fig. 4.4, different extractions of the unit cell phase shift are shown for a wide frequency band. The uncorrected dispersion is obtained without any correction of the phase branch. Without phase correction, the phase branch depends on the implementation of the inverse hyperbolic cosine function in (4.2). Here, the extracted phase βl is between $-\pi$ and $+\pi$ so that the unit cell phase shift βp lies between $-\pi/12$ and $+\pi/12$ and a wrapping of the phase occurs near the magnetic resonance frequency at 5 and at 22 GHz. Applying the attenuation constant α in the Kramers–Kronig relation (2.82) the phase constant β_{KK} in Fig. 4.4 can be calculated. Since the integration limits for numeric and measured data are finite, this is an approximation of the correct phase constant, especially close to the limits of the simulation or measurement band. However, the accuracy is sufficient to determine the correct phase branch

$$m(\omega) = \text{round} \left\{ \frac{[\beta_{\text{KK}}(\omega) - \beta(\omega)]l}{2\pi} \right\} \quad (4.5)$$

shown in Fig. 4.5.

With the corrected phase the effective material parameters can be calculated. Figure 4.6 shows the effective material parameters of a 12 unit cell array of the configuration in Fig. 4.2 using the uncorrected phase from Fig. 4.4. The real part of

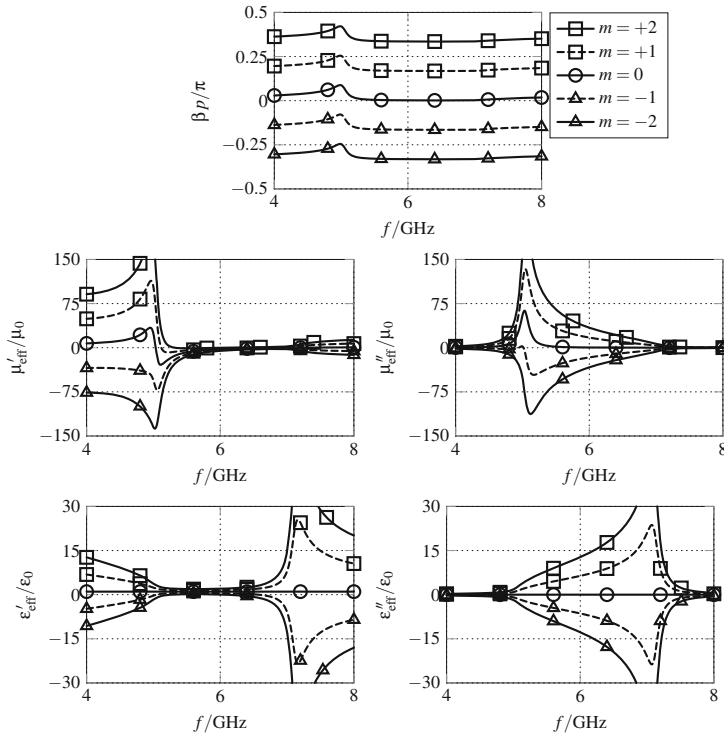


Fig. 4.3 Extracted unit cell phase shift and effective material parameters of a Lorentz material for different phase branches m

Fig. 4.4 Unit cell phase shift of a Lorentz material extracted from 12 unit cells: Comparison of the phase without correction, result of Kramers–Kronig approximation (2.82), and the corrected phase

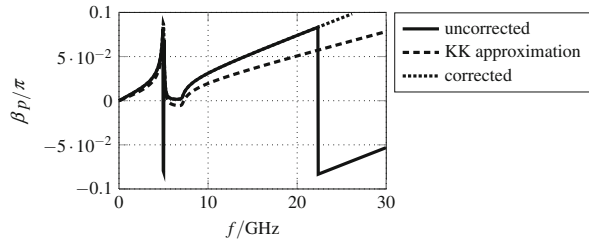
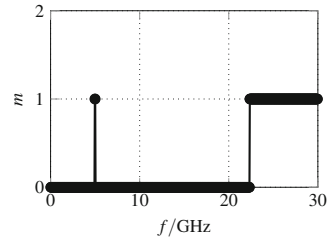


Fig. 4.5 Phase branch of a Lorentz material extracted from 12 unit cells using the Kramers–Kronig relation for the phase constant



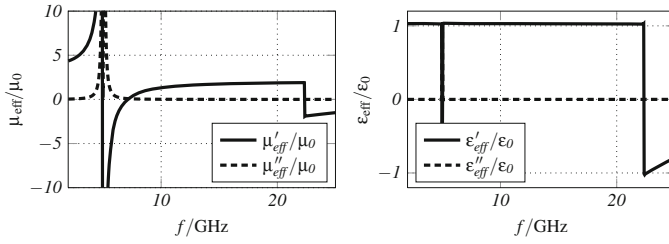


Fig. 4.6 Uncorrected effective material parameters of a Lorentz material extracted from 12 unit cells

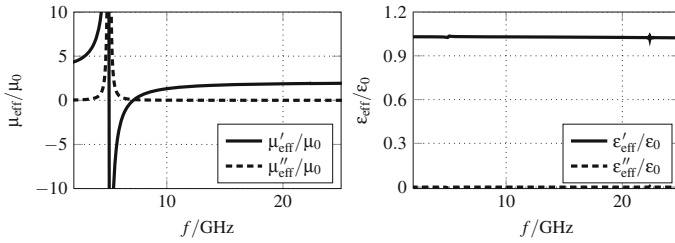


Fig. 4.7 Effective material parameters of a Lorentz material extracted from 12 unit cells after correction of the phase branch m from Fig. 4.5

the effective material parameters shows discontinuities near the magnetic resonance frequency of 5 GHz. Furthermore, due to the phase wrapping at 22 GHz, the material parameters differ from the magnetic Lorentz response and constant effective permittivity as expected from the unit cell circuit.

Using the correct phase branch m from Fig. 4.5, the effective material parameters in Fig. 4.7 are obtained. They show the response of a lossy magnetic Lorentz material following (2.17) and a constant effective permittivity.

4.1.2 Consideration of Higher Order Modes in Scattering Parameters

Since the scattering parameters of a two-port circuit describe the propagation of only the fundamental mode, a propagation of higher order modes is not considered in the conventional NRW method where a fullwave simulation or measurement is performed for a single mode and a single unit cell. However, these higher order modes are excited by discontinuities in the unit cell and can significantly contribute to the propagation inside a lattice even if they are evanescent modes. This becomes more important the closer geometric discontinuities are to the port planes. One possibility to take this higher order mode coupling into account is to perform a fullwave simulation

Fig. 4.9 Cut wire unit cell
(dimensions: $a = 10$ mm,
 $d = 1$ mm, $g = 0.1$ mm)

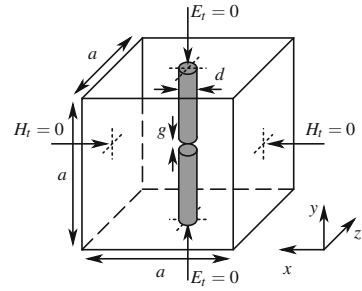
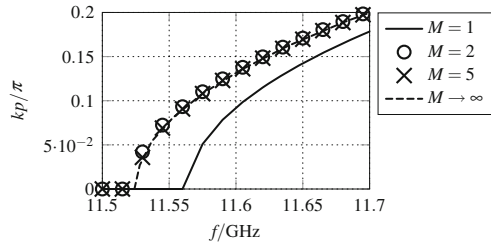


Fig. 4.10 Unit cell phase shift of a wire resonator extracted from scattering parameters of a 10 unit cell array and eigenmode solver



from the eigenmode solver result ($M \rightarrow \infty$). This discrepancy is caused by coupling of higher order modes, excited by the discontinuity formed by the wire. If two modes are taken into account ($M = 2$), the dispersion corresponds to the eigenmode result, i.e. for this specific configuration already two modes are adequate to describe the dispersion characteristic with a high accuracy compared to the eigenmode result where all higher modes ($M \rightarrow \infty$) are considered. The Bloch impedance for this example is not presented here. It can, however, be extracted using (4.1).

The electric and magnetic field distribution in the port plane obtained with the full-wave eigenmode solver with $M \rightarrow \infty$ is shown in Fig. 4.11. It represents the electric and magnetic field of the propagating wave within an infinite lattice at a frequency of 11.54 GHz. The field distribution does not accord to a plane wave propagation which is assumed if only the fundamental mode with $M = 1$ is taken into account. The electric field mainly has components in vertical direction parallel to the wire but is not constant over the port plane. Furthermore, the magnetic field is not constant over the port plane and it has additional components in the propagation direction z . The discrepancy between the plane wave excitation and the actual propagating mode is responsible for the shift of the dispersion diagram in Fig. 4.10.

For the given example, the relative error

$$\epsilon(\omega) = \frac{k - k_{\text{eigenmode}}}{k_{\text{eigenmode}}} \quad (4.8)$$

over the frequency is shown in Fig. 4.12 for different numbers of considered modes in a 10-unit cell array. The largest error occurs close to the transition frequency of 11.52 GHz. If only the fundamental mode is considered, the error in the frequency

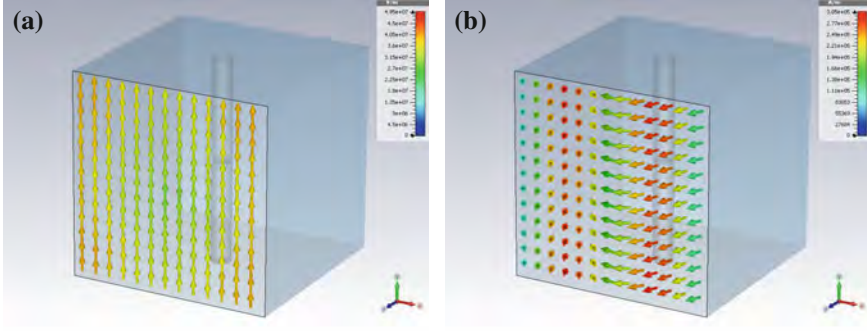
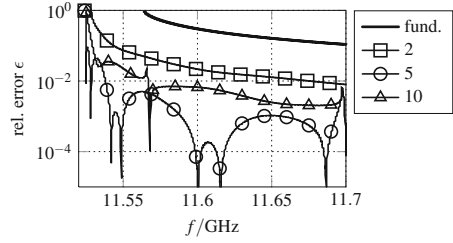


Fig. 4.11 Eigenmode field solution of the unit cell from Fig. 4.9 at 11.54 GHz: **a** Electric field distribution, **b** Magnetic field distribution

Fig. 4.12 Relative error compared to the fullwave eigenmode solution of 10 unit cells and different numbers of considered modes



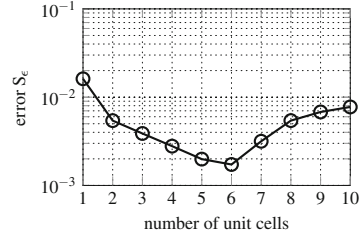
band of interest is larger than 10 % compared to the fullwave eigenmode result. By considering only one more mode, the error can be decreased by a factor of 10.

A second parameter that affects the accuracy of this method is the number of unit cells used in the concatenation to imitate the perfect periodic structure. The truncation of the array causes an error which can be expressed by the mean squared error normalized to the number N of investigated frequency points

$$S_{\epsilon} = \frac{1}{N} \sqrt{\sum_{n=1}^N \epsilon(\omega_n)^2} = \frac{1}{N} \sqrt{\sum_{n=1}^N \left(\frac{k(\omega_n) - k_{\text{eigenmode}}}{k_{\text{eigenmode}}} \right)^2}. \quad (4.9)$$

Figure 4.13 shows S_{ϵ} for different unit cell numbers. Up to 6 unit cells, the total error is reduced by a factor of 10 due to the better approximation of the periodic array. For 7 unit cells and above the total error increases. This error is caused by the NRW extraction method and is introduced by the phase wrapping that occurs in the considered frequency band for longer arrays. Since kp is numerically extracted from scattering parameter results, numerical errors occur which become significant close to the phase wrapping points, i.e. close to phase shifts of integer multiples of 2π . The higher the number of concatenated unit cells, the more wrapping points occur in the considered frequency band which increases the total error of the extracted phase.

Fig. 4.13 Normalized mean square error compared to the fullwave eigenmode solution for 2 considered modes and different unit cell numbers



For highly accurate predictions of the dispersion properties, care has to be taken concerning the error source. Errors can originate from the disregard of higher order mode coupling or from the extraction algorithm like the NRW method in form of numerical errors. In the case of a fullwave simulation, errors can additionally be caused by the meshing of the unit cell geometry or numerical errors in the solution of the discrete Maxwell's equations during the computation.

Although errors are introduced by the truncation of the array, in the presented example the truncation error is smaller than the error caused by neglecting higher order modes. Furthermore, dielectric and magnetic losses can be considered with the scattering parameter method which is not possible in most commercial fullwave eigenmode solvers. Hence, complex dispersion parameters and complex effective material parameters can be obtained.

4.1.3 Eigenmode Determination from Simulated Scattering Parameters

In the previously presented method, an array consisting of an infinite number of unit cells has to be approximated by a truncated array. The introduced truncation error can be avoided by applying the periodic boundary condition [6]

$$b_1 = a_2 e^{-jkp} \quad (4.10)$$

$$b_2 = a_1 e^{jkp} \quad (4.11)$$

to the scattering transfer matrix \mathbf{T} with

$$\begin{pmatrix} \mathbf{b}_1 \\ \mathbf{a}_1 \end{pmatrix} = \mathbf{T} \cdot \begin{pmatrix} \mathbf{a}_2 \\ \mathbf{b}_2 \end{pmatrix} = \begin{pmatrix} \mathbf{T}_{11} & \mathbf{T}_{12} \\ \mathbf{T}_{21} & \mathbf{T}_{22} \end{pmatrix} \cdot \begin{pmatrix} \mathbf{a}_2 \\ \mathbf{b}_2 \end{pmatrix}, \quad (4.12)$$

which contains the coupling between all considered modes. As proposed in [7–9], by calculating the eigenmodes of the transfer matrix, the dispersion diagram of all modes, including the superposition of the fundamental and all considered higher order modes (4.6) and (4.7) can be obtained. \mathbf{a}_i and \mathbf{b}_i are vectors of the incident and reflected normalized waves for each port mode. \mathbf{T}_{ij} are the scattering transfer matrices for all modes between port i and port j so that the transfer matrix becomes

$$\begin{pmatrix} b_1^{(1)} \\ b_1^{(2)} \\ \vdots \\ b_1^{(M)} \\ a_1^{(1)} \\ a_1^{(2)} \\ \vdots \\ a_1^{(M)} \end{pmatrix} = \begin{pmatrix} T_{11}^{(11)} & T_{11}^{(12)} & \dots & T_{11}^{(1M)} & T_{12}^{(11)} & T_{12}^{(12)} & \dots & T_{12}^{(1M)} \\ T_{11}^{(21)} & T_{11}^{(22)} & \dots & T_{11}^{(2M)} & T_{12}^{(21)} & T_{12}^{(22)} & \dots & T_{12}^{(2M)} \\ \vdots & \vdots & \ddots & \vdots & \vdots & \vdots & \ddots & \vdots \\ T_{11}^{(M1)} & T_{11}^{(M2)} & \dots & T_{11}^{(MM)} & T_{12}^{(M1)} & T_{12}^{(M2)} & \dots & T_{12}^{(MM)} \\ T_{21}^{(11)} & T_{21}^{(12)} & \dots & T_{21}^{(1M)} & T_{22}^{(11)} & T_{22}^{(12)} & \dots & T_{22}^{(1M)} \\ T_{21}^{(21)} & T_{21}^{(22)} & \dots & T_{21}^{(2M)} & T_{22}^{(21)} & T_{22}^{(22)} & \dots & T_{22}^{(2M)} \\ \vdots & \vdots & \ddots & \vdots & \vdots & \vdots & \ddots & \vdots \\ T_{21}^{(M1)} & T_{21}^{(M2)} & \dots & T_{21}^{(MM)} & T_{22}^{(M1)} & T_{22}^{(M2)} & \dots & T_{22}^{(MM)} \end{pmatrix} \cdot \begin{pmatrix} a_2^{(1)} \\ a_2^{(2)} \\ \vdots \\ a_2^{(M)} \\ b_2^{(1)} \\ b_2^{(2)} \\ \vdots \\ b_2^{(M)} \end{pmatrix}. \quad (4.13)$$

The obtained result is a vector \mathbf{U} of eigenvalues. The propagating eigenmodes are identified with $|U_m| = 1$ yielding the phase $k_m p = \angle U_m$.

This method is applied to the cut wire unit cell and the extracted dispersion diagram is shown in Fig. 4.14. Like in the multimode-circuit method above, only 2 modes are necessary to significantly increase the accuracy of the phase extraction of this unit cell configuration, which is close to the solution obtained from the fullwave eigenmode simulation. This is confirmed by the normalized mean squared error in Fig. 4.15. With two considered modes, the total relative error becomes 2×10^{-3} while an increase above 5 unit cells does not yield a further reduction of the error.

This approach is similar to the one described in Sect. 4.1.2. The main difference is the boundary condition of the scattering parameter matrix. Since a periodic boundary condition is applied, i.e. implicitly the array is infinitely long, a truncation error does not occur. However, an extraction of the Bloch impedance and hence, of effective material parameters, is not possible.

Fig. 4.14 Unit cell phase shift obtained with an eigenmode analysis of the multimode scattering parameters

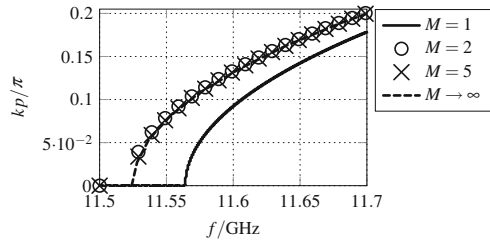
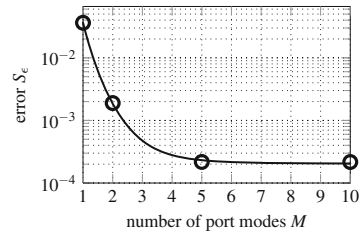


Fig. 4.15 Normalized mean squared error compared to the fullwave eigenmode solution for different unit cell numbers



4.2 Fullwave Eigenmode Computation

To consider all higher order modes in an infinitely long periodic lattice, the periodic boundary condition (4.6)–(4.7) can be applied in the fullwave simulation of a single unit cell. With a varying unit cell phase shift $kp = -\pi \dots \pi$ between the unit cell interface planes at z_{\min} and z_{\max} , the field distribution and the eigenfrequencies of the propagating modes can be calculated. With the eigenfrequencies, the dispersion diagram can be constructed. On the other hand, the field distribution at each eigenfrequency can be used to extract information about the Bloch impedance or the effective material parameters by the use of averaging methods. Furthermore, this field information can be used to compute the farfield of periodic antennas, such as leaky-wave antennas or transmit arrays.

4.2.1 Bloch Impedance Extraction by Field Averaging

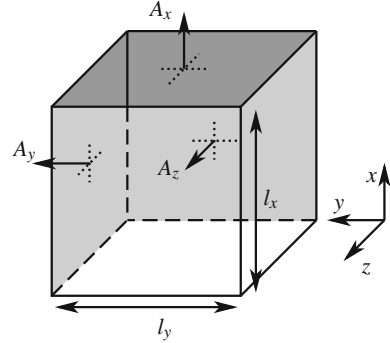
The fullwave eigenmode solution of a unit cell provides information about the distribution of the electric and magnetic fields in each point of a unit cell at a certain eigenfrequency. However, a set of Bloch parameters Z_B and k or effective material parameters μ_{eff} and ε_{eff} , which describe the response of the complete unit cell, is preferred. For that, a homogenization or averaging of the local electric and magnetic responses has to be performed yielding the field components $\langle \mathbf{E} \rangle$, $\langle \mathbf{D} \rangle$, $\langle \mathbf{H} \rangle$, and $\langle \mathbf{B} \rangle$ which now represent the electromagnetic response of the complete unit cell. These averaged fields can be used to calculate the effective material parameters of the unit cell or the Bloch impedance.

An overview over different field homogenization methods and the averaged field components is depicted in Table 4.1 for a Bloch wave propagating in z -direction. These homogenization methods rely on averaging different field components and flux components to obtain either the effective material parameters or the Bloch impedance from which, with the periodic boundary condition and its phase shift, the effective

Table 4.1 Overview of field averaging methods to extract the Bloch impedance or the effective material parameters

	Pendry [10]	Smith [11]	Simovski [12, 13]	Acher [14, 15]	Boscolo [16, 17]
Z_B	–	$\frac{\frac{1}{l_x} \int_{l_x} \mathbf{E} \cdot d\mathbf{s}}{\frac{1}{l_y} \int_{l_y} \mathbf{H} \cdot d\mathbf{s}}$	$\frac{\int_{A_z} E_t dA}{\int_{A_z} H_t dA}$	–	$\frac{\int_{A_z} z_B \text{Re}\{\tilde{S}_z\} dA}{\int_{A_z} \text{Re}\{\tilde{S}_z\} dA}$
μ_{eff}	$\frac{\frac{1}{A_y} \int_{A_y} \mathbf{B} \cdot d\mathbf{A}}{\frac{1}{l_y} \int_{l_y} \mathbf{H} \cdot d\mathbf{s}}$	–	–	$\frac{\frac{1}{V} \int_V B_y dV}{\frac{1}{A_x} \int_{A_x} H_y dA}$	–
ε_{eff}	$\frac{\frac{1}{A_x} \int_{A_x} \mathbf{D} \cdot d\mathbf{A}}{\frac{1}{l_x} \int_{l_x} \mathbf{E} \cdot d\mathbf{s}}$	–	–	$\frac{\frac{1}{A_x} \int_{A_x} D_x(\mathbf{r}) dA}{\frac{1}{V} \int_V E_x(\mathbf{r}) dV}$	–

Fig. 4.16 Lines and surfaces for the integrals of the field averaging methods



material parameters can be calculated. The surfaces and edges of the unit cell used in the averaging are depicted in Fig. 4.16.

The field averaging method by Pendry et al. [10] uses averages of the local fluxes $\mathbf{D}(\mathbf{r}, \omega)$ and $\mathbf{B}(\mathbf{r}, \omega)$ over the unit cell surfaces and averages of the local fields $\mathbf{E}(\mathbf{r}, \omega)$ and $\mathbf{H}(\mathbf{r}, \omega)$ on the unit cell edges to directly obtain the effective material parameters. The flux integration surfaces cannot intersect with conducting elements such as continuous wires [11]. This is a crucial limitation of this method because the effective material parameters of unit cells containing a conducting connection between unit cells in x -direction cannot be calculated.

This limitation is overcome by the approach by Smith et al. [11] where the Bloch impedance is calculated by the ratio of the line averages of $\mathbf{E}(\mathbf{r}, \omega)$ and $\mathbf{H}(\mathbf{r}, \omega)$. However, this method requires an infinite lattice in the xy -plane. In bounded structures such as hollow waveguides this method fails since the line integral of the electric field of the unit cell edges yields zero.

As the method by Smith, the approach by Simovski et al. [12, 13] uses averaged electric and magnetic fields to calculate the Bloch impedance for an excitation with a linear wave. Averaging of the transversal components of $\mathbf{E}(\mathbf{r}, \omega)$ and $\mathbf{H}(\mathbf{r}, \omega)$ is performed over the input plane A_z of the unit cell. This method fails for the propagation of higher order modes; e.g. for the TE_{20} mode in a hollow wave guide, the integration of the electric fields over the input plane yields a zero average field.

The method by Acher et al. [14, 15] is (as Pendry's approach) based on the ratio of averaged flux- and field values to directly calculate effective material parameters. Averaging is performed over the unit cell surfaces and volume. Since the integration surface of the flux $\mathbf{D}(\mathbf{r}, \omega)$ is the same as in Pendry's approach, it shows the same limitations concerning a conductive element between different unit cells.

The method by Boscolo [16] originally has been applied to two-dimensional photonic crystals. It relies on the point wise calculation of the local impedances $z_B(\mathbf{r})$ which are then averaged over the input width. Similarly, the extension for a three-dimensional unit cell [17]

$$Z_B = \frac{\int_{A_z} z_B(\mathbf{r}, \omega) \bar{S}_z(\mathbf{r}, \omega) dA}{\int_{A_z} \bar{S}_z(\mathbf{r}, \omega) dA} \quad (4.14)$$

employs the local impedances

$$z_B(\mathbf{r}, \omega) = \frac{E_t(\mathbf{r}, \omega)}{H_t(\mathbf{r}, \omega)} = \frac{2\bar{S}_z(\mathbf{r}, \omega)}{|H_t(\mathbf{r}, \omega)|^2} = \frac{|E_t(\mathbf{r}, \omega)|^2}{2\bar{S}_z(\mathbf{r}, \omega)} \quad (4.15)$$

in the A_z -plane which are averaged with the z -component of the time averaged Poynting vector

$$\bar{\mathbf{S}}(\mathbf{r}, \omega) = \frac{1}{2} \mathbf{E}(\mathbf{r}, \omega) \times \mathbf{H}^*(\mathbf{r}, \omega) \quad (4.16)$$

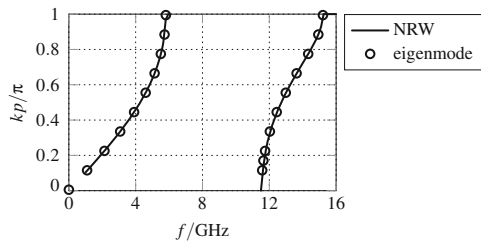
in the A_z -plane as weighting function.

As an example, the method of Boscolo is applied to the cut wire unit cell from Fig. 4.9. The field distribution is calculated using the fullwave eigenmode solver for different unit phase shifts as described above in Sect. 4.2. A comparison of the dispersion diagram obtained with the Nicolson–Ross–Weir method and the eigenmode simulation is shown in Fig. 4.17 with a good agreement between both methods. From the field results for each eigenmode, the Bloch impedance is calculated using the averaging method by Boscolo and compared to the methods by Smith and Simovski, respectively. From the phase shift and the real part of the Bloch impedance, the real part of the effective material parameters is obtained.

Figure 4.18 shows the extracted Bloch impedance and effective material parameters using the methods by Smith, Simovski and Boscolo compared to the result obtained with the NRW extraction. The best agreement can be seen between the methods of Smith and Boscolo. The method by Simovski shows a strong difference due to the partial cancellation of higher order modes. However, a general conclusion about the preferred averaging method cannot be drawn because results depend on the geometry and related to that, the numerical errors for the specific excitation and geometry.

A common drawback of averaging methods based on eigenmode results is that losses cannot be taken into account. Furthermore, these methods provide information about the transmission bands. However, since only the field distribution of

Fig. 4.17 Dispersion diagram of the cut wire unitcell obtained with different extraction methods



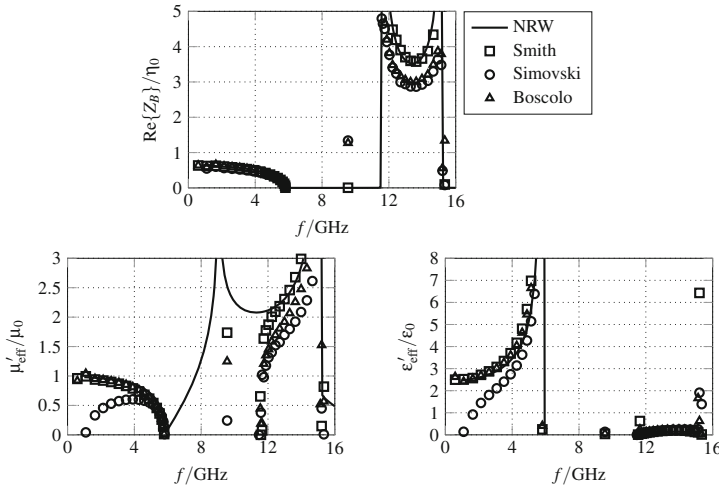


Fig. 4.18 Real part of the effective material parameters of the cut wire unit cell obtained with different field averaging methods

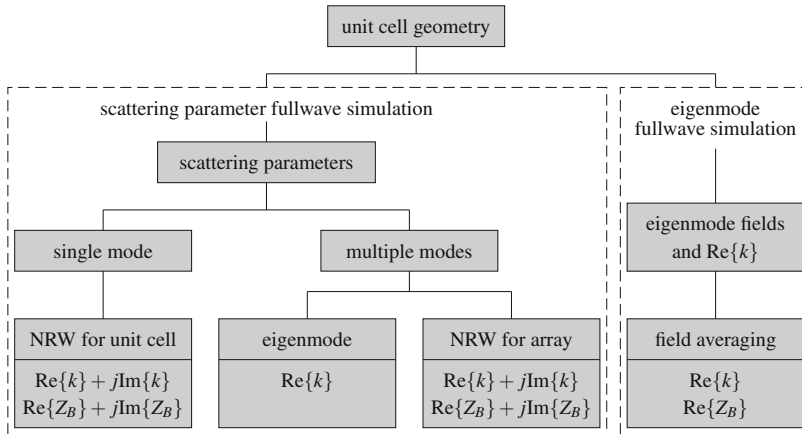


Fig. 4.19 Overview of extraction methods based on the simulation of scattering parameters and eigenmode field of a single unit cell

propagating eigenmodes can be calculated with a fullwave eigenmode method, Bloch parameters within the stop bands cannot be determined.

A comprehensive investigation and comparison of different field averaging methods can be found in [18].

A summary of the presented extraction methods is depicted in Fig. 4.19. A full-wave simulation of the unit cell geometry is performed. This yields scattering parameters for all considered modes (approximation with $M < \infty$) or the field distribution of eigenmodes ($M \rightarrow \infty$). The NRW method for a single mode and single unit cell does

not consider the propagation of any higher order modes and yields complex dispersion parameters, i.e. information about propagation bands and stop bands including losses. The eigenmode method for multiple modes takes higher order mode coupling into account but does not yield any information about the Bloch impedance or dispersion properties within the stop band. The NRW method for arrays with multiple modes that has been developed within this work considers losses and yields dispersion parameters in the propagation bands and stop bands based on the simulation of a single unit cell.

The eigenmode fullwave methods consider all higher order modes. The purely real unit cell phase shift is the boundary condition yielding the eigenfrequencies and the associated electric and magnetic field distribution. However, due to the periodic boundary condition with a purely real wavenumber, losses and the stop band behavior cannot be determined. Using field averaging methods, the real part of the Bloch impedance and with that, the real part of the effective material parameters, can be extracted.

For applications where the knowledge of the complex dispersion parameters, i.e. complex wavenumber and Bloch impedance or complex effective material parameters, is important, only the NRW methods for a single and multiple modes yield sufficient results with the downside of an approximation of the higher order mode propagation. On the contrary, if a precise prediction of the field distribution including higher order modes is of interest, the eigenmode fullwave simulation is preferably used. The extraction of the Bloch impedance by field averaging of the eigenmode field results strongly depends on the geometry of the particle and host medium.

4.2.2 *Farfield Computation from Eigenmode Results*

The farfield computation of long periodic arrangements like leaky-wave antennas with a high level of geometric details but a large overall size often provokes problems regarding simulation time and memory limitations if the structure is simulated in the form of a complete array. On the other hand, a scattering parameter simulation of a single unit cell can provide information about the dispersion characteristics and nearfield distribution but it does not consider higher order mode coupling. To avoid such limitations, conventional farfield transformation approaches to predict the radiation pattern of leaky-wave antennas presented in [19] consider an isotropic point source or omit the field distribution of a single element [20], which reduces the accuracy of the farfield pattern result.

Here it is proposed to employ the field distribution of the eigenmodes as elements for the farfield transformation. Information about the wave propagation in an infinite periodic array can be obtained using a fullwave eigenmode solver including the electric and magnetic nearfield distribution and higher order mode coupling between adjacent unit cells. The field distribution of the unit cell is concatenated in the direction of the guided wave to construct the near field distribution of a large array from which the detailed farfield pattern can be obtained [21].

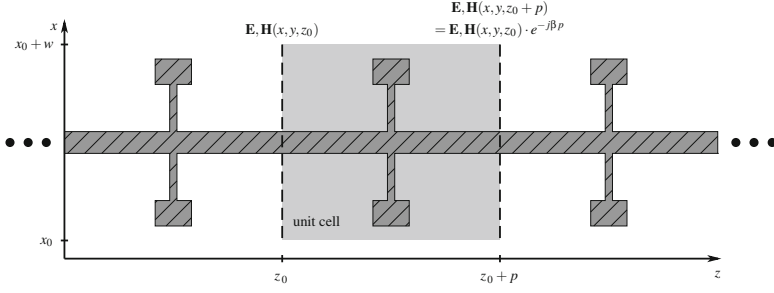


Fig. 4.20 Planar unit cell with periodic boundary condition in z -direction

Due to the periodicity of the unit cell in z -direction as shown in Fig. 4.20, electric and magnetic fields follow (4.6)–(4.7) so that with losses, expressed by the attenuation constant α , the fields of the guided wave are

$$\mathbf{E}, \mathbf{H}(x, y, z) = \mathbf{E}, \mathbf{H}(x, y, z - mp) \cdot e^{-(\alpha + j\beta)mp}. \quad (4.17)$$

Thus, if the field distribution \mathbf{E}_0 and \mathbf{H}_0 of a single unit cell is known from the eigenmode simulation, the field distribution of an array consisting of N unit cells can be determined by

$$\mathbf{E}, \mathbf{H}(x, y, z + np) = \sum_{n=0}^{N-1} \mathbf{E}_0, \mathbf{H}_0(x, y, z) \cdot e^{-(\alpha + j\beta)np}. \quad (4.18)$$

For a leaky-wave antenna as shown in Fig. 4.21, the field distribution $\mathbf{E}, \mathbf{H}(x, y_0, z)$ in the aperture plane $y = y_0$ is Fourier transformed to obtain the plane wave spectrum [22]

$$\mathbf{f}(k_x, k_z) = \int_{Np} \int_w \mathbf{E}(x, y_0, z) e^{j(k_x x + k_z z)} dx dz \quad (4.19)$$

and the electric farfield pattern of the leaky-wave antenna with

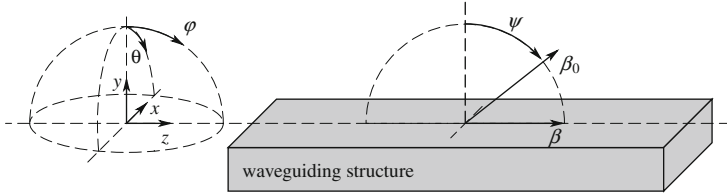


Fig. 4.21 Leaky-wave antenna with guided wave propagating in z -direction

$$\tilde{\mathbf{E}}(r, \theta, \varphi) = j \frac{k_0 e^{-jk_0 r}}{2\pi r} \mathbf{f}(k_x, k_z) \cos \theta. \quad (4.20)$$

Here, k_0 is the wavenumber in free space and r is the distance from the antenna in the farfield. Hence, to calculate the farfield pattern of periodic leaky-wave antennas, it is possible to use the result of the field distribution $\mathbf{E}_0, \mathbf{H}_0$ obtained from an eigenmode simulation of a single unit cell instead of simulating an array consisting of a large number of unit cells. This method considers the full higher order mode coupling. However, usually fullwave eigenmode solvers cannot take metallic, dielectric, or radiation losses into account so that it has to be set manually for the calculation of the farfield pattern. Furthermore, truncation effects of the excitation in the first and last unit cell are not taken into consideration, since the simulated unit cell is part of an infinitely long periodic array. For most applications, however, the unit cell number of the leaky-wave antenna is sufficiently large so that the excitation merely influences the radiation pattern.

The farfield pattern (4.20) can be rewritten to the form

$$\tilde{\mathbf{E}}(r, \theta, \varphi) = j \frac{k_0 e^{-jk_0 r}}{2\pi r} \cos \theta \cdot \mathbf{f}_0(k_x, k_z) \sum_{n=0}^{N-1} e^{np(jk_0 \sin \theta \sin \varphi - \alpha - j\beta)} \quad (4.21)$$

showing that the plane wave spectrum

$$\mathbf{f}_0(k_x, k_z) = \int_p \int_w \mathbf{E}_0(x, y_0, z) e^{j(k_x x + k_z z)} dx dz \quad (4.22)$$

of the unit cell is multiplied with the array factor

$$\text{AF} = \sum_{n=0}^{N-1} e^{np(jk_0 \sin \theta \sin \varphi - \alpha - j\beta)} \quad (4.23)$$

which contains the unit cell phase shift βp and leakage constant α as complex weighting term.

The direction of the main beam of a leaky-wave antenna depends on the phase constant of the fundamental guided wave and is given by

$$\psi = \sin^{-1} \frac{\beta}{k_0} = \sin^{-1} \frac{\beta p}{\omega p / c_0}. \quad (4.24)$$

Radiation is only possible in the fast wave region, i.e. for $|v_p|/c_0 = k_0/|\beta| > 1$ since only under this condition (4.24) yields a real valued main beam direction [23].

Application Example: Investigation of a Loaded CPW Transmission Line

The developed farfield computation method is applied to the unit cell depicted in Fig. 4.22 consisting of a coplanar waveguide (CPW) loaded with a series tank in

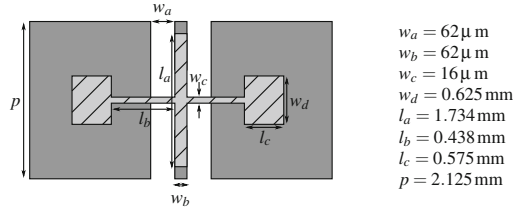


Fig. 4.22 Top view of the top- and bottom gold metallizations of the investigated unit cell

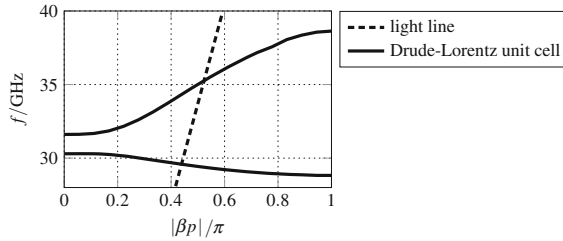


Fig. 4.23 Dispersion diagram of the investigated unit cell obtained with the fullwave eigenmode solver

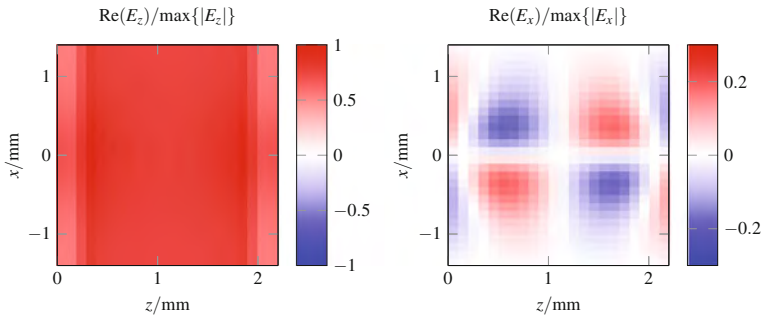


Fig. 4.24 Normalized electric nearfield distribution of a single unit cell at 30.2493 GHz

the series- and shunt branch. The dispersion diagram in Fig. 4.23 is obtained from the fullwave eigenmode computation of a single unit cell in CST Microwave Studio taking into account the propagation of all higher order modes. Due to the Drude dispersion of the effective permeability (2.23) and the Lorentz resonance of the effective permittivity (2.18), a narrow backward wave band occurs followed by a stop band and a forward wave transmission band. Radiation is possible in the fastwave region between 29.5 and 35 GHz with a frequency dependent radiation angle between -90° and $+90^\circ$ with respect to the broadside.

The obtained electric field distribution of the unit cell is shown in Fig. 4.24 for a unit cell phase shift of -30° and an eigenfrequency of 30.2493 GHz, respectively. It can be seen that the distribution of the z -component is nearly constant whereas the

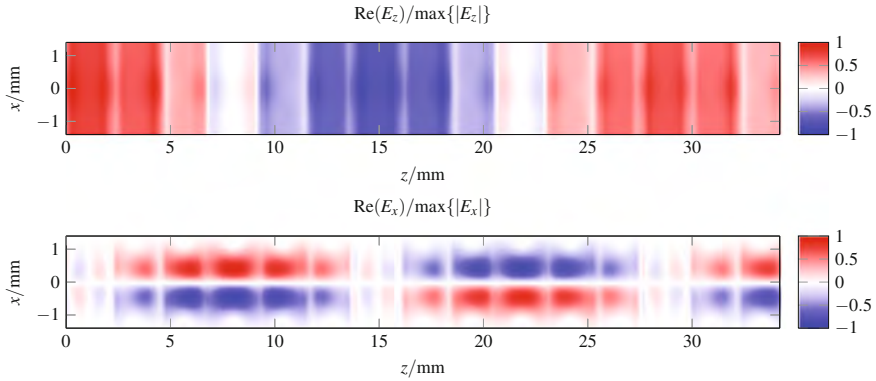


Fig. 4.25 Normalized electric nearfield distribution for backward wave propagation at 30.2493 GHz (15 unit cells, $\alpha p = 0.01$)

x -component shows a strong variation with an anti-symmetric distribution with respect to the z -axis (the propagation direction). This indicates that the main radiation in the xz -plane will exhibit mainly a φ -component while in the θ -direction no significant radiation occurs.

In Fig. 4.25, the electric field distribution of 15 unit cells after the concatenation and multiplication with the phase and leakage term is depicted. The leakage term is set to $\alpha p = 0.01$. Due to the non-zero α , a slight attenuation of the propagating wave can be observed. Furthermore, it can be seen that with $\beta p = -\pi/6$ the guided wavelength

$$\lambda_g = \frac{2\pi p}{|\beta p|} \quad (4.25)$$

confirms the theoretical value of 27 mm. As before for the unit cell, the x -component of the electric field has an opposite sign with respect to the propagation direction and this component cancels out in the farfield.

Using (4.19) and (4.20), the field distribution in Fig. 4.25 is transformed yielding the electric field strength $\tilde{\mathbf{E}}(r, \theta, \varphi)$ in the farfield region from which the directivity can be computed [22].

The obtained directivity pattern of the θ - and φ -component is shown in Fig. 4.26 for eigenfrequencies in the backward wave transmission band, at the stop band, and in the forward wave transmission band. As expected from the nearfield distribution of the electric field, the main radiation in the xz -plane is in the φ direction for all investigated frequencies because the vertical θ -components of the electric field are canceled out in the symmetry plane. Furthermore, in the backward wave band at 30.2493 GHz, the main radiation direction in the xz -plane is -22° , which corresponds to the theoretical value predicted by (4.24) for a unit cell phase shift of -30° . If the frequency is increased to the lower end of the stop band at 30.2949 GHz, the main beam points in the broadside direction due to the zero phase constant. A further

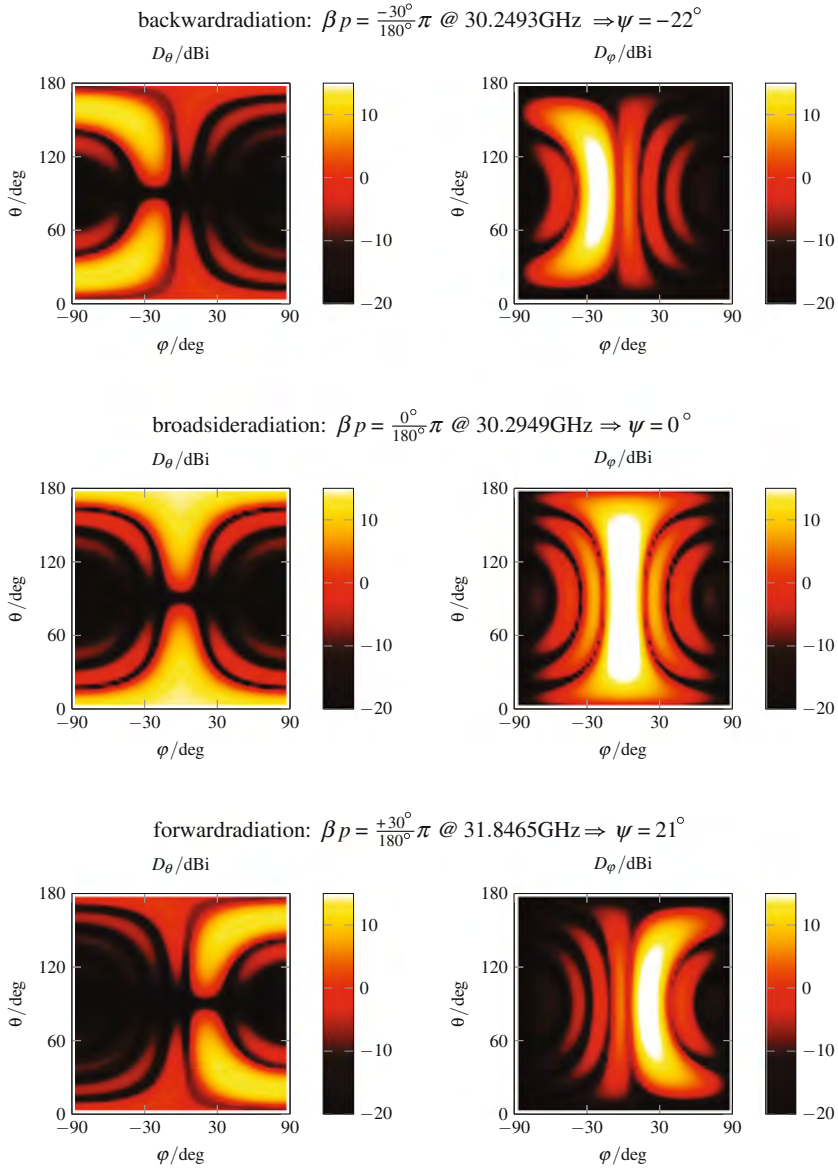
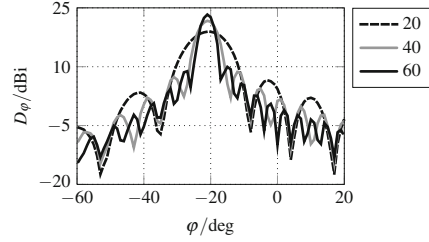


Fig. 4.26 Directivity of a leaky-wave antenna with 15 unit cells and $\alpha p = 0.01$ at different frequencies

increase of frequency above the stop band to the forward wave transmission band yields a unit cell phase shift of $+30^\circ$ resulting in a theoretical main beam direction of 20.89° which is confirmed by the directivity plot.

Fig. 4.27 Directivity in the xz -plane for different unit cell numbers



The applicability of this approach in terms of varying unit cell numbers is demonstrated for the unit cell in Fig. 4.22 in the backward wave band at 30.2493 GHz. The directivity in the xz -plane is shown in Fig. 4.27 for 20, 40, and 60 unit cells and a leakage factor of $\alpha p = 0.01$. As expected from the previous investigations, the main beam direction is $\psi = -21^\circ$. Furthermore, with a larger unit cell number, the directivity is increased while the half-power beam width is decreased. Due to the power leakage along the antenna, the ratio of the effective and the physical aperture becomes smaller and the main part of the energy is radiated along the first unit cells of the antenna while in the last elements no energy is available for radiation. Hence, above a length of 50 unit cell, an increase of the element numbers does not yield a significant performance improvement. This is confirmed by the results in Fig. 4.28 where the directivity and half-power beam width of the φ -component in the xz -plane are shown for a varying array length. A minimum half-power beam width of 3° and a maximum directivity of 25 dBi are expected for the given configuration at 30.2493 GHz.

A comparison of the farfield pattern in the xz -plane obtained using different methods is shown in Fig. 4.29. The operation frequency of the leaky-wave antenna consisting of 30 unit cells is in the backward wave band at 30.2493 GHz and the leakage is set to $\alpha p = 0.01$. In [19] the array factor (4.23) is used to approximately predict the farfield pattern of one- and two-dimensional leaky-wave antennas. This approach shows a low accuracy for scanning angles ψ and observing angles φ, θ close to the axial direction because the unit cell pattern is omitted. This is improved by the method in [20] where an assumption of the nearfield distribution of the unit cell has to be made. With a uniform field distribution and a point source, the predicted side lobe level is improved in comparison with the array factor approach. Taking the

Fig. 4.28 Directivity and half-power beam width in the xz -plane for different unit cell numbers

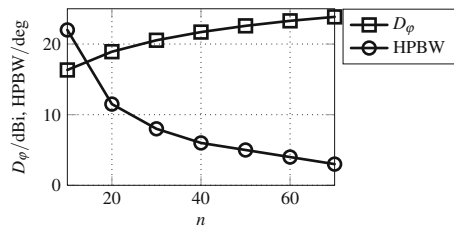
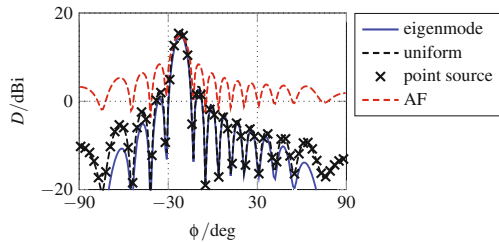


Fig. 4.29 Comparison of different farfield computation methods



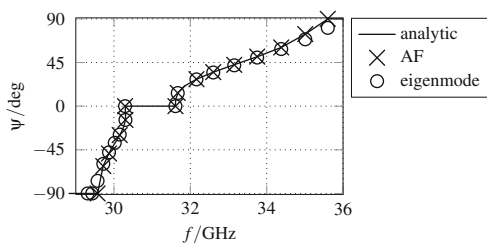
eigenmode field solution as excitation field [21], the radiation pattern close to the main beam is only marginally changed and the side lobe response close to the axial direction differs compared to the excitation with a point source or a uniform field distribution.

With (4.24) the frequency dependent radiation angle ψ in Fig. 4.30 can be calculated. The beam can be scanned in the fast wave regions of the backward- and forward wave transmission band between -90° and $+90^\circ$ whereas in the stop band and in the slow wave regions below 29 GHz and above 35.5 GHz no radiation occurs. This analytic equation fails for large scanning angles which can be seen in comparison with the eigenmode transformation method. For angles close to the axial direction, the obtained scanning angle ψ becomes smaller than predicted by the analytic and the array factor approach.

With the presented method, the farfield radiation pattern of long periodic antennas can be investigated in an efficient manner without sacrificing polarization information. The time consuming fullwave simulation of a single unit cell element has to be performed once for each phase shift of interest to obtain the eigenfrequency and the nearfield distribution. Afterwards, the response of the complete antenna can be investigated without any further fullwave simulations. For the given geometry in Fig. 4.22, the duration of the fullwave simulation of a single unit cell consisting of 205,000 hexahedral meshcells is 35 min. The concatenation, weighting, and transformation to obtain the farfield pattern of an array of 70 unit cells is performed in 17 s.

The presented transformation method is not limited to guided radiative structures. It is also possible to apply this technique to large arrays which are periodic transversal to the incident wave propagating in y -direction. In such a case, the periodic boundary condition is applied in x - and z -direction where the phase shift $\Delta\phi_x$ and $\Delta\phi_z$ between

Fig. 4.30 Extracted radiation angle using the analytic solution (4.24), the array factor method, and the eigenmode method



each unit cell boundary yields the angle of the transmitted wave. Then (4.19) and (4.20) can be used to determine the pattern of the transmitted wave in the farfield region.

References

1. A.M. Nicolson, G.F. Ross, Measurement of the intrinsic properties of materials by time-domain techniques. *IEEE Trans. Instrum. Meas.* **19**(4), 377–382 (1970)
2. W. Weir, Automatic measurement of complex dielectric constant and permeability at microwave frequencies. *Proc. IEEE* **62**(1), 33–36 (1974)
3. D. Frickey, Conversions between s , z , y , h , $abcd$, and t parameters which are valid for complex source and load impedances. *IEEE Trans. Microw. Theory Tech.* **42**, 205–211 (1994)
4. V.V. Varadan, R. Ro, Unique retrieval of complex permittivity and permeability of dispersive materials from reflection and transmitted fields by enforcing causality. *IEEE Trans. Microw. Theory Tech.* **55**, 2224–2230 (2007)
5. Z. Szabo, G.-H. Park, R. Hedge, E.-P. Li, A unique extraction of metamaterial parameters based on kramers-kronig relationship. *IEEE Trans. Microw. Theory Tech.* **58**(10), 2646–2653 (2010)
6. R. Collin, I. Antennas, P. Society, *Field Theory of Guided Waves*, The IEEE/OUP Series on Electromagnetic Wave Theory (Formerly IEEE Only), Series Editor Series (IEEE Press, New York, 1991)
7. B. Bandlow, R. Schuhmann, G. Lubkowski, T. Weiland, Analysis of single-cell modeling of periodic metamaterial structures. *IEEE Trans. Magn.* **44**(6), 1662–1665 (2008)
8. R. Schuhmann, B. Bandlow, G. Lubkowski, T. Weiland, Micro- and macroscopic simulation of periodic metamaterials. *Adv. Radio Sci.* **6**, 77–82 (2008)
9. G. Lubkowski, B. Bandlow, R. Schuhmann, T. Weiland, Effective modeling of double negative metamaterial macrostructures. *IEEE Trans. Microw. Theory Tech.* **57**(5), 1136–1146 (2009)
10. J. Pendry, A. Holden, D. Robbins, W. Stewart, Magnetism from conductors and enhanced nonlinear phenomena. *IEEE Trans. Microw. Theory Tech.* **47**, 2075–2084 (1999)
11. D.R. Smith, J.B. Pendry, Homogenization of metamaterials by field averaging (invited paper). *J. Opt. Soc. Am. B* **23**, 391–403 (2006)
12. C. Simovski, Material parameters of metamaterials (a review). *Opt. Spectrosc.* **107**(5), 726–753 (2009)
13. C.R. Simovski, On electromagnetic characterization and homogenization of nanostructured metamaterials. *J. Opt.* **13**(1), 013001 (2011)
14. O. Acher, A. Adenot, F. Duverger, Fresnel coefficients at an interface with a lamellar composite material. *Phys. Rev. B* **62**(20), 13748 (2000)
15. J.-M. Lerat, N. Malléjac, O. Acher, Determination of the effective parameters of a metamaterial by field summation method. *J. Appl. Phys.* **100**(8), 084908 (2006)
16. S. Boscolo, C. Conti, M. Midrio, C. Someda, Numerical analysis of propagation and impedance matching in 2d photonic crystal waveguides with finite length. *J. Light. Technol.* **20**, 304–310 (2002)
17. R. Biswas, Z.Y. Li, K.M. Ho, Impedance of photonic crystals and photonic crystal waveguides. *Appl. Phys. Lett.* **84**(8), 1254–1256 (2004)
18. G. Lubkowski, Simulation of Electromagnetic Fields in Double Negative Metamaterials. Ph.D. thesis, Technische Universität Darmstadt, 2009
19. C. Caloz, T. Itoh, Array factor approach of leaky-wave antennas and application to 1-d/2-d composite right/left-handed (crlh) structures. *IEEE Microw. Wirel. Compon. Lett.* **14**, 274–276 (2004)
20. Z. Li, J. Wang, F. Li, Prediction of radiation patterns of the crlh leaky-wave antennas by different approaches, in *IEEE International Conference on Microwave Technology Computational Electromagnetics (ICMTCE)* (2011)

21. M. Maasch, M. Roig, C. Damm, R. Jakoby, Efficient farfield computation from eigenmode simulations for leaky-wave antennas, in *2013 IEEE Antennas and Propagation Society International Symposium (APSURSI)*, pp. 1656–1657, July 2013
22. C.A. Balanis, *Antenna Theory: Analysis and Design*, 2nd edn. (Wiley-Interscience, Hoboken, 2005)
23. D. Jackson, C. Caloz, T. Itoh, Leaky-wave antennas. *Proc. IEEE* **100**, 2194–2206 (2012)

Chapter 5

Tunable Transmission Line Metamaterials

Transmission line metamaterials using the possibility of forward- and backward wave propagation or the independent design of the phase and impedance [1–5], have a broad range of potential applications. Such artificial transmission lines can be designed with a large positive or negative phase shift making it possible to realize compact filters [6], phase shifters [7, 8], and couplers [3, 9]. Leaky-wave antennas with a frequency tunable radiation covering 180° including the broadside direction in its fundamental spatial harmonic have been demonstrated [10–12]. In [13] the zeroth-order resonance is exploited to design a compact transmission line resonator. For applications such as microstrip antennas [14] or delay lines for passive RFID devices [15], the low phase- and group velocity can be exploited to design very compact components.

By employing transmission line metamaterials with lumped elements based on the theoretical considerations in Chap. 2 it is possible to tailor the electric and magnetic response independently of each other for a desired application. Hence, within the physical limitations like causality and passivity, arbitrary dispersion characteristics can be designed. Furthermore, with tunable elements, components with reconfigurable properties can be realized, such as voltage tunable filters, leaky-wave antennas or transmission line matching networks. Similarly, it is possible to use sensing elements, e.g. temperature dependent capacitors, for sensor applications.

In this chapter, transmission line metamaterials with tunable dispersion properties are presented using different unit cell configurations and voltage tunable elements, such as semiconductor varactors and liquid crystal. Apart from dispersion characteristics, technological constraints and realizability, especially for voltage tunable designs that require a biasing network, are aspects that are taken into account yielding artificial transmission lines with tunable properties and low parasitic effects.

5.1 Tunable Double Series Transmission Line

In [16, 17], the double series (DS) and double parallel (DP) unit cells have been investigated and compared to the CRLH and D-CRLH [18] unit cell concerning their dispersion properties. In the double series configuration, the capacitors can be replaced by varactors so that with a simple biasing network a tunable transmission line can be implemented and the phase and impedance can be tuned for the application in transmission line components.

Figure 5.1a shows the modified DS unit cell with ideal distributed elements, i.e. without spatial dispersion. It consists of a series resonator in the series and shunt branch. Compared to [17] the shunt capacitance C'_0 representing the dielectric response of the host medium is added to the unit cell circuit to provide a causal response with the purely real effective material parameters shown in Fig. 5.1b. The effective permittivity shows a Lorentz dispersion (2.17) with a negative value between the electric resonance

$$\omega_{0\varepsilon} = \frac{1}{\sqrt{L'_{\text{sh}} C'_{\text{sh}}}} \quad (5.1)$$

and the electric transition frequency

$$\omega_{\text{te}} = \sqrt{\frac{1}{L'_{\text{sh}} C'_{\text{sh}}} + \frac{1}{L'_{\text{sh}} C'_0}} \quad (5.2)$$

while the effective permeability follows the Drude dispersion (2.24) with a negative effective permeability below the magnetic plasma frequency

$$\omega_{\text{p}\mu} = \frac{1}{\sqrt{L'_{\text{se}} C'_{\text{se}}}}. \quad (5.3)$$

For a narrow frequency band close to the electric resonance frequency and far from the electric transition frequency, C'_0 can be neglected which is done from this point on.

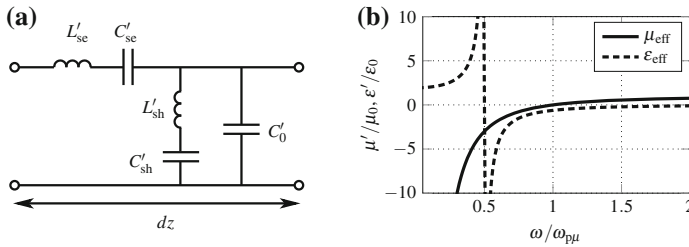


Fig. 5.1 Double series transmission line: **a** Modified unit cell configuration with the host material capacitance C'_0 , **b** Effective material parameters for the lossless case with $\omega_{0\varepsilon} = 0.5\omega_{\text{p}\mu}$

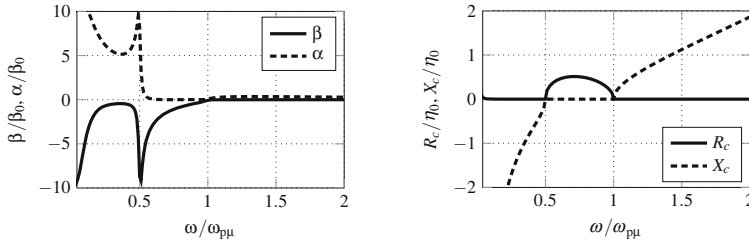


Fig. 5.2 Normalized propagation constant and line impedance of an ideal lossless double series transmission line with $\omega_{0\varepsilon} = 0.5\omega_{p\mu}$

The electric transition frequency is shifted to high frequencies out of the frequency band of interest so that the propagation constant can be approximated by

$$\gamma = \alpha + j\beta \approx \pm \sqrt{\frac{L'_{se}}{L'_{sh}} \cdot \frac{\omega^2 - \omega_{p\mu}^2}{\omega^2 - \omega_{0\varepsilon}^2}} \quad (5.4)$$

and the line impedance by

$$Z_c = R_c + jX_c \approx \pm \frac{j}{\omega} \sqrt{L'_{se} L'_{sh} (\omega^2 - \omega_{p\mu}^2)(\omega^2 - \omega_{0\varepsilon}^2)}. \quad (5.5)$$

The frequency response of the propagation constant and the line impedance are shown in Fig. 5.2. Between $\omega_{0\varepsilon}$ and $\omega_{p\mu}$, both μ'_{eff} and $\varepsilon'_{\text{eff}}$ are negative resulting in a backward wave band with $\beta < 0$. At $\omega_{p\mu}$ the effective permeability becomes positive yielding a stop band for higher frequencies. For frequencies below $\omega_{0\varepsilon}$, the effective permittivity becomes positive while the effective permeability is negative resulting in a stop band that delimits the lower cutoff frequency of the transmission band.

In the propagation constant (5.4), a zero and a pole exist at $\omega_{p\mu}$ and $\omega_{0\varepsilon}$, respectively. Since the slope

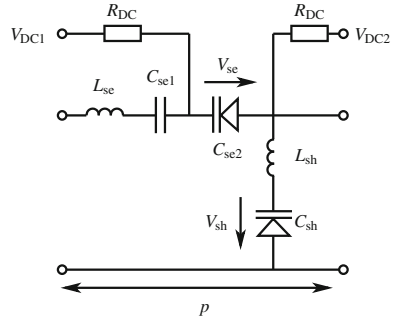
$$\left. \frac{\partial \beta}{\partial \omega} \right|_{\alpha=0} = \frac{1}{v_g} \quad (5.6)$$

has to be positive for the case of low losses, the frequency order of $\omega_{p\mu}$ and $\omega_{0\varepsilon}$ sets the sign of the square root in (5.4) so that

$$\begin{aligned} \text{(i)} \quad & \omega_{p\mu} < \omega_{0\varepsilon} \Rightarrow \beta > 0, \alpha = 0, \\ \text{(ii)} \quad & \omega_{p\mu} > \omega_{0\varepsilon} \Rightarrow \beta < 0, \alpha = 0, \\ \text{(iii)} \quad & \omega_{p\mu} = \omega_{0\varepsilon} \Rightarrow \beta = 0, \alpha > 0. \end{aligned} \quad (5.7)$$

For the case $\omega_{p\mu} = \omega_{0\varepsilon}$, the zero and pole of γ as well as its frequency dependency cancel out so that γ becomes constant and purely real for all frequencies. By separately tuning the zero and pole of γ , the dispersion can be tuned to create either a

Fig. 5.3 Double series unit cell with separately tunable series- and shunt branch including the resistive biasing network



backward or forward wave propagation band with $\beta \neq 0$ and $\alpha = 0$ or to a stopband configuration with $\beta = 0$ and $\alpha > 0$.

Implementation of the Tunable Unit Cell

To independently tune the magnetic and electric response, tunable elements have to be added to the unit cell. Since voltage tuning is practical and desirable for a number of applications, the distribution of a tuning voltage and the realization of the necessary biasing network are important issues in the design process. A double series unit cell configuration with varactor diodes as tunable elements is shown in Fig. 5.3 including the necessary DC blocking capacitor C_{se1} and a resistive biasing network represented by R_{DC} . This configuration is chosen in such a way that the implementation of the tunability is possible with a minimum number of additional elements. Furthermore, only two tuning voltages V_{DC1} and V_{DC2} are necessary yielding the varactor voltages

$$V_{se} = V_{DC1} - V_{DC2}, \quad (5.8)$$

$$V_{sh} = V_{DC2}. \quad (5.9)$$

To demonstrate the proposed tuning of the DS unit cell with a forward- and backward wave propagation, a prototype is designed, fabricated, and measured for a frequency of 2.5 GHz. For such frequencies, a number of semiconductor varactors are available. Here, the varactor diode Infineon BB857 is used due to its low resistivity and high self resonance. Measurements of the varactor on Rogers RO5880 substrate at 2.5 GHz yield a series inductance of 1.5 nH, and a series resistance of 2.6 Ω . All simulations of the unit cell and the artificial transmission line are carried out using the circuit simulator of AWR Microwave Studio. Measured scattering parameters of all lumped elements are used in the simulation while microstrip sections, connection pads, and vias are represented by models based on fullwave simulations.

The layout of the DS line in microstrip technology is shown in Fig. 5.4a. The center line contains the varactor diodes with C_{se2} and the DC blocking capacitors C_{se1} . The series inductance L_{se} is determined by the inductance of the varactor diodes and the series inductance of the microstrip host line. The shunt branch is implemented by the varactor diode with C_{sh} which is connected to the ground layer using a via. Like

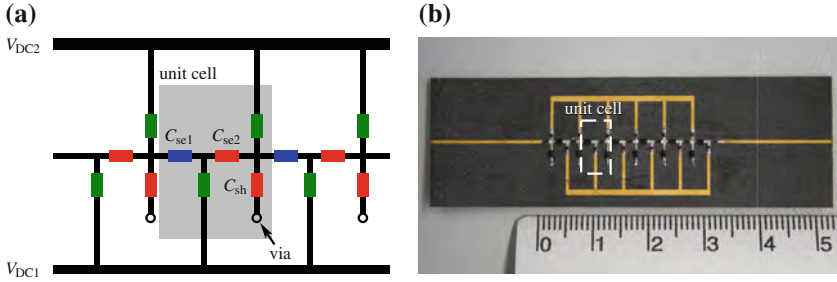


Fig. 5.4 Voltage tunable double series transmission line: **a** layout of the tunable DS line, *red*: varactors C_{se2} , C_{sh} , *blue*: DC blocking capacitors C_{se1} , *green*: biasing resistors R_{DC} , **b** photo of the manufactured prototype with 6 unit cells

in the series branch, the inductance L_{sh} is determined by the varactor inductance and the connection line to signal and ground. To reduce the coupling between the shunt branches in adjacent unit cells, their orientation is altered in each unit cell.

As substrate Rogers RO5880 with a thickness of 0.787 mm is used. The complete prototype in Fig. 5.4b consists of 6 unit cells with a total length of 33 mm. A 20 mm microstrip section at the input and output port is used for connecting a microstrip test fixture for characterization.

To set the DS unit cell to forward or backward wave propagation, the condition

$$\frac{L_{se}}{1/C_{se1} + 1/C_{se2}} = 1/\omega_{p\mu}^2 = L_{sh}C_{sh} = 1/\omega_{0\varepsilon}^2 = 1/\omega_{\text{balanced}}^2 \quad (5.10)$$

has to be fulfilled for the medium capacitor value of the varactors so that $\omega_{p\mu}$ and $\omega_{0\varepsilon}$ can be shifted into opposite direction to create either a positive or negative sign for the phase constant β , depending on the cases (5.7). The lumped element values of the unit cell are $L_{se} = 2.8$ nH, $C_{se} = 0.49 \dots 4.9$ pF, $L_{sh} = 3.1$ nH, $C_{sh} = 0.5 \dots 6.5$ pF. With these values, a theoretical tuning of the magnetic plasma frequency between 1.36 and 4.3 GHz and a tuning of the electric resonance frequency between 1.12 and 4.0 GHz is possible.

The simulated unit cell phase shift in Fig. 5.5 shows how for different tuning voltages the cutoff frequencies of the transmission band can be independently tuned and the sign of the phase constant can be changed. With a constant series voltage $V_{se} = 0$ V and an increasing shunt voltage V_{sh} , the lower cutoff frequency of the forward wave transmission band is fixed at 1 GHz while the upper cutoff frequency is shifted from 2.2 to 3.5 GHz. For the backward wave transmission, the series voltage $V_{se} = 25$ V yields a constant upper cutoff frequency of 3.7 GHz and a decreasing voltage V_{sh} shifts the lower cutoff frequency of the backward wave band from 3.2 to 1.7 GHz. The unsymmetrical tuning of the cutoff frequencies is due to the series connection of the non-tunable C_{se1} and the tunable C_{se2} which leads to different minimum and maximum values of the total series- and shunt capacitance.

For the investigation of the Bloch impedance, as before for the phase investigation, one cutoff frequency of the transmission band is fixed while the second cutoff

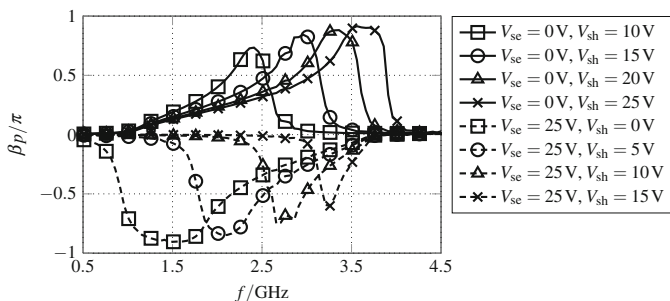
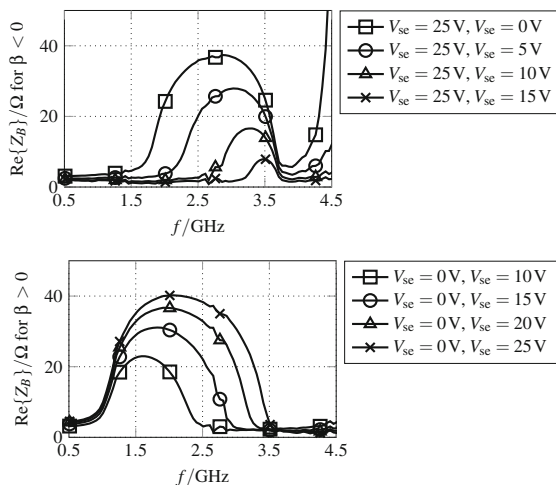


Fig. 5.5 Simulated unit cell phase shift for different tuning states for forward- and backward wave operation (measured scattering parameters are used for all lumped components)

Fig. 5.6 Simulated realpart of the Bloch impedance for different tuning states for forward- and backward wave operation (measured scattering parameters are used for all lumped components)



frequency is tuned. The real part of the simulated Bloch impedance for a forward- and backward wave transmission is shown in Fig. 5.6. As for the phase shift, the independent tuning of the cutoff frequencies can be clearly observed. At 2.5 GHz the real part of the Bloch impedance can be tuned between 2 and 40 Ω . The covered impedance range can be optimized for a specific application by adapting the inductance values in the series and shunt branch with lumped inductors.

Figure 5.7 shows a photo of the measurement setup. A microstrip test fixture is used to contact the double series transmission line while the DC tuning voltages are applied directly to the biasing lines.

A comparison of the simulated and measured unit cell phase shift is shown in Fig. 5.8 for the minimum and maximum tuning voltages of each varactor. Due to the use of measured scattering parameters of the lumped elements, the agreement is good in the transmission band. At 3 GHz a symmetric, continuous tuning of the unit cell phase shift is possible between at least -0.3π and $+0.3\pi$.

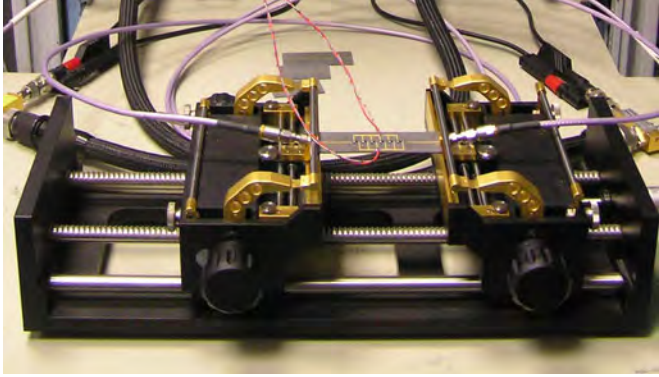


Fig. 5.7 Microstrip characterization setup for the measurement of the tunable double series line

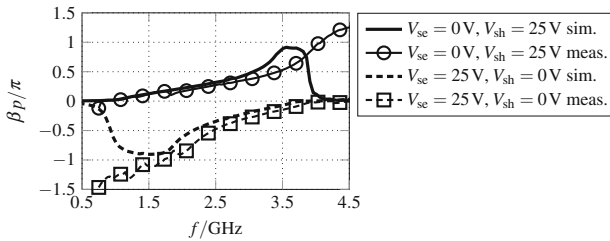
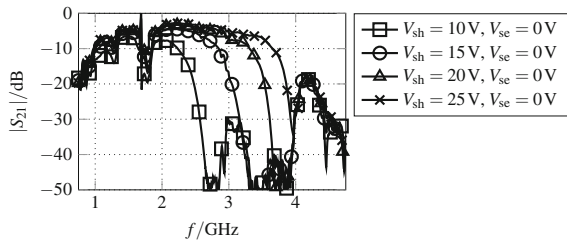


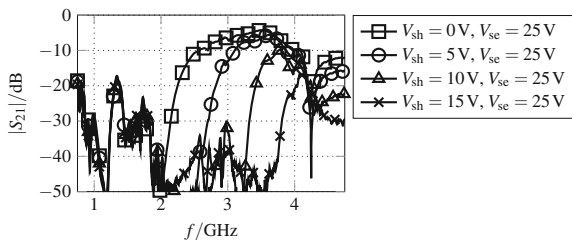
Fig. 5.8 Comparison of simulated and measured unit cell phase shift for different tuning states

Fig. 5.9 Measured transmission for forward wave propagation with $V_{sh} = 10 \dots 25 \text{ V}$, $V_{se} = 0 \text{ V}$



Figures 5.9 and 5.10 show the measured forward transmission for different tuning states and for the forward and backward wave operation, respectively. For $V_{sh} > V_{se}$ (Fig. 5.9) β becomes positive, i.e. a forward wave transmission band occurs. As V_{sh} is increased with $V_{se} = 0 \text{ V}$ kept constant, the upper transmission band limit is shifted to higher frequencies while the lower band limit is constant at 1 GHz. For $V_{sh} < V_{se}$ (Fig. 5.10) β becomes negative and the transmission band has a backward wave characteristic. A decreasing voltage V_{sh} and a constant voltage $V_{se} = 25 \text{ V}$ keeps the upper band limit constant at 4.2 GHz and shifts the lower transmission band limit to lower frequencies.

Fig. 5.10 Measured transmission for backward wave propagation with $V_{\text{sh}} = 0 \dots 15 \text{ V}$, $V_{\text{se}} = 25 \text{ V}$



5.2 Liquid Crystals for Voltage Tunable Components

For the double series transmission line in the previous section, semiconductor varactors have been used to introduce a continuous voltage tuning of the dispersion characteristics. Such varactor diodes limit the operation frequency to about 10 GHz. To overcome this frequency limitation, liquid crystals (LC) are applied in this work to realize planar and three-dimensional metamaterial structures with tunable properties.

Due to their continuous tunability and low loss at frequencies above 10 GHz, liquid crystals have been applied in numerous voltage tunable components for frequencies up to the mm-wave region, such as voltage tunable phase shifters [19], reflectarrays [20, 21], and frequency selective surfaces [22]. Furthermore, several planar and three-dimensional metamaterials at frequencies up to 30 GHz using LC, such as magnetically tunable omega resonators [23], voltage tunable, metamaterial based frequency selective surfaces [24], or tunable leaky-wave antennas [25, 26], have been presented.

Figure 5.11 shows the orientation of rod-like LC molecules for different phases, i.e. different temperatures. The orientational order parameter [27, 28]

$$|S| = \left\langle \frac{3}{2} \cos^2 \theta - \frac{1}{2} \right\rangle \quad (5.11)$$

describes the (temporal or spatial) average of the angle θ between each rod-like molecule and the average direction of all molecules (the director \mathbf{n}). At low temperatures, the molecules align in a crystalline order where their position is fixed. All molecules

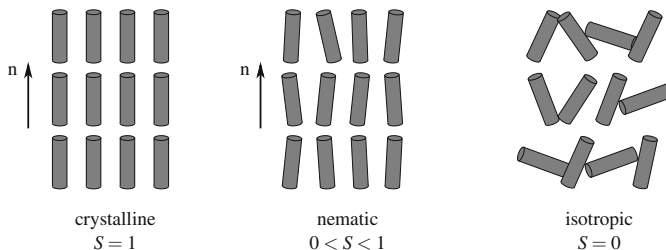


Fig. 5.11 Different LC phases and their orientational order parameter

are oriented in the same direction yielding a maximum order of $S \approx 1$. By increasing the temperature, the LC transforms into the nematic phase, a mesophase between the crystalline and isotropic phase. Due to the strong intermolecular interaction, an orientation of the molecules with the director \mathbf{n} can be observed, but with lower orientational order S . In the isotropic phase at a higher temperature, the order becomes zero and a main orientation does not exist because the molecules can orient freely without constraints and the bulk material shows an isotropic response.

LC is primarily used in the nematic phase since here, the molecules exhibit an order $S > 0$ and a tunable main direction. Due to the rod-like structure and the rotational symmetry, the bulk material exhibits a uniaxial anisotropy which can be represented by the permittivity tensor

$$\bar{\epsilon}_{\text{LC}} = \epsilon_0 \mathbf{R} \begin{pmatrix} \epsilon_{r,\text{LC}\parallel} & 0 & 0 \\ 0 & \epsilon_{r,\text{LC}\perp} & 0 \\ 0 & 0 & \epsilon_{r,\text{LC}\perp} \end{pmatrix} \mathbf{R}^{-1}. \quad (5.12)$$

The rotation matrix \mathbf{R} describes the rotation of the director \mathbf{n} with respect to the electric RF field. Hence, each component of the electric RF field \mathbf{E}_{RF} experiences a permittivity between $\epsilon_{r,\text{LC}\perp}$ and $\epsilon_{r,\text{LC}\parallel}$ depending on the orientation of the director \mathbf{n} with respect to the electric RF field.

Tuning of the director \mathbf{n} of nematic LC can be achieved by different approaches [28, 29]:

- *Magnetically*: Molecules align parallel to static magnetic field lines.
- *Electrically*: Molecules align parallel to static or low frequency electric field lines.
- *Mechanically with an alignment layer*: A layer of polyimide is processed on a surface. This layer with a thickness of a few nanometers is mechanically rubbed with a velvet cloth which creates grooves in the alignment layer. Molecules close to the surface are anchored in parallel to these grooves and the rubbing direction.

In practical applications, a combination of mechanical and electrical alignment is used where the force on the molecules is the superposition of the force from the alignment layer and the electric field. The equilibrium between these forces and the resulting orientation between the molecules and the electric RF field can be tuned and hence, the average bulk permittivity $\langle \epsilon_{r,\text{LC}} \rangle$ experienced by the electric RF field can be tuned between the perpendicular and parallel component.

The tuning of the director field is depicted in Fig. 5.12 for different DC tuning voltages of a parallel plate capacitor including an alignment layer on the electrodes. These electrodes are used to simultaneously apply the DC tuning voltage and the electric RF field. With the surface area A of the electrodes and the distance d between them, the capacitance becomes

$$C = \epsilon_0 \langle \epsilon_{r,\text{LC}} \rangle \frac{A}{d}. \quad (5.13)$$

Here, $\langle \epsilon_{r,\text{LC}} \rangle$ represents the average permittivity of the entire LC layer between the electrodes.

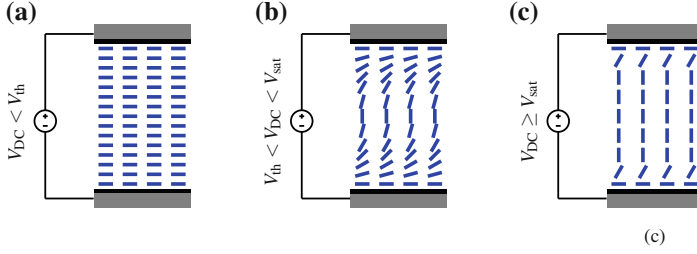
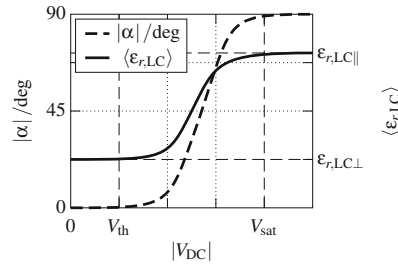


Fig. 5.12 Director orientation in a varactor with alignment layer for different DC tuning voltages V_{DC} : **a** without a DC voltage, **b** below the saturation voltage, **c** above the saturation voltage

The alignment layer anchors the molecules close to the surface and forces them to orient parallel to the surface. Without a tuning voltage, due to the molecule interaction, molecules further from the surface follow this orientation (Fig. 5.12a) and the average permittivity is $\langle \epsilon_{r,LC} \rangle = \epsilon_{r,LC\perp}$. If the DC voltage is increased above the threshold voltage V_{th} , molecules experience two orientation forces: the mechanical force from the alignment layer and the force from the electric field. In the equilibrium, molecules close to the alignment layer align parallel to the surface while elements in the center between the electrodes orient parallel to the electric field (Fig. 5.12b). The average permittivity is $\epsilon_{r,LC\perp} < \langle \epsilon_{r,LC} \rangle < \epsilon_{r,LC\parallel}$. If the voltage is further increased above the saturation voltage V_{sat} , the electric force on all molecules becomes larger than the mechanical force and all molecules, except the ones close to the alignment layer, are aligned parallel to the electric field (Fig. 5.12c) so that the average permittivity becomes $\langle \epsilon_{r,LC} \rangle \approx \epsilon_{r,LC\parallel}$.

The general voltage dependence of the director orientation α and the average LC permittivity is shown in Fig. 5.13. For small voltages, the force by the alignment layer is larger than the electric force from the applied tuning voltage. If the tuning voltage is increased above the threshold V_{th} , the main orientation is caused by the electric force. Above the saturation voltage V_{sat} , all molecules are aligned parallel to the applied electric field and the average permittivity reaches its maximum. Detailed descriptions of methods to calculate the director orientation can be found in [30–32].

Fig. 5.13 General voltage dependence of the average LC bulk permittivity



The LC used in this work is the commercial mixture GT3-23001 by Merck KGaA. At room temperature and at a frequency of 30 GHz its dielectric parameters are $\epsilon_{r,LC\perp} = 2.47$, $\epsilon_{r,LC\parallel} = 3.16$, $\tan \delta_{LC\perp} = 0.0151$, $\tan \delta_{LC\parallel} = 0.0033$. Investigations of this LC mixture have shown a significant anisotropy $\Delta\epsilon_{r,LC}$ up to a frequency of at least 4 THz [33, 34]. Comprehensive information about the manufacturing process of different microwave components using LC can be found in [20, 35–37].

5.3 Tunable Artificial Transmission Line Using Liquid Crystal

The following tunable transmission line with separately tunable series and shunt branch, based on liquid crystal material, is designed for an operation frequency of 30 GHz. Alignment of the LC molecules, i.e. tuning, is realized electrically and magnetically to investigate the influence of the resistive biasing network on the RF response.

The basic unit cell with LC varactors is shown in Fig. 5.14 which is a symmetric configuration of the previously presented double series unit cell including the parasitic shunt capacitance C_0 and losses represented by the resistors R_{se} and R_{sh} . Here, the impact of C_0 and hence, the electric plasma frequency, is not neglected.

Figure 5.15 demonstrates how a resistive biasing network can be incorporated in the unit cell. For a small varactor leakage current, the voltage drop over the resistive biasing network can be neglected and the varactor voltages are

Fig. 5.14 RF equivalent circuit of the unit cell with tunable series and shunt branch

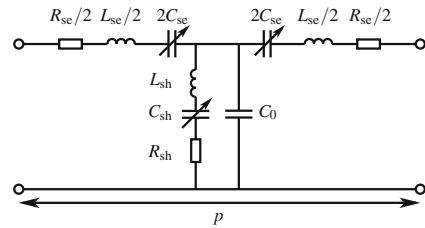
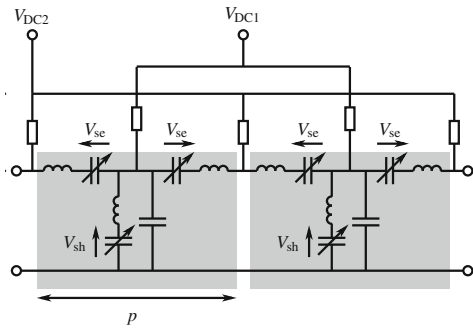


Fig. 5.15 Schematic of two unit cells marked by the gray shading and the additional bias network with the resulting DC tuning voltages



$$V_{se} = V_{DC1} - V_{DC2}, \quad (5.14)$$

$$V_{sh} = -V_{DC1}. \quad (5.15)$$

As for the prototype with semiconductor varactors, only two tuning voltages are necessary to independently tune the capacitors in the series- and shunt branch.

If the unit cell length p is small compared to the wavelength, i.e. if the spatial dispersion is negligible, the unit cell shows a Drude dispersion for the effective permeability and Lorentz dispersion for the effective permittivity so that (2.18) and (2.23) become

$$\mu_{eff} = \frac{L_{se}}{p} \left(1 - \frac{\omega_{p\mu}^2 + jR_{se}/L_{se}}{\omega^2} \right), \quad (5.16)$$

$$\varepsilon_{eff} = \frac{C_0}{p} \left(1 + \frac{\omega_{te}^2 - \omega_{0e}^2}{\omega^2 - \omega_{0e}^2 - j\omega R_{sh}/L_{sh}} \right). \quad (5.17)$$

With the varactors C_{se} and C_{sh} , the magnetic plasma and electric transition frequencies are

$$\omega_{p\mu}^2(V_{se}) = \frac{1}{L_{se}C_{se}(V_{se})}, \quad (5.18)$$

$$\omega_{te}^2(V_{sh}) = \frac{1}{L_{sh}C_{sh}(V_{sh})} + \frac{1}{L_{sh}C_0} \quad (5.19)$$

and the electric resonance frequency is

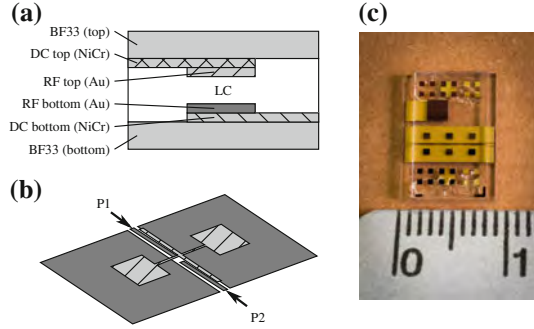
$$\omega_{0e}^2(V_{sh}) = \frac{1}{L_{sh}C_{sh}(V_{sh})}, \quad (5.20)$$

which can be shifted by the DC voltages V_{se} in the series branch and V_{sh} in the shunt branch. Hence, at a fixed frequency the effective permeability and permittivity can be tuned independently. For $\omega_{p\mu} > \omega_{te}$, the dispersion can be divided into four different frequency bands: a forward wave transmission band with a positive phase shift above the magnetic plasma frequency and the electric transition frequency, a backward wave transmission band between the electric resonance and transition frequency and two stop bands, the first one below the electric resonance frequency and a second one between the electric transition frequency and the magnetic plasma frequency.

The unit cell in Fig. 5.16 is implemented as a loaded coplanar waveguide section consisting of two metallic layers separated by a layer of LC. By applying a variable static or low frequency electric field between the two metallic layers, the orientation of the LC molecules can be changed continuously yielding the voltage tunable capacitors C_{se} and C_{sh} between the metal layers.

The fabrication process follows the steps in Appendix A.3 and is based on [35]. A schematic view of the loaded CPW unit cell and a photo of the manufactured

Fig. 5.16 **a** Cross section view of the substrate and metal layers, **b** layout of the unit cell with *top*- and *bottom* RF metallization, **c** photo of the manufactured prototype

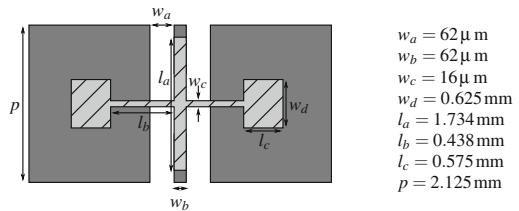


prototype consisting of three unit cells are shown in Fig. 5.16. The RF signal alternates between the bottom-gold and top-gold metallization, each having a thickness of $2\text{ }\mu\text{m}$. This results in the series resonator consisting of C_{se} and L_{se} . The resonator in the shunt branch is formed by the shunt wire and the metal patch, which yields the shunt capacitor C_{sh} . For the top and bottom substrates, $700\text{ }\mu\text{m}$ thick glass substrate Schott BF33 ($\epsilon_r = 4.65$, $\tan \delta = 0.006$) is used. They are separated by micropearls from Sekisui Chemical with a diameter of $100\text{ }\mu\text{m}$, which define the height of the LC cavity between the top and bottom metallization. A high resistive nickel-chromium (NiCr) layer with a conductivity of $5 \times 10^5\text{ S/m}$ and a thickness of 20 nm is used as an adhesive layer between the gold metallization and glass substrate. Additionally, this NiCr layer is used to pattern the bias lines with a width of $20\text{ }\mu\text{m}$ yielding a per unit length resistance of $R'_{bias} = 5\text{ M}\Omega/\text{m}$. A thin layer of rubbed polyimide on the glass substrates orients the LC molecules parallel to the propagation direction when no bias field is applied. Due to its small thickness of a few nm this polyimide layer does not influence the RF response of the unit cell.

In simulations carried out in Agilent ADS, both plasma frequencies are not tuned independent of each other since the anisotropy and local tuning of the LC layer cannot be modeled. Instead, an isotropic and homogenous dielectric layer with a varying permittivity is assumed for the LC layer (Fig. 5.17).

The simulated real part of the effective material parameters without bias lines is shown in Fig. 5.18 for the biased and unbiased state, i.e. for an LC permittivity of $\epsilon_{r,LC\parallel} = 3.16$ and $\epsilon_{r,LC\perp} = 2.47$, respectively. The magnetic plasma frequency is shifted from 27 to 31 GHz if the orientation of the LC is changed. The electric

Fig. 5.17 Top view of the *top* and *bottom* gold metallizations and dimensions



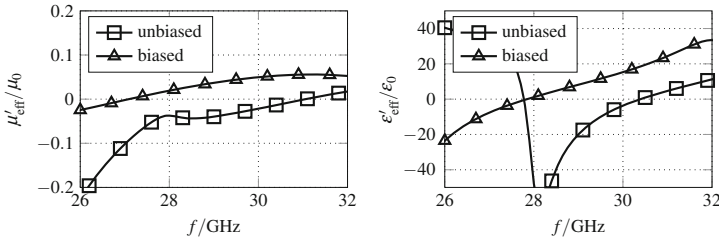


Fig. 5.18 Simulated real part of effective material parameters of the tunable transmission line for two LC orientations

Fig. 5.19 On-wafer measurement setup for the tunable transmission line. One tuning voltage is applied via bias-tees and the RF probes, the second via a DC probe on a contact pad of the substrate



transition frequency shifts from 27.8 to 30.4 GHz. According to (5.19), the expected tuning range of the effective permittivity is smaller than for the permeability due to the additional non-tunable term introduced by the host medium capacitor in the shunt branch (Fig. 5.15).

Measurements of the scattering parameters with an on-wafer setup as depicted in Fig. 5.19 are carried out for magnetic and electric alignment of the LC molecules. In the case of magnetic alignment, all molecules in the LC layer are oriented parallel (unbiased) or perpendicular (biased) to the metallization and substrate surface. The latter is done by placing rare earth magnets with a field strength of 1.3 T directly below the bottom glass substrate. Furthermore, no resistive bias lines are present in the magnetically tunable prototype. The extracted effective material parameters are presented in Fig. 5.20. The magnetic plasma frequency is shifted from 35.7 to 34.5 GHz and the electric transition frequency from 35.4 to 34 GHz when the static magnetic field is applied in vertical direction. Due to manufacturing tolerances, the response of the effective permeability and permittivity are shifted to higher frequencies. The tuning range is smaller than predicted by simulations since, due to the anchoring force, the LC near the substrate surface cannot be aligned perfectly perpendicular to the alignment layer.

In addition to magnetic alignment, electric tuning and the impact of the manufactured resistive biasing lines is investigated. While keeping one voltage constant

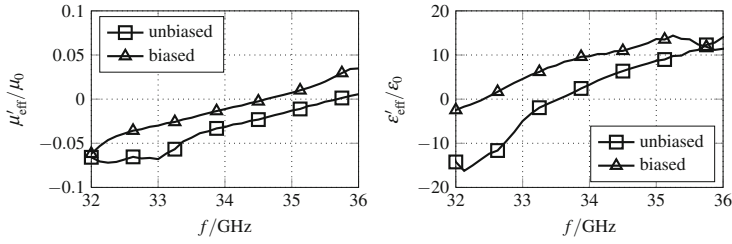


Fig. 5.20 Measured real part of effective material parameters for magnetic biasing for two different orientation of the magnetic flux

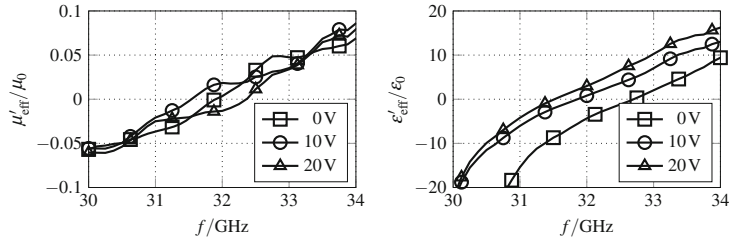


Fig. 5.21 Measured real part of effective material parameters for tuned shunt capacitor with varying V_{sh} and constant $V_{\text{se}} = 10$ V

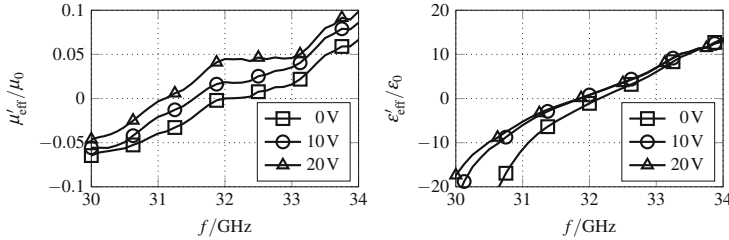


Fig. 5.22 Measured real part of effective material parameters for tuned series capacitor with varying V_{se} and constant $V_{\text{sh}} = 10$ V

and varying the other voltage, only the effective permeability or permittivity is tuned which is confirmed by the measurement results in Figs. 5.21 and 5.22. The resistive bias network shifts the response by -2 GHz compared to the magnetic alignment without any bias lines.

The measurement results in Fig. 5.21 are obtained for a constant voltage $V_{\text{se}} = 10$ V in the series branch and a varying voltage V_{sh} between 0 and 20 V in the shunt branch. As expected, the magnetic plasma frequency is not tuned and is constant around 32 GHz. With an increasing voltage V_{sh} the electric transition frequency shifts from 32.7 to 31.5 GHz.

For the results in Fig. 5.22, the voltage in the shunt branch is kept constant at $V_{\text{sh}} = 10$ V while the voltage in the series branch is tuned. Now the magnetic plasma

frequency is shifted between 32.1 and 31 GHz when the series branch voltage V_{se} is increased. The electric transition frequency is kept constant around 32 GHz. The slight tuning of the effective permittivity occurs because a tuning voltage applied to the CPW signal metallization not only orients the LC between the top and bottom metallization of the glass substrates, but also between the CPW signal and ground. Hence, C_0 , which determines the effective permittivity, is slightly tuned as well.

5.4 Tunable Open Split-Ring Resonator

Due to its small size, the open split-ring resonator (OSRR) [38] is an attractive element for the design of compact planar filters and transmission line metamaterials. The possibility of voltage tuning has been demonstrated in [39] for varactor loaded open split-ring resonators and their complementary version.

An open split-ring resonator in the series branch of a transmission line can be described by the equivalent circuit in Fig. 5.23. It consists of a series resonator with $L_{se} + L_{ring}$ and C_{se} and the losses R_{se} . The effective permittivity of the host medium is modeled by the shunt capacitor C_0 . The OSRR is not excited by the magnetic field on the transmission line but by the current in the series branch. The ring forms a series inductor L_{ring} while the opposing areas of the rings form the capacitor C_{ring} .

Due to the Drude dispersion of the effective permeability caused by the series branch, and the constant effective permittivity, the propagation constant of the OSRR transmission line is

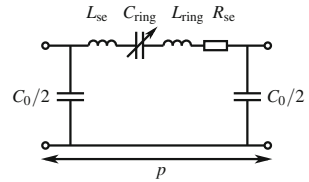
$$\gamma p = \pm \sqrt{Z_{se} Y_{sh}} = \pm \sqrt{(L_{se} + L_{ring}) C_0 \left(\omega_{p\mu}^2 - \omega^2 + j\omega \frac{R_{se}}{L_{se} + L_{ring}} \right)} \quad (5.21)$$

and the characteristic impedance

$$Z = \pm \sqrt{\frac{Z_{se}}{Y_{sh}}} = \pm \sqrt{\frac{L_{se} + L_{ring}}{C_0}} \sqrt{\frac{\omega^2 - \omega_{p\mu}^2 - j\omega R_{se}/(L_{se} + L_{ring})}{\omega^2}}. \quad (5.22)$$

Above the magnetic plasma frequency

Fig. 5.23 Circuit of the open split-ring resonator unit cell with a tunable series resonator in the series branch



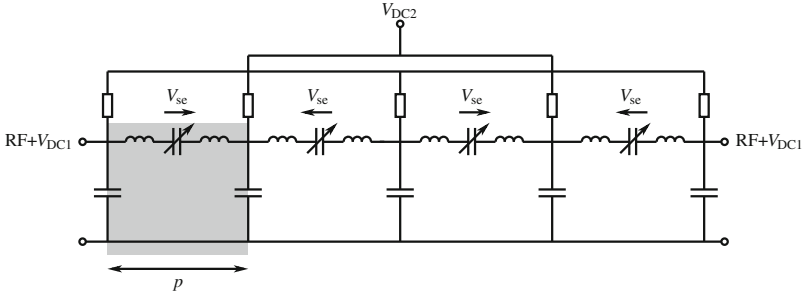
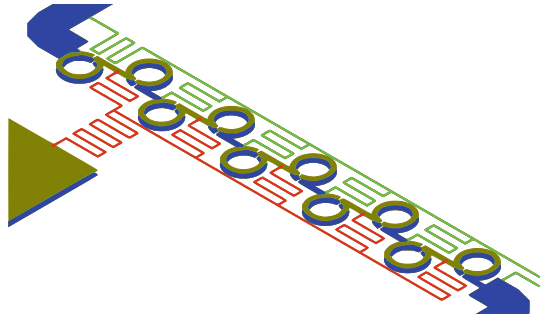


Fig. 5.24 Biasing schematic of a tunable OSRR array with 4 unit cells

Fig. 5.25 3D view of the open split-ring resonator array. Shown are the RF gold layers and the nickel-chromium layer for the resistive biasing network



$$\omega_{p\mu} = \frac{1}{\sqrt{(L_{se} + L_{ring})C_{ring}}} \quad (5.23)$$

a propagation band occurs and the propagation constant γ becomes imaginary while the characteristic impedance becomes real. With a tunable series capacitor C_{se} it is possible to tune the phase and impedance at a certain frequency. Since only the series branch is tunable, with this unit cell configuration it is not possible to tune the electric response and thus, to independently tune the phase and impedance of the configuration.

Figure 5.24 shows an array consisting of four OSRR unit cells and a possible implementation of the biasing network for a metallization layout as depicted in Fig. 5.25. One voltage is applied to one of the RF ports using a bias tee while a second voltage is applied via a DC contact pad on the substrate so that the varactor voltage is

$$V_{se} = V_{DC1} - V_{DC2}. \quad (5.24)$$

The layout of the realized OSRR transmission line is shown in Fig. 5.25 with the dielectric and metallic layers as shown in Fig. 5.26. Compared to [38], the rings of the OSRR here are broadside coupled with an LC layer between the rings. That increases the overlapping area between the rings and hence, the tunable capacitor

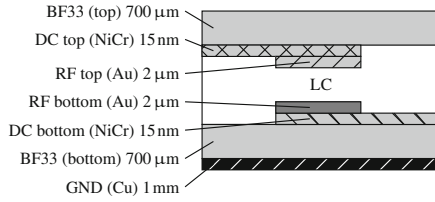


Fig. 5.26 Dielectric and metal layers of the open split-ring resonator structure

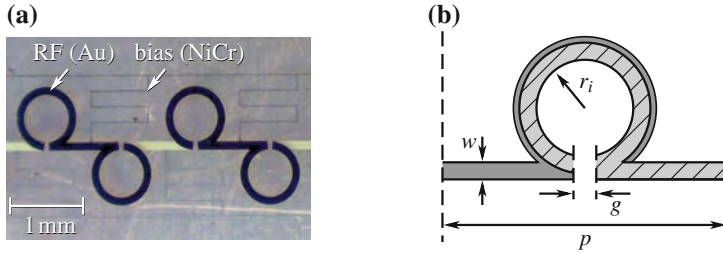


Fig. 5.27 Tunable open split-ring resonator: **a** detail photo of the realized structure, **b** unit cell geometry (dimensions: $p = 1 \text{ mm}$, $r_i = 300 \mu\text{m}$, $w = g = 10 \mu\text{m}$)

C_{ring} . Furthermore, a ground plane window is not implemented due to the large aspect ratio between the ring distance of $100 \mu\text{m}$ and the substrate thickness of $700 \mu\text{m}$. Like for the fabrication of the structure in Sect. 5.3, two BF33 glass substrates are glued on top of each other while glass spheres with a diameter of $100 \mu\text{m}$ act as spacers to form the LC cavity between the substrates. A photo of the fabricated structure can be seen in Fig. 5.27a with four OSRR unit cells including the meander bias lines. The dimensions of the unit cell geometry are depicted in Fig. 5.27b.

Simulations are carried out in Agilent ADS with an isotropic and homogeneous dielectric layer representing the LC layer. Figure 5.28 shows the resulting simulated frequency response of the Bloch impedance and unit cell phase shift. It can be seen that the magnetic plasma frequency is shifted from 13 to 12 GHz if the biasing field is applied, i.e. if the LC permittivity is tuned from $\epsilon_{r,LC\perp} = 2.47$ (unbiased) to $\epsilon_{r,LC\parallel} = 3.16$ (biased). At the design frequency of 16 GHz the Bloch impedance is close to 50Ω for all tuning states.

The measured transmission and input reflection of an array of 10 unit cells for different tuning voltages are shown in Fig. 5.29. The tuning of the lower cutoff frequency between 13 and 14 GHz can be clearly observed. At the design frequency of 16 GHz the unit cell transmission is better than $-0.3 \text{ dB/unit cell}$ with a matching better than -10 dB .

The measured real part of the Bloch impedance for a tuning voltage of 0 and 120 V is shown in Fig. 5.30. It is smaller than predicted by the simulation in the transmission band and shifts between 25 and 40Ω at 16 GHz.

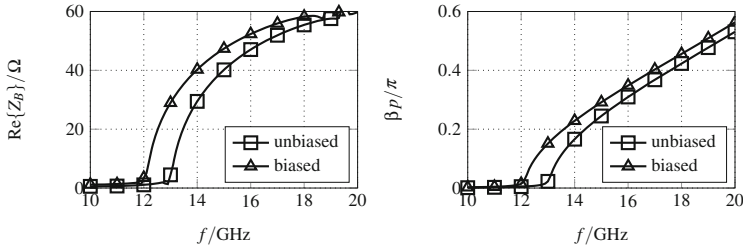


Fig. 5.28 Simulated real part of Bloch impedance and unit cell phase shift for the biased and unbiased state of the OSRR unit cell

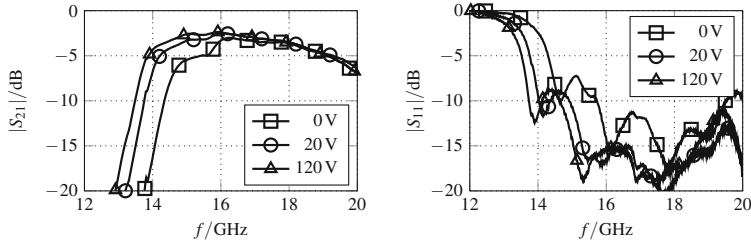


Fig. 5.29 Measured forward transmission and input reflection of a 10 unit cell OSRR array

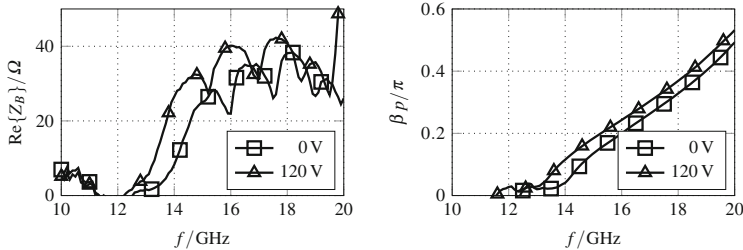


Fig. 5.30 Measured real part of Bloch impedance and unit cell phase shift for the biased and unbiased state of the OSRR array consisting of 10 unit cells

In the measured unit cell phase shift in Fig. 5.30 it can be seen that the cutoff frequency, i.e. the magnetic plasma frequency, is shifted from 14 to 13 GHz if the tuning voltage is increased from 0 to 120 V. The discrepancy between the simulation and measurements is caused by the bias lines. Due to the critical etching time of a few seconds of the NiCr layer, their thickness cannot be controlled precisely. That directly affects the resistance of the resistive bias network and hence, the coupling between the unit cells.

A variety of planar unit cell topologies and configurations exists and the suitability of each depends on the specific application. Hence, the tunable unit cells presented here cover a small field of possible applications. However, the concepts, demonstrated for the double series unit cell and the open-split ring resonator, could be applied for the

implementation of other voltage tunable configurations, especially for frequencies above 10 GHz.

References

1. G. Eleftheriades, A. Iyer, P. Kremer, Planar negative refractive index media using periodically l-c loaded transmission lines. *IEEE Trans. Microw. Theory Tech.* **50**, 2702–2712 (2002)
2. A. Iyer, G. Eleftheriades, Negative refractive index metamaterials supporting 2-d waves, in *2002 IEEE MTT-S International Microwave Symposium Digest*, (2002) vol. 2, pp. 1067–1070
3. C. Caloz, T. Itoh, Novel microwave devices and structures based on the transmission line approach of meta-materials, in *2003 IEEE MTT-S International Microwave Symposium Digest* (2003) vol. 1, pp. 195–198
4. C. Caloz, T. Itoh, Transmission line approach of left-handed (lh) materials and microstrip implementation of an artificial lh transmission line. *IEEE Trans. Antennas Propag.* **52**, 1159–1166 (2004)
5. A. Lai, T. Itoh, C. Caloz, Composite right/left-handed transmission line metamaterials. *IEEE Microw.* **5**(3), 34–50 (2004)
6. M. Gil, J. Bonache, J. Selga, J. García-García, F. Martín, High-pass filters implemented by composite right/left handed (crlh) transmission lines based on complementary split rings resonators (csrrs). *PIERS online* **3**(3), 251–253 (2007)
7. C. Damm, M. Schübler, J. Freese, R. Jakoby, Artificial line phase shifter with separately tunable phase and line impedance, in *Proceeding of the 36th European Microwave Conference* (2006) pp. 423–426
8. A. Giere, C. Damm, P. Scheele, R. Jakoby, Lh phase shifter using ferroelectric varactors, in *Proceeding of the IEEE Radio and Wireless Symposium* (2006) pp. 403–406
9. C. Caloz, A. Sanada, T. Itoh, A novel composite right/left-handed coupled-line directional coupler with arbitrary coupling level and broad bandwidth. *IEEE Trans. Microw. Theory Tech.* **52**, 980–992 (2004)
10. L. Liu, C. Caloz, T. Itoh, *Electron. Lett.* **38**(2), 1414–1416 (2002)
11. C. Caloz, T. Itoh, A. Rennings, Crlh metamaterial leaky-wave and resonant antennas. *IEEE Antennas Propag. Mag.* **50**, 25–39 (2008)
12. D. Jackson, C. Caloz, T. Itoh, Leaky-wave antennas. *Proc. IEEE* **100**, 2194–2206 (2012)
13. A. Sanada, C. Caloz, T. Itoh, Novel zeroth-order resonance in composite right/left-handed transmission line resonators. *Proc. Asia-Pacific Microw. Conf.* **3**, 1588–1591 (2003)
14. M. Schübler, C. Damm, J. Freese, R. Jakoby, Realization concepts for compact microstrip antennas with periodically loaded lines, in *Proceeding of the IEEE MTT-S International Microwave Symposium Digest* (2005) pp. 4
15. M. Schübler, C. Damm, M. Maasch, R. Jakoby, Performance evaluation of left-handed delay lines for rfid backscatter applications, in *Proc. IEEE MTT-S International Microwave Symposium Digest* (2008) pp. 177–180
16. C. Damm, M. Schübler, M. Puentes, H. Maune, M. Maasch, R. Jakoby, Artificial transmission lines for high sensitive microwave sensors (2009)
17. C. Damm, M. Maasch, M. Schübler, R. Jakoby, Double series and double parallel unit cells for transmission line metamaterials. *Electron. Lett.* **46**(2), 112–113 (2010)
18. C. Caloz, Dual composite right/left-handed (D-CRLH) transmission line metamaterial. *IEEE Microw. Wirel. Compon. Lett.* **16**, 585–587 (2006)
19. F. Gölden, A. Gäbler, M. Göbel, A. Manabe, S. Müller, R. Jakoby, Tunable liquid crystal phase shifter for microwave frequencies. *Electron. Lett.* **45**, 686–687 (2009)
20. A. Mössinger, R. Marin, S. Müller, J. Freese, R. Jakoby, Electronically reconfigurable reflectarrays with nematic liquid crystals. *Electron. Lett.* **42**(1), 899–900 (2006)

21. W. Hu, R. Cahill, J. Encinar, R. Dickie, H. Gamble, V. Fusco, N. Grant, Design and measurement of reconfigurable millimeter wave reflectarray cells with nematic liquid crystal. *IEEE Trans. Antennas Propag.* **56**, 3112–3117 (2008)
22. W. Hu, R. Dickie, R. Cahill, H. Gamble, Y. Ismail, V. Fusco, D. Linton, N. Grant, S. Rea, Liquid crystal tunable mm wave frequency selective surface. *IEEE Microw. Wirel. Compon. Lett.* **17**, 667–669 (2007)
23. F. Zhang, G. Houzet, E. Lheurette, D. Lippens, M. Chaubet, X. Zhao, Negative-zero-positive metamaterial with omega-type metal inclusions. *J. Appl. Phys.* **103**(8), 084312 (2008)
24. F. Zhang, Q. Zhao, W. Zhang, J. Sun, J. Zhou, D. Lippens, Voltage tunable short wire-pair type of metamaterial infiltrated by nematic liquid crystal. *Appl. Phys. Lett.* **97**(13) (2010)
25. C. Damm, M. Maasch, R. Gonzalo, R. Jakoby, Tunable composite right/left-handed leaky wave antenna based on a rectangular waveguide using liquid crystals (2010) pp. 13–16
26. M. Roig, M. Maasch, C. Damm, R. Jakoby, Liquid crystal-based tunable crlh-transmission line for leaky wave antenna applications at ka-band. *Int. J. Microw. Wirel. Technol.* **6**(3–4), 325–330 (2014)
27. P.G. de Gennes, J. Prost, *The Physics of Liquid Crystals*, International series of monographs on physics (Clarendon Press, Oxford, 1995)
28. P. Collings, M. Hird, *Introduction to Liquid Crystals: Chemistry and Physics*, Liquid Crystals Book Series (Taylor & Francis, Boca Raton, 1997)
29. D. Yang, S. Wu, *Fundamentals of Liquid Crystal Devices*, Wiley Series in Display Technology (Wiley, New York, 2006)
30. A. Gäbler, F. Gölden, S. Müller, R. Jakoby, Multiphysics simulations for tunability efficiency evaluation of liquid crystal based rf. *Frequenz* **62**(9–10), 240–245 (2008)
31. A. Gäbler, F. Gölden, S. Müller, R. Jakoby, Modeling of electrically tunable transmission line phase shifter based on liquid crystal, in 2008. *AP-S 2008. IEEE Antennas and Propagation Society International Symposium* (2008) pp. 1–4
32. G. Perez-Palomino, R. Florencio, J. A. Encinar, M. Barba, R. Dickie, R. Cahill, P. Baine, M. Bain, R.R. Boix, Accurate and efficient modeling to calculate the voltage dependence of liquid crystal based reflectarray cells (2014)
33. R. Dudley, M. Naftaly, Thz optical constants of liquid crystals bl037 and gt3-23001, in *2013 6th UK Millimeter Waves and THz Technology Workshop (UCMMT)* (Europe, China, 2013), pp. 1–2
34. C. Weickhmann, R. Jakoby, E. Constable, R. Lewis, Time-domain spectroscopy of novel nematic liquid crystals in the terahertz range, in *2013 38th International Conference on Infrared, Millimeter, and Terahertz Waves (IRMMW-THz)* (2013) pp. 1–2
35. F. Gölden, A. Gäbler, S. Müller, A. Lapanik, W. Haase, R. Jakoby, Liquid-crystal varactors with fast switching times for microwave applications. *Electron. Lett.* **44**(7), 480–481 (2008)
36. F. Gölden, Liquid crystal based microwave components with fast response times: material, technology, power handling capability. Ph.D. thesis, Technische Universität Darmstadt, Fachgebiet Mikrowellentechnik (2010)
37. O. H. Karabey, Electronic beam steering and polarization agile planar antennas in liquid crystal technology. Ph.D. thesis, TU Darmstadt, Cham, 2014. Zugl. Darmstadt, Techn. Univ., Diss (2013)
38. J. Martel, R. Marqués, F. Falcone, J. Baena, F. Medina, F. Martín, M. Sorolla, *IEEE Microw. Wirel. Compon. Lett.* **14**, 210–212 (2004)
39. A. Véandlez, F. Aznar, M. Durán-Sindreu, J. Bonache, F. Martín, Tunable coplanar waveguide band-stop and band-pass filters based on open split ring resonators and open complementary split ring resonators, *IET Microwaves, Antennas Propagation* (2011) vol. 5(21), pp. 277–281

Chapter 6

Artificial Gradient-Index Lens

Metamaterials for the microwave region are of special interest in the design of three-dimensional structures such as artificial lenses [1–4], absorbers [5], or cloaking devices [6, 7], since the electric and magnetic response, i.e. effective permittivity and permeability, can be tailored independently of each other. This can be done by employing fundamental elements like split-ring resonators and wires to influence the magnetic and electric field of an incident wave.

By using a combination of SRRs [8] and wires [9], a desired frequency response can be tailored and realized with tunable properties. Depending on the frequency range of operation and technological limitations, variations like omega resonators [10, 11], S-shaped resonators [12, 13], or fishnet elements [14, 15] can be employed. Like the SRR–wire combination, these particles exhibit a Lorentz–Drude or double-Lorentz response. By introducing voltage tunable elements such as varactor diodes or materials like liquid crystal, tunable particles can be designed. These allow reconfiguration of phase and impedance at a fixed frequency or a tuning to cover a larger frequency band of operation.

In this chapter, tunability is introduced to different unit cell structures such as split-ring resonators, omega resonators, and fishnet metamaterials. To investigate the applicability for complex three-dimensional structures, unit cells are loaded with varactor diodes and liquid crystal material. Furthermore, by introducing a voltage tunable gradient in a fishnet array, the beam scanning capability of a gradient-index metamaterial with a tunable scan angle is demonstrated. Different implementations and characterization methods, which take realizability and technological constraints of complex arrays into account, are demonstrated by guided wave and free space characterization methods.

6.1 Gradient-Index Structures for Beam Scanning

The working principle of a gradient-index structure consisting of N unit cells transversal to an incident wave is shown in Fig. 6.1. The phase shift ϕ_n is linearly increased in x -direction yielding a constant phase gradient

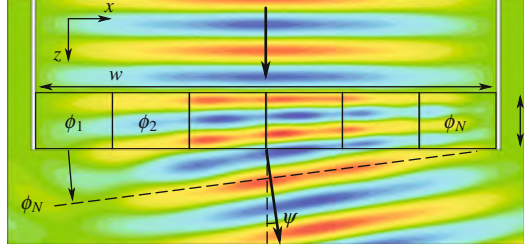


Fig. 6.1 Working principle of the gradient-index lens: The phase shift ϕ_n is linearly increased over the lens aperture yielding the radiation angle ψ . ϕ_1 and ϕ_N represent the maximum and minimum phase shift and w the array width [16], © 2014 IEEE

$$\frac{\Delta\phi(\omega)}{\Delta x} = \frac{\phi(x_0) - \phi(x_0 + w)}{w} = \frac{\phi_1 - \phi_N}{w} \quad (6.1)$$

where w is the width of the lens. The non-constant phase distribution over the aperture of the lens creates a frequency dependent refraction of the incident wave with the angle

$$\psi \left(\omega, \frac{\Delta\phi}{\Delta x} \right) = \sin^{-1} \left(\frac{c_0}{\omega} \cdot \frac{\Delta\phi(\omega)}{\Delta x} \right). \quad (6.2)$$

With an increasing phase gradient $\frac{\Delta\phi}{\Delta x}$, the beam scanning angle is increased. By increasing the lens width w , the half-power beam width of the radiated beam can be decreased, but at the same time this also reduces the phase gradient $\frac{\Delta\phi}{\Delta x}$ and thus, the scanning angle ψ . Hence, for a specific application, a compromise has to be found between the half-power beam width and the scanning angle if the maximum achievable phase difference $|\Delta\phi_{\max}| = |\phi_1 - \phi_N|$ is smaller than 2π .

For $|\Delta\phi_{\max}| \geq 2\pi$, the phase periodicity can be exploited by applying a Fresnel-lens profile [17–19] over the aperture as shown in Fig. 6.2. In each zone with the width s , the phase shift ϕ is increased from 0 to 2π . Due to phase wrapping, the phase gradient that determines the radiation direction, becomes

$$\frac{\Delta\phi(\omega)}{\Delta x} = \frac{\phi(x_0) - \phi(x_0 + s)}{s}. \quad (6.3)$$

The radiation angle ψ is not limited by the aperture size w so that a large scanning angle together with a small half-power beam width can be realized.

This principle is demonstrated for a discretized gradient-index lens with an aperture size of $w = 90$ mm discretized by 18 unit cells. The operation frequency is 22.5 GHz. With a maximum phase difference of $|\Delta\phi_{\max}| = 2\pi$, the maximum phase gradient is $\left| \frac{\Delta\phi}{\Delta x} \right| = \frac{2\pi}{85 \text{ mm}}$, and the maximum beam scanning range is $\pm 9^\circ$.

A larger scanning angle with the same geometry requires a larger phase difference or a wrapping of the phase at 2π . e.g., for a radiation angle of $\psi = 32^\circ$, a phase difference of $|\Delta\phi| = 6.8\pi$ over the complete aperture with the width w is required and the phase gradient becomes $\left| \frac{\Delta\phi}{w} \right| = \frac{6.8\pi}{85 \text{ mm}} = 0.08 \frac{\pi}{\text{mm}}$. However, as shown in

Fig. 6.2 Working principle of a Fresnel lens: in each section the phase is linearly increased

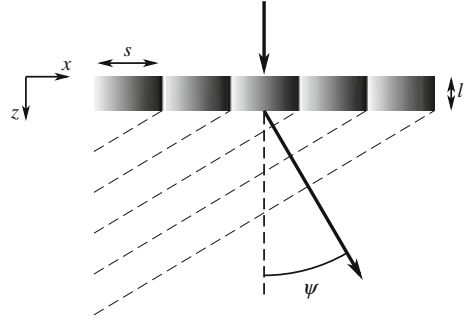


Fig. 6.3 Required phase distribution of a discretized gradient-index lens with continuous phase increment (*unwrapped*) and with a Fresnel phase profile (*wrapped*) for a radiation angle of $\psi = 32^\circ$

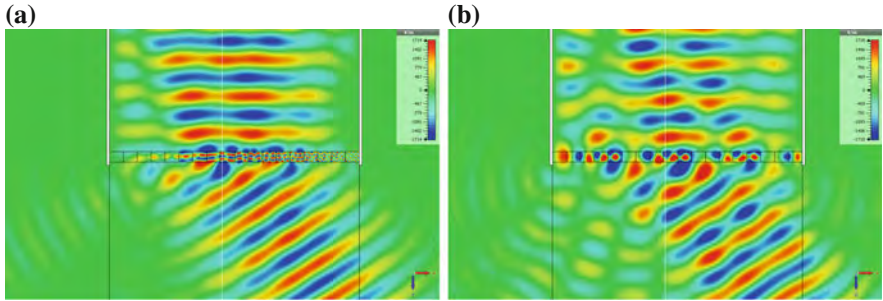
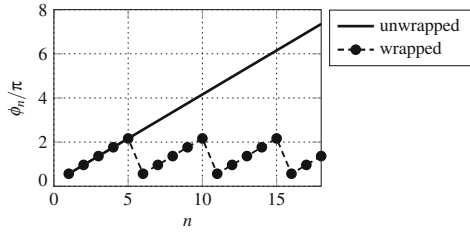


Fig. 6.4 Electric field distribution of a discretized gradient-index lens: **a** with continuous phase increment of $\Delta\phi = 6.8\pi$ over the aperture, **b** with a Fresnel phase profile

Fig. 6.3, the same radiation angle can be achieved with a phase wrapping at $|\Delta\phi| = 2\pi$ and introduction of four zones with the width s . The phase gradient is $\left|\frac{\Delta\phi}{s}\right| = \frac{2\pi}{25\text{ mm}} = 0.08 \frac{\pi}{\text{mm}}$, yielding the same radiation angle of 32° .

A comparison of the electric field distribution of the discretized gradient-index lens in the xz -plane is shown in Fig. 6.4 for a phase difference of 6.8π over the complete aperture (Fig. 6.4a) and for a Fresnel phase profile with a phase difference of 2π in each zone (Fig. 6.4b). The Fresnel lens consists of four zones with a linearly increasing phase from 0 to 2π in each zone as depicted in Fig. 6.3. Since for both configurations the phase gradient is identical, the incident normal wave is refracted with an angle of 32° , which confirms the analytic value. Differences occur mainly for the side lobes.

Fig. 6.5 Farfield pattern of a discretized gradient-index lens with continuous phase increment (*unwrapped*) and with a Fresnel phase profile (*wrapped*)

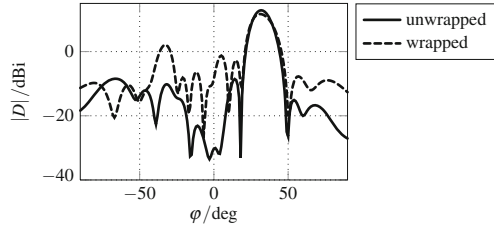


Figure 6.5 shows the simulated directivity in the xz -plane for the continuous and the Fresnel phase distribution, respectively. The main lobe direction and magnitude are in agreement for both configurations and the main lobe directions confirms the theoretical value of 32° . As expected from the nearfield results, the side lobes are increased for the Fresnel profile with phase wrapping.

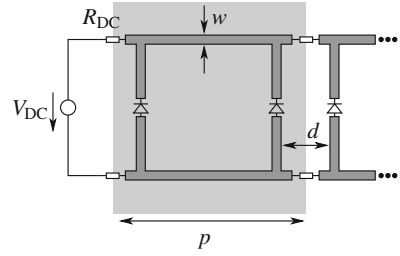
Equation (6.2) illustrates that only the sign of the phase gradient $\frac{\Delta\phi}{\Delta x}$ and not the sign of the phase ϕ_n itself determines the direction of the transmitted wave, i.e. the sign of the radiation angle ψ . Hence, it is not crucial to have a negative phase, i.e. a simultaneously negative effective permeability and permittivity, to achieve scanning to negative angles. This is particularly important if the dispersion of the effective permeability is taken into account: A negative effective permeability is realized with a Lorentz dispersion near the magnetic resonance frequency. This, however, is the region with largest magnetic losses. Since for the gradient-index lens the phase ϕ_n does not have to be negative, it is instead possible to work in the positive permeability region below the magnetic resonance frequency, where the effective permeability shows a strong dispersion and hence, a high tunability, but moderate magnetic losses.

6.2 Tunable Split-Ring Resonator

For microwave frequencies it has been demonstrated that split-ring resonators can be applied in three-dimensional devices such as gradient-index structures. In [1, 2] the magnetic resonance frequency is varied to create a gradient of the effective permeability and hence, of the phase. However, this gradient is fixed since it is created by varying the geometry of split-ring resonators. In [20, 21] it has been demonstrated that by loading the gap of a split-ring resonator in planar configurations with semiconductor varactors or ferroelectric material, the magnetic resonance frequency can be tuned by a DC voltage. Although non-planar configurations with a tunable magnetic resonance frequency exist [22, 23], a realization of a three-dimensional array of such tunable split-ring resonators is very challenging due to the complex biasing network. Here, a biasing scheme for split-ring resonators loaded with semiconductor varactors, which can be applied also in larger arrays, is presented and investigated.

To tune the effective permeability of an array of split-ring resonators at a fixed frequency, it is necessary to shift their magnetic resonance frequency. This can either

Fig. 6.6 Principle diagram of the DC biased SRRs, $p = 9 \text{ mm}$, $w = 0.55 \text{ mm}$, $d = 1.5 \text{ mm}$



be achieved by tuning the ring inductance L_{ring} or the gap capacitor C_{gap} , where tuning the gap capacitor is more practical in terms of implementation. The convenient position of the tunable capacitor differs depending on the shape of the split-ring resonators. For broadside-coupled split-ring resonators (BC-SRR), the main capacitance is between the rings on two sides of a substrate. To tune this capacitance, varactors have to be located between the two sides of the substrate and vias are required to contact them to the rings. A similar problem occurs with edge-coupled split-ring resonators (EC-SRR) where the varactor has to be placed between the inner and outer ring or in the gap of the outer ring of the EC-SRR unit cell [24, 25]. Due to the interleaved rings, the tuning voltage for the inner ring only can be applied from the second substrate side which requires via connections and results in a more complex biasing network.

Figure 6.6 shows a split-ring resonator with two gaps which are each loaded with a semiconductor varactor. By introducing two gaps, two separate DC paths are created and at the same time, the symmetry of the unit cell in propagation direction is maintained and a bi-anisotropic response is prevented. A DC tuning voltage can be applied between the upper and lower half of each split-ring resonator to tune the varactor capacitance. To distribute the tuning voltage in an array of split-ring resonators, adjacent unit cells are connected by the resistors R_{DC} . The reverse current I_r of each varactor diode causes a voltage drop on the DC coupling resistors R_{DC} . Thus, the voltage drop before the n th SRR is

$$V_{R,n} = 4R_{\text{DC}}I_r(N - n + 1) \quad (6.4)$$

where N is the total number of unit cells. The varactor voltage at the n th SRR inside an array is

$$V_n = V_{\text{DC}} - \sum_{k=1}^n V_{R,k} = V_{\text{DC}} - 4n \left(N + \frac{1-n}{2} \right) R_{\text{DC}}I_r. \quad (6.5)$$

To minimize the DC tuning voltage difference between adjacent unit cells it is necessary to apply varactors with a small reverse current I_r . In the presented prototype, varactor diodes BB857 by Infineon are employed with a reverse current of 25 pA.

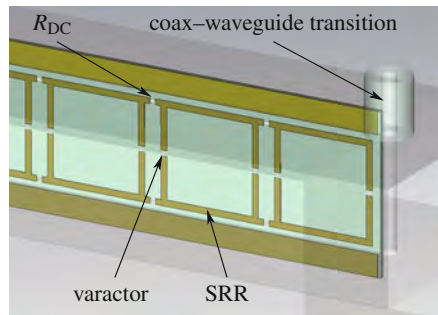
For an array consisting of nine unit cells and with $R_{DC} = 100 \text{ k}\Omega$, the maximum varactor voltage difference between the first and last unit cell is only $360 \text{ }\mu\text{V}$.

The square shape is chosen for the rings. This allows the implementation of the DC connection and the RF decoupling between the SRRs with SMD resistors. Since the unit cell size is not increased by the biasing network, the biasing scheme in Fig. 6.6 can be applied to complex three-dimensional periodic arrangements of SRRs. Another benefit is that the already existing RF structure is used to distribute the DC tuning voltage. Hence, no additional biasing lines are required which simplifies the manufacturing process and reduces parasitic effects.

Measurement of the response of an implemented array of split-ring resonators is possible with different approaches. Fabrication of an array consisting of a large number of unit cells in propagation direction as well as transversal to the propagation direction [26] is challenging since a large number of substrates have to be aligned in parallel to each other. Furthermore, a large number of SMD varactors and biasing elements are required. In contrast, measurement of a single unit cell element [25] does not take the effects of the biasing network and higher order mode coupling into account. As a compromise, a rectangular hollow waveguide described in [27–29], which has well defined boundary conditions for measurements, is used here. Hence, only a single unit cell transversal to the propagation direction is required while in propagation direction a high number of unit cells can be implemented to consider higher order mode coupling between adjacent unit cells.

If the split-ring resonators are positioned as shown in Fig. 6.7 in the transversal center of the waveguide, they are only excited by normal magnetic field components as in the case of a plane wave excitation. However, the waveguide itself shows a dispersive characteristic. This has to be taken into account but is not critical for the present investigation since the waveguide yields a Drude dispersion for the effective permittivity if the propagating mode is a TE mode (3.38). Since the split-ring resonators and their effective permeability do not affect the dispersion of the effective permittivity created by the waveguide and vice versa, they can be investigated separately. Beyond the characterization purpose, the principle of a hollow waveguide loaded with voltage tunable split-ring resonators has been demonstrated for the application in voltage tunable leaky-wave antennas [30, 31].

Fig. 6.7 CST model detail of the coax to waveguide transition and tunable SRR array inside the waveguide test fixture. The DC bias resistors are positioned over the *horizontal* gaps between adjacent SRRs, the varactor diodes over the *vertical* SRR gaps



The fabricated array consists of 9 unit cells in propagation direction with the dimensions as shown in Fig. 6.6. These dimensions allow measurements inside a WR90 waveguide with a TE₁₀ cutoff frequency of 6.56 GHz. Below this, the waveguide shows a negative effective permittivity due to the Drude dispersion (3.38). As substrate, Rogers RO5880 with a thickness of 0.38 mm is used.

Simulations of the unit cell as well as the array, both inside the WR90 waveguide, are carried out in two steps. In the fullwave simulation using the frequency domain solver in CST Microwave Studio, each lumped element, i.e. varactor diodes and resistors, is replaced by a discrete port. In a second simulation step, these discrete ports are loaded with scattering parameters representing the discrete SMD elements. This is possible since the unit cells as well as the lumped elements are linear and reciprocal. That way, the time consuming fullwave simulation has to be performed only once while the final response of the unit cell and the array for different tuning states or different capacitive and resistive loads can be carried out with a fast circuit simulation based on scattering parameters. Another benefit is that for the lumped elements measured scattering parameters from precise element characterizations can be included in the simulation.

The obtained real parts of the effective material parameters of a single SRR unit cell without the biasing resistors inside a WR90 waveguide are shown in Fig. 6.8 for different tuning voltages in 4 V steps. The effective permittivity is negative over a broad frequency band following the Drude dispersion (caused by the excitation of TE₁₀ mode of the waveguide) while the effective permeability is negative between the magnetic resonance and transition frequency. By tuning the varactor voltage from 4 to 24 V, the magnetic resonance frequency is shifted between 0.75 and 1.7 GHz. Besides the anti-resonance caused by spatial dispersion due to the large phase, the effective permittivity is unaffected by the tuning since it is only determined by the waveguide geometry. Since both, μ'_{eff} and ϵ'_{eff} are simultaneously negative, a backward wave transmission band occurs above the magnetic resonance frequency and below the waveguide cutoff frequency [32–34].

With the varactor capacitance, which is tuned between 0.8 pF and 4 pF, and the magnetic resonance frequency

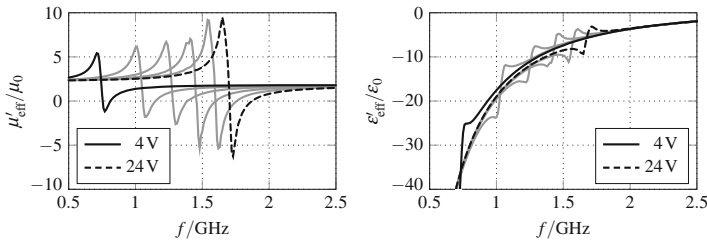


Fig. 6.8 Simulated effective material parameters of the voltage tunable SRR in a WR90 hollow waveguide (intermediate tuning states in 4 V steps are plotted in gray)

Fig. 6.9 Surface current density of the SRR unit cell inside the waveguide

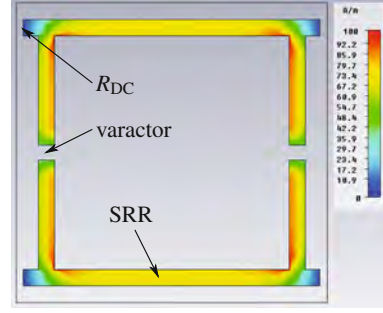
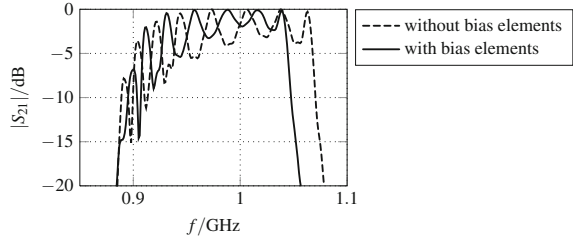


Fig. 6.10 Simulated impact of the biasing elements for an array of 9 unit cells and a varactor voltage of 20 V



$$\omega_{0\mu}^2 = \frac{1}{L_{\text{ring}} C_{\text{varactor}}}, \quad (6.6)$$

the ring inductance yields $L_{\text{ring}} = 22.5 \text{ nH}$.

The major part of losses in the magnetic response is due to metallic losses of the SRR. As it can be seen in Fig. 6.9, the current density is very high in the SRR corners. Furthermore, no current flows via the connection pads for the bias resistors in each corner, which means that the impact of the bias network connected to these points will be comparatively small.

To determine the impact of the resistive biasing network on the response of the SRR array inside the waveguide, a simulation of the lossless array consisting of 9 unit cells is carried out with and without biasing elements. As it can be seen in the detailed view of the backward wave transmission band in Fig. 6.10, the biasing network only has a minor effect on the frequency characteristic. The varactor capacitance is set to 3 pF while the biasing resistors are modeled as a resistance of 100 kΩ with a parasitic parallel capacitance of 0.5 pF. Due to increased coupling between adjacent SRRs caused by the biasing elements, the backward wave transmission band gets slightly narrower while its position is not changed.

The simulation of a single unit cell as does not consider higher order mode coupling between adjacent unit cells. However, higher order modes can strongly contribute to the propagation in the macroscopic structure, i.e. effective material parameters obtained with a fundamental mode excitation are not always sufficient to describe the response of the macroscopic structure. Therefore, a simulation of the complete characterization setup is carried out following the approach in Sect. 4.1.2.

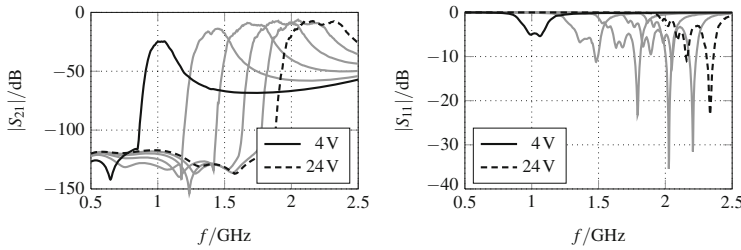


Fig. 6.11 Simulated transmission and input reflection of the complete SRR loaded waveguide for different biasing voltages (intermediate tuning states in 4 V steps are plotted in *gray*)

Since the coax–waveguide transitions are included in this simulation, the definition of effective material parameters loses its meaning if they are extracted from the complete structure. Yet, obtained scattering parameters yield information about the position of the backward wave band and its tuning.

The simulated scattering parameters of the complete characterization setup are shown in Fig. 6.11 for different tuning voltages. For the lumped elements, i.e. the bias resistors and the varactor diodes, measured scattering parameters are used in combination with the fullwave simulation of the loaded waveguide. The center frequency of the backward wave transmission band below the waveguide cutoff frequency of 6.56 GHz can be tuned between 1 and 2.2 GHz. The shift of the backward wave band to a slightly higher frequency compared to the transmission band predicted by the effective material parameters is caused by the higher order mode coupling. The degraded matching for lower frequencies is due to the waveguide dispersion. Since the waveguide is not affected by the tuning, the effective permittivity changes for each tuned transmission band as shown in Fig. 6.8. Hence, the Bloch impedance in the transmission band changes with the tuning voltage.

Figure 6.12 shows a photo of the opened WR90 waveguide used for the measurements and the array of 9 split-ring resonators. Above and below the SRRs a metallization strip is visible. This metallization is connected to the waveguide and sticks out by 0.1 mm into the waveguide to form a defined and constant distance between the SRR and RF ground potential.

A comparison of the simulated and measured scattering parameters of the backward wave band are shown in Fig. 6.13 for a varactor voltage of 20 V. The frequency of the backward wave band is predicted well by the simulation, while the measured bandwidth is smaller. This is caused by a variation of the varactor capacitances and stronger coupling via the biasing resistors between adjacent unit cells due to the soldering and manufacturing process.

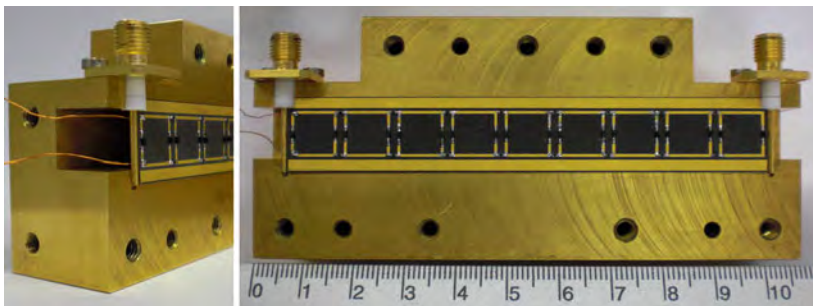


Fig. 6.12 Photo of the SRR loaded waveguide with 9 tunable unit cells

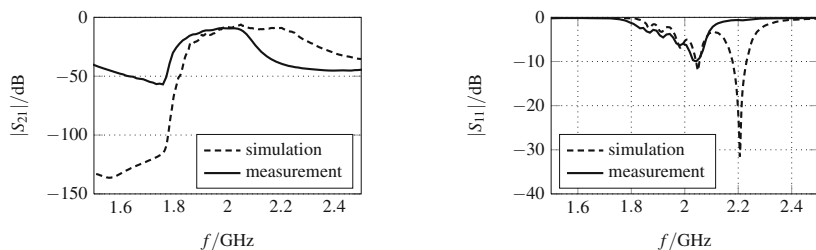


Fig. 6.13 Comparison of simulated and measured transmission and input reflection for a tuning voltage of 20 V

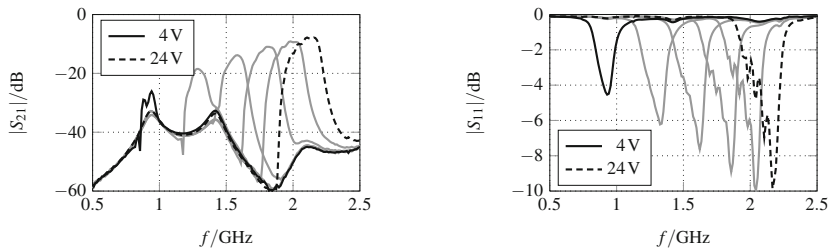


Fig. 6.14 Measured transmission and input reflection for different biasing voltages (intermediate tuning states in 4 V steps are plotted in gray)

The measured transmission and input reflection for different tuning voltages in 4 V steps are shown in Fig. 6.14. The backward wave transmission band is shifted from 0.9 to 2.2 GHz for a voltage between 4 and 24 V which agrees with the theoretical frequency tuning range. As expected from simulations, for low frequency transmission bands matching is degraded due to the larger negative effective permittivity. For transmission bands above 2 GHz, the transmission is better than -1 dB/unit cell.

6.3 Tunable Omega Resonator

It has been demonstrated that varactor loaded split-ring resonators can be used to realize a tunable magnetic response in the microwave region. In addition, a wire array can be employed to manipulate the electric response. However, in an array with tunable properties, the separation of the split-ring resonators and wires yields a complex biasing network. A unit cell configuration that combines the magnetic response of the split-ring resonator and the electric response of the wire is the omega resonator [10, 35] that has originally been presented as chiral particle with strong bi-anisotropy. In a broadside-coupled configuration [11, 36–39] as shown in Fig. 6.15, the bi-anisotropic effect is canceled out yielding the typical effective material parameters in Fig. 6.16. The effective permeability shows a resonance at 6.3 GHz and a transition frequency of 8.4 GHz with a negative effective permeability between them. This Lorentz dispersion is caused by the rings [39]. The effective permittivity shows a Drude dispersion with an electric plasma frequency of 8.9 GHz caused by the wires parallel to the incident electric field.

Close to the magnetic resonance frequency, the effective permeability becomes very large yielding a large unit cell phase shift $\phi \approx \pi$ and hence, a strong spatial dispersion as described in Sect. 2.4. This becomes obvious with the anti-resonance of the effective permittivity at the magnetic resonance frequency.

The magnetic response is determined by the rings which are excited by the perpendicular magnetic component of the incident wave. Hence, the resonance and transition frequency are the same as for the split-ring resonator (3.14) and (3.15). On the other hand, the electric response is determined by the arms of the omega resonator which are parallel to the incident electric field yielding a Drude response with the electric plasma frequency (3.4). It can be seen that the gap capacitance has an impact only on the magnetic response. Thus, when a tunable capacitor is introduced, only the magnetic response is tuned while the electric plasma frequency is constant.

Figure 6.15 illustrates that the vertical arms of the omega resonator are connected to the upper and lower unit cells, i.e. all unit cells consist of a metallization that is continuous in vertical direction. This continuous RF metallization can be used at the same time to distribute a DC tuning voltage inside an array.

Fig. 6.15 Broadside-coupled omega resonator unit cell

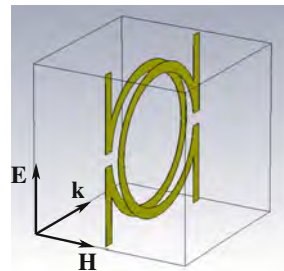


Fig. 6.16 Real part of the effective material parameters of the omega resonator

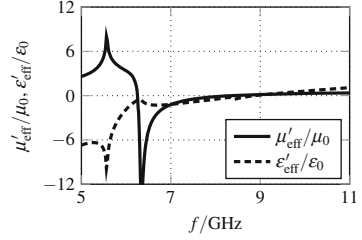
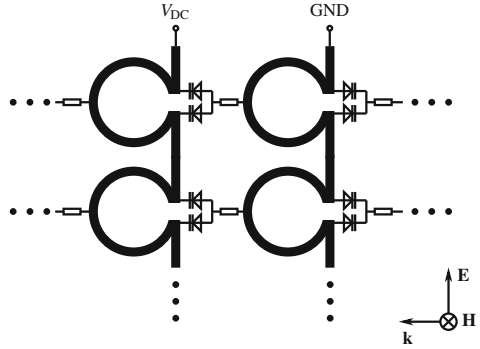


Fig. 6.17 Biasing scheme of an array of varactor loaded omega resonators



A tuning of the magnetic resonance is possible by loading the gaps of overlapping rings with a tunable component. In [40] liquid crystal is used as magnetically tunable material between the broadside-coupled rings. Here, by loading the gaps of the omega resonator with varactor diodes, the magnetic resonance frequency is tuned while the electric response is unaltered. The layout of the unit cell with biasing elements is depicted in Fig. 6.17. Each gap is loaded with two varactor diodes whose common node is connected to the adjacent unit cell via a resistor. Since a vertical array of omega resonators consists of one continuous metallization, this metallization can be used to provide each unit cell with the required DC tuning voltage. In the implementation of an array, special care has to be taken of the first and last unit cell in vertical direction. To maintain the electric boundary condition, which mimics an infinite array in vertical direction, and to avoid additional electric resonances, the arms of the omega resonator have to be connected to a metallic plane. At the same time, DC blocking capacitors have to be introduced to prevent a DC short circuit over the metallic plane between V_{DC} and ground potential.

Characterization Line

When characterizing three-dimensional metamaterials such as split-ring resonators, wires, or omega resonators on substrates which are positioned parallel to the propagation direction of the incident wave, a major challenge is the mechanical positioning and fixing of substrates since they have to be aligned parallel with constant distance to each other. Additionally, for structures like wires or omega resonators, a good

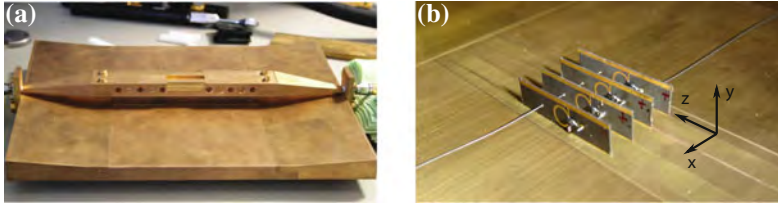


Fig. 6.18 **a** Photo of the complete characterization line, **b** Photo of the characterization line loaded with omega resonators and without the microstrip signal metallization

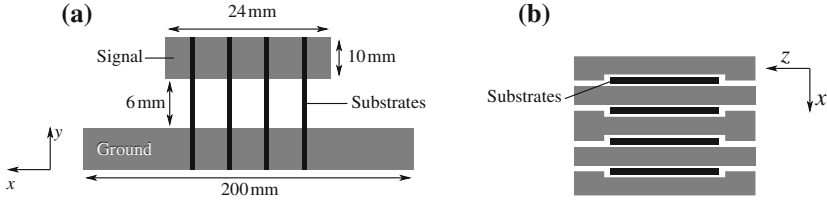


Fig. 6.19 Characterization line: **a** Cross section view transversal to the propagation direction z , **b** Top view of the middle section consisting of layered metal sheets with cutouts for the substrates

RF ground connection of the structures is required to avoid additional resonances in the electric response. A characterization of such structures can be done e.g. with three-dimensional arrays containing a large number of unit cells transversal to the propagation direction. Another solution is to use guided wave structures such as microstrip lines with a field distribution similar to a plane wave in free space, which can then be loaded with the unit cells to be characterized [23]. That way the number of required unit cells is much smaller than for a free space characterization which is convenient especially for tunable unit cells.

On the basis of these considerations and the required ground connection of the arms of the omega particle, the characterization line in Fig. 6.18 based on a microstrip line has been designed. It consists of a substrate fixing section holding the substrates in the middle of the setup, and taper sections at the input and output port. To provide a good RF ground connection and to hold the substrates, signal and ground line are cut in propagation direction z into 5 layers with vertical cutouts. Substrates are positioned in these cutouts and clamped between the metal sheets as shown in Figs. 6.18b and 6.19.

The microstrip characterization line is a compromise in terms of field distribution and the required number of unit cells. The simulation results of the electric and magnetic field distribution of the unloaded characterization line in Fig. 6.20 show that fields in the parallel section between the signal and ground metallization mainly consist of vertical electric field components and horizontal magnetic field components, both close to the field distribution of a plane wave. This is the region where the unit cells to be characterized are positioned. Fringing fields occur close to the corner of the signal line and outside the parallel section.

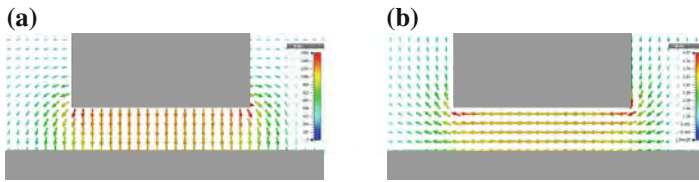


Fig. 6.20 Simulated field distribution of the unloaded characterization line: **a** electric field distribution, **b** magnetic field distribution

Fig. 6.21 Measured real part of line impedance of the empty test fixture

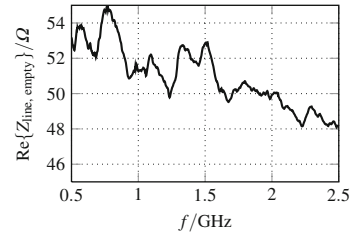
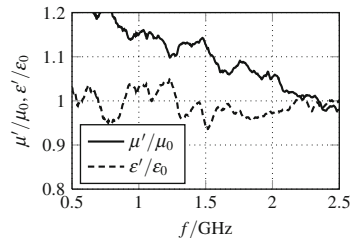


Fig. 6.22 Measured real part of effective permittivity and permeability of the empty characterization line



The characterization line and its taper sections are designed for an impedance of $50\ \Omega$ for a minimum reflection and a simple de-embedding. Thus, after measurements, the taper sections including the coax transitions are de-embedded by assuming a constant line impedance and linearly increasing phase constant of the taper sections. For the unloaded test fixture in Fig. 6.18a, the measured line impedance of the middle section, which will hold the structure to be characterized, is shown in Fig. 6.21. The real part is close to the desired value of $50\ \Omega$. The extracted material parameters in Fig. 6.22 show a relative permeability and permittivity around their ideal values of unity. The ripple is caused by imperfections of the produced taper sections and the transition between the SMA connectors and the taper section, which is sensitive to changes. With a calibration, e.g. a through-reflect-line (TRL) calibration with different standards for the middle section, the error terms that represent the taper sections could be calculated, so that in measurement, the precise scattering parameters of only the middle section are obtained.

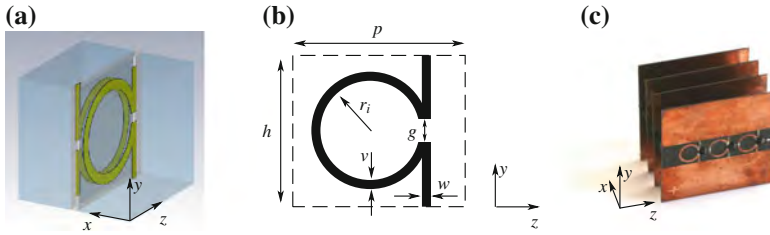


Fig. 6.23 **a** 3D view of the omega resonator unit cell. **b** Layout of the omega resonator unit cell (dimensions in mm: $p = 7$, $h = 6$, $r_i = 2$, $g = 0.4$, $v = 0.5$, $w = 0.4$). **c** Photo of the fabricated $4 \times 1 \times 3$ array

Characterization of Tunable Omega Resonators

To demonstrate the tunability of the omega resonators, the varactor loaded unit cell shown in Fig. 6.23 is designed. It consists of two broadside-coupled omega resonators to maintain the symmetry of the unit cell and hence, to prevent a bi-anisotropic response. Due to loading of the gaps with varactor diodes, the main capacitance is determined by the varactors while the capacitance between the broadside-coupled rings can be neglected. Each gap is loaded with two varactor diodes, whose common node is connected to the adjacent unit cell via a resistor as shown in Fig. 6.24. By loading the gaps of the omega resonators with varactor diodes, the magnetic resonance frequency (3.14) can be tuned by a DC voltage while the electric response is not changed. The capacitors in the arms of the omega resonators prevent a DC short circuit of the DC biasing voltage on the signal metallization of the characterization line.

For the varactor diodes, the Skyworks SMV1232 with a capacitance of 1 pF to 7 pF for a DC voltage between 0 and 15 V at 2 GHz is used. With the dimensions in Fig. 6.23, a backward wave transmission band in the range of 1.8 GHz is obtained. The metallizations above and below the omega particles have a width of 10 mm to assure a good RF contact between the arms of the omega resonators and the test fixture clamping areas.

With the given unit cell size, a $4 \times 1 \times 3$ unit cell array can be characterized in the presented characterization line. The unit cell and its biasing in Fig. 6.24 follow the proposal for the biasing of larger omega resonator arrays in Fig. 6.17.

For the simulation of the omega particle, the frequency domain solver in CST Microwave Studio and CST Design Studio for circuit simulation are used. As for the tunable SRR in Sect. 6.2, a fullwave simulation of the unit cell structure with a discrete port for each lumped element, i.e. varactor diode, bias resistor, and DC blocking capacitor, is carried out. In a second simulation step, these ports are loaded with measured scattering parameters of the elements in a circuit simulator. Thus, the time consuming fullwave simulation has to be performed only once when the geometry is changed, while the tuning behaviour can be investigated on circuit level.

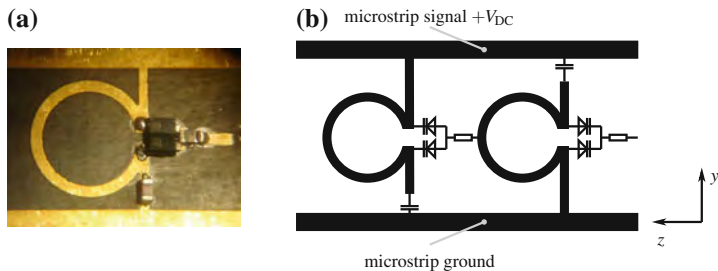


Fig. 6.24 **a** Photo of a fabricated omega resonator unit cell, **b** Biasing scheme of the omega resonators inside the characterization line

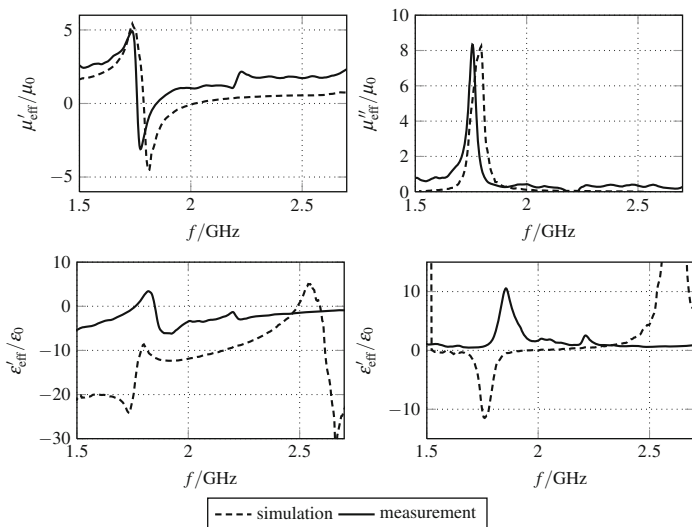


Fig. 6.25 Comparison of the simulated and measured effective material parameters of the $4 \times 1 \times 3$ array for a tuning voltage of 5 V

A comparison between the simulated and measured effective material parameters is shown in Fig. 6.25 for a tuning voltage of 5 V. The effective permeability is predicted well while the effective permittivity shows a significant discrepancy between the simulated and measured results. The main origin of this is the overlapping area between the RF ground on the substrates and the metallization of the characterization line. If both surfaces are not touching completely, gaps between them cause parasitic capacitances, which have a significant impact on the capacitance in the shunt branch of the equivalent circuit. A further source of error is the de-embedding process of the taper sections of the characterization line as described before. Since the characteristics of the manufactured taper sections are not exactly known, the caused error affects the extracted effective material parameters.

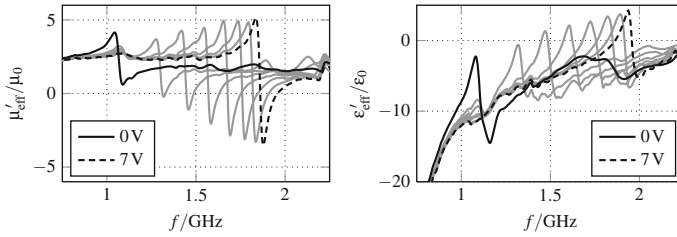


Fig. 6.26 Measured real part of effective material parameters of the $4 \times 1 \times 3$ array for different tuning voltages (intermediate tuning states in 1 V steps are plotted in gray)

The continuous tuning of the real part of the effective material parameters is demonstrated in Fig. 6.26. Due to the imperfect contact of the RF ground metallization, a parasitic resonance occurs in the effective permittivity which overlaps with the magnetic resonance so that a backward wave band cannot be observed. However, the effective permeability follows the Lorentz dispersion and the magnetic resonance frequency can be tuned between 1.1 GHz at 0 V and 1.9 GHz at 7 V as expected from the theoretical considerations.

6.4 Tunable Fishnet Structure

In the previous sections it has been demonstrated and investigated how tunability can be introduced to three-dimensional unit cells like split-ring resonators and omega resonators using biasing schemes that are suitable for the implementation of large arrays. However, the substrates containing the unit cells have to be aligned parallel to each other with a constant distance. This can be challenging for certain substrate materials such as Teflon-based laminates where the distance can vary due to the missing rigidity of the substrates, particularly since a large number of substrates is necessary transversal to the propagation direction. Apart from mechanical demands, investigations of split-ring resonators have shown a degradation and saturation of their resonance when scaled up in frequency [41].

For the fishnet structure [14, 15, 42], which shows the same dispersion characteristics as the SRR–wire combination, manufacturing challenges are less restrictive since required metallizations can be structured using standard photolithography on Teflon or glass substrates, which are then stacked normal to the incident beam. Tunability of the dispersion characteristics can be achieved by using a dielectric layer with a tunable permittivity between the RF metallizations of the fishnet. In [43, 44], LC is used as voltage tunable dielectric layer with a permittivity that is tuned uniformly over the complete array. Hereby, the uniform phase distribution over the aperture of the fishnet and its frequency response can be controlled, but beam scanning is not possible.

Fig. 6.27 Schematic view of two unit cell layer of the fishnet array

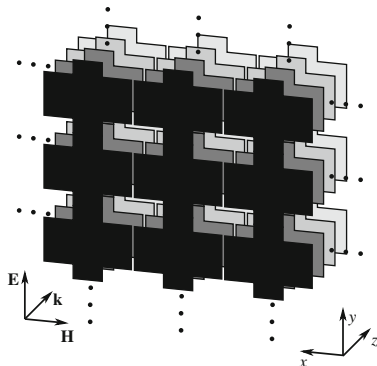
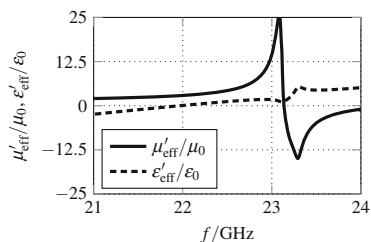


Fig. 6.28 Real part of the effective material parameters of a fishnet array



Here, an artificial gradient-index lens based on fishnet metamaterial with a locally tunable response is demonstrated. In addition to the frequency-selective response, it is possible to manipulate the phase distribution over the aperture with a tuning voltage and achieve a scanning of an incident wave.

The fishnet with the schematic view of two unit cell layers in Fig. 6.27 produces a Lorentz-Drude response for the effective material parameters [14, 15] as shown in Fig. 6.28. The effective permeability shows a Lorentz resonance at 23.1 GHz with strong spatial dispersion whereas the effective permittivity follows the Drude dispersion with a wide band of negative effective permittivity below the electric plasma frequency of 22.1 GHz. Figure 6.29 shows the surface current densities near the magnetic resonance frequency and near the electric plasma frequency, respectively. Near the magnetic resonance, the incident magnetic field induces antiparallel currents on the metallizations (Fig. 6.29a). The current loop is closed via the dielectric layer between the metallizations yielding the equivalent circuit in Fig. 6.30b. The magnetic resonance frequency is thus given by [14]

$$\omega_{0\mu}^2 = \frac{1}{C_1} \cdot \left(\frac{1}{L_1} + \frac{1}{L_2} \right) \quad (6.7)$$

and can be tuned by the capacitance C_1 , i.e. the permittivity, between the metallizations.

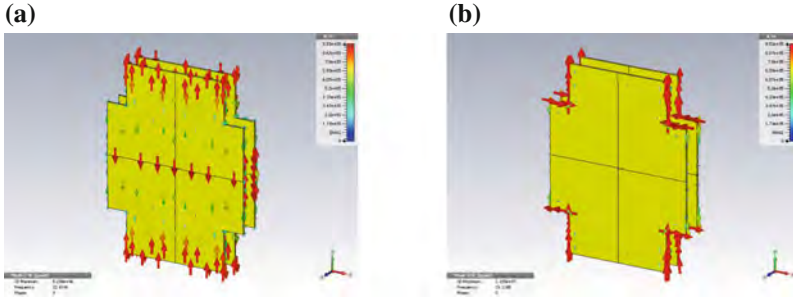


Fig. 6.29 Surface current density of the fishnet unit cell: **a** near the magnetic resonance frequency, **b** near the electric plasma frequency

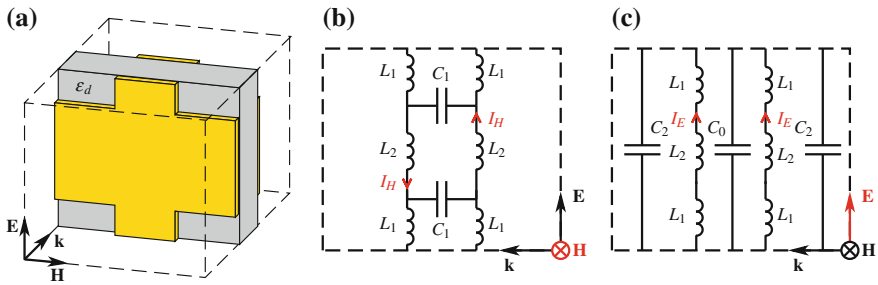


Fig. 6.30 Fishnet unit cell: **a** Three-dimensional view; **b/c**: Lumped element representation of the currents in the fishnet unit cell: **b** Excitation of antiparallel currents near the magnetic resonance frequency, **c** Excitation of parallel currents near the electric plasma frequency

Near the electric plasma frequency, the currents on the metallizations driven by the incident electric field are parallel (Fig. 6.29b). Since the distance between the metallizations is small and hence, the phase on both metallizations is approximately the same, no displacement current flows via the capacitance C_1 which yields the equivalent circuit in Fig. 6.30c. The capacitors C_0 and C_2 represent the capacitances inside the unit cell parallel to the incident electric field, i.e. the dielectric host material. Two different capacitances are used to consider different materials between the metallizations inside the unit cell and between adjacent unit cells. With this configuration, the electric plasma frequency is

$$\omega_{pe}^2 = \frac{1}{(L_1 + L_2/2)(C_0 + 2C_2)}. \quad (6.8)$$

As it can be seen from (6.7) and (6.8), the magnetic and electric response can be controlled by tuning the permittivity of the host material, i.e. the dielectric layers in the fishnet. In the implemented structure, one dielectric layer consists of tunable material whereas the other dielectric layer acts, additionally to its RF characteristic, as mechanical supporting structure containing the RF metallizations.

The magnetic resonance frequency is determined by the permittivity ε_d between the metallizations, i.e. by the capacitor C_1 . To obtain a large capacitor value and thus, a small resonance frequency and a small physical length of the unit cell, the permittivity ε_d has to be as large as possible while the distance between the metallizations has to be as small as possible. If the metallization distance is much smaller than the unit cell length, C_0 is decreased and C_2 is increased so that the electric plasma frequency can be approximated

$$\omega_{pe}^2 \approx \frac{1}{(2L_1 + L_2)C_2}. \quad (6.9)$$

Hence, for a small ratio of the dielectric layer length and unit cell length $\frac{l_d}{p} \ll 1$, a permittivity variation of the dielectric layer tunes the magnetic resonance frequency $\omega_{0\mu}$ but not the electric plasma frequency ω_{pe} .

6.4.1 Static Gradient-Index Fishnet Structure

With tunable effective material parameters it is possible to manipulate the phase of the transmitted wave of a unit cell at a fixed frequency. As shown in (6.2), the direction of the transmitted wave of an transversal array can be controlled by varying the phase shift in each unit cell, i.e. by controlling the magnetic resonance frequency or electric plasma frequency of each fishnet unit cell. Here, this principle is applied to realize a continuous voltage tunable gradient-index lens based on the fishnet metamaterial. First, investigations of the array and the phase gradient are carried out to demonstrate the beam-scanning capability of the fishnet metamaterial and its applicability as artificial gradient-index lens. In a second step, voltage tunability is introduced to each unit cell of a fishnet array to control the radiation direction of the transmitted wave.

According to Fig. 6.30 and (6.7), the magnetic resonance frequency of the fishnet depends on the permittivity ε_d of the dielectric layer between the metallizations. If their distance is much smaller than the unit cell length, a variation of the permittivity ε_d tunes the capacitor C_1 whereas the tuning of C_0 can be neglected compared to C_2 .

The spatial variation of ε_d will later be realized by using tunable material. In the current investigation it is realized with a layer of Rogers RO4003 dielectric substrate with a cavity as shown in Fig. 6.31. The effective permittivity ε_d and hence, the capacitor $C_1 \propto \varepsilon_d$, can be manipulated by the air–RO4003 ratio between the metallizations, i.e. the cavity diameter d . With the geometric parameters in Fig. 6.31, the effective material parameters as shown in Fig. 6.32 are achieved. With an increasing cavity diameter d , the value of C_1 is decreased which shifts the magnetic resonance frequency from 22.5 to 25.5 GHz. Apart from the anti-resonance caused by spatial dispersion, the effective permittivity, i.e. the electric plasma frequency of 21.8 GHz, is not tuned.

The largest tuning of the effective permeability occurs at 22.5 GHz, i.e. the lowest achievable magnetic resonance frequency. The effective material parameters at this

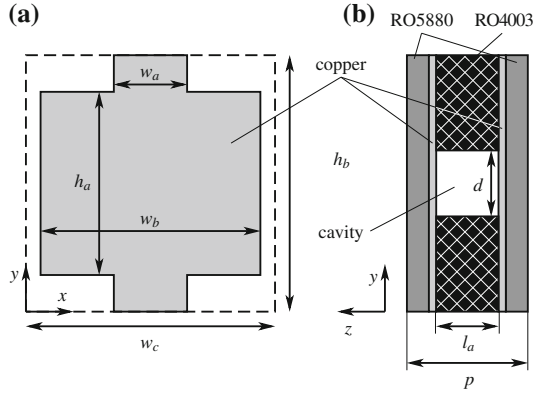


Fig. 6.31 Schematic of the fishnet unit cell: **a** Front view of the metallization, **b** side view of the substrates with the metallization and cavity for tuning the magnetic resonance frequency (dimensions in mm : $w_a = 0.4$, $w_b = 4.5$, $w_c = 5.0$, $h_a = 4.0$, $h_b = 4.5$, $l_a = 0.5$, $p = 0.754$)

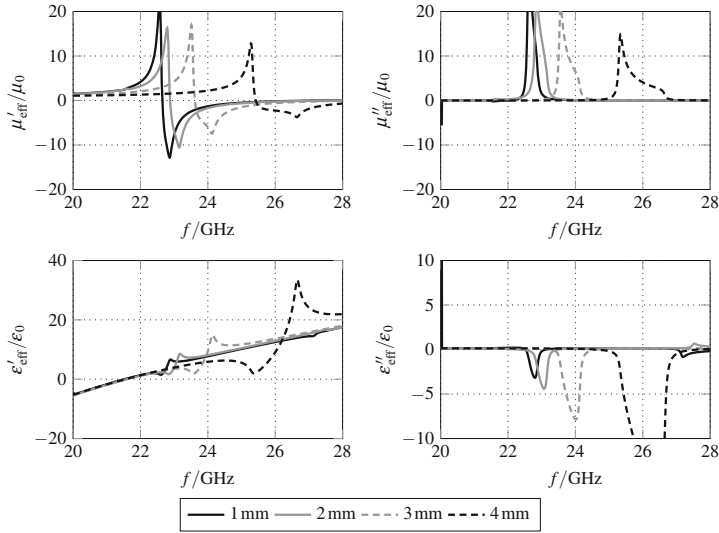


Fig. 6.32 Simulated effective material parameters for different cavity diameters

frequency for different cavity diameters are summarized in Fig. 6.33. The real part of the effective permeability is tuned between $1.5\mu_0$ and $15.3\mu_0$ whereas the effective permittivity is hardly tuned and constant around $2.5\epsilon_0$. A third-order polynomial fitting for the effective material parameters yields

$$\begin{pmatrix} \mu'_{\text{eff}}/\mu_0 \\ \mu''_{\text{eff}}/\mu_0 \\ \epsilon'_{\text{eff}}/\epsilon_0 \\ \epsilon''_{\text{eff}}/\epsilon_0 \end{pmatrix} = \begin{pmatrix} 32.947 & -22.947 & 5.8505 & -0.52083 \\ 7.5163 & -5.2527 & 1.1525 & -0.077134 \\ 1.936 & -0.25266 & 0.2935 & -0.045833 \\ 1.0396 & -1.5907 & 0.70079 & -0.090033 \end{pmatrix} \cdot \begin{pmatrix} 1 \\ d/\text{mm} \\ (d/\text{mm})^2 \\ (d/\text{mm})^3 \end{pmatrix}. \quad (6.10)$$

Fig. 6.33 Simulated effective material parameters at 22.5 GHz for different cavity diameters

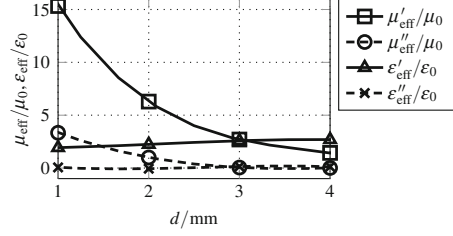
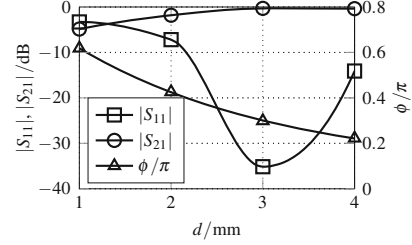


Fig. 6.34 Simulated scattering parameters and phase shift of one single unit cell layers at 22.5 GHz for different cavity diameters



With this, the cavity diameter can be calculated for a desired set of effective material parameters.

With a single unit cell layer, a variation of the cavity diameter yields the scattering parameters and phase shift ϕ at 22.5 GHz as shown in Fig. 6.34. Best matching and transmission is achieved for a cavity diameter of 3 mm. This is because for $d = 3$ mm the Bloch impedance

$$Z_B = \sqrt{\frac{\mu_{\text{eff}}}{\epsilon_{\text{eff}}}} \approx \sqrt{\frac{\mu_0}{\epsilon_0}} = \eta_0 \quad (6.11)$$

matches the free space impedance. Matching degrades for cavity diameters below 2 mm since only the effective permeability is tuned strongly and hence, matching to free space cannot be maintained for all tuning states. The phase shift follows the fitting function

$$\phi/\pi = 0.080477 + 0.84127e^{-0.4467 \frac{d}{\text{mm}}} \quad (6.12)$$

with a maximum differential unit cell phase shift of $\Delta\phi = 0.4\pi$. Hence, at least five unit cell layers in propagation direction would be necessary to obtain a differential phase shift of 2π which is essential for the implementation of a Fresnel profile.

Since during the application as tunable lens the incident or radiated wave are not always normally oriented, it is important to consider the anisotropy of the fishnet unit cell [45–48]. Figure 6.35 shows the two-dimensional lattice of the fishnet in the xz -plane. Due to the structure orientation in x -direction, the wavenumbers k_x and k_z are not equal and the phase shift experienced by the wave propagating in the lattice depends on the propagation angle θ .

By applying a periodic boundary condition with independently variable phase shifts in x - and z -direction, i.e. for varying wavenumbers k_x and k_z , and vertical

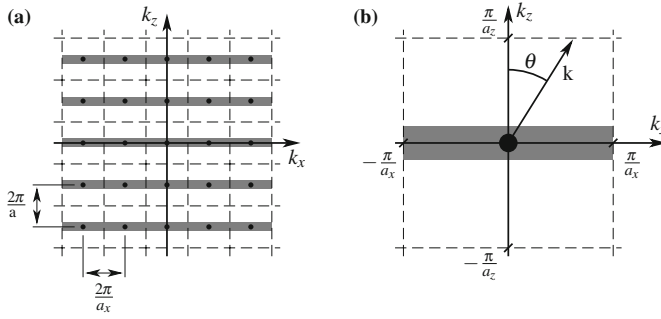


Fig. 6.35 **a** Two-dimensional lattice representation of the fishnet with the unit cell length a_z and width a_x . **b** Detail view of the fishnet unit cell with the propagation angle θ

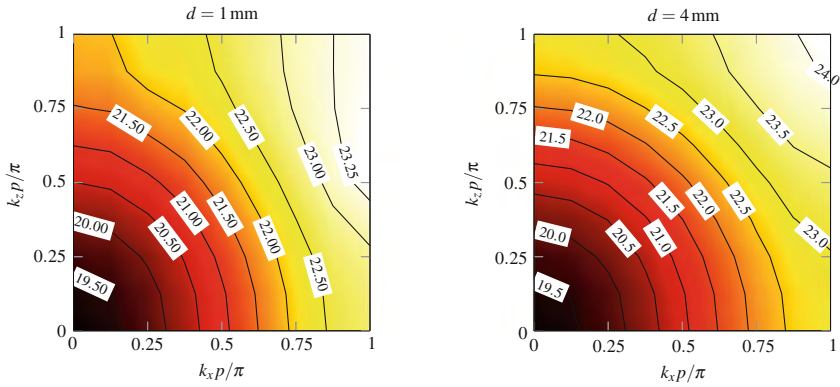


Fig. 6.36 Iso-frequency surface plot of the fishnet unit cell in the xz -plane for different cavity diameters (TE case)

polarization, the eigenfrequencies for all possible propagation directions, i.e. the two-dimensional dispersion diagram, can be computed using a fullwave eigenmode solver. This dispersion diagram represents the eigenfrequencies of propagating eigenmodes depending on the propagation directions θ .

The iso-frequency plots for a cavity diameter of 1 mm and 4 mm are presented in Fig. 6.36. Additionally, for propagation parallel to the x - and z -axis, the dispersion diagrams for $k_x(\omega)|_{k_z=0}$ and $k_z(\omega)|_{k_x=0}$ are shown in Fig. 6.37.

For a cavity diameter of 1 mm, the non-circular iso-frequency lines in Fig. 6.36 indicate an anisotropic response. Depending on the wavenumbers k_x and k_z , different cutoff frequencies are obtained. For transmission in z -direction ($k_x = 0$), a transmission band (limited by $k_z p = 0$ and $k_z p = \pi$) between 19.3 and 21.9 GHz is obtained for a cavity diameter of 1 mm (Fig. 6.37a). If the cavity diameter is increased to 4 mm, the magnetic resonance frequency is tuned and the upper cutoff frequency of the transmission band is shifted to 22.8 GHz.

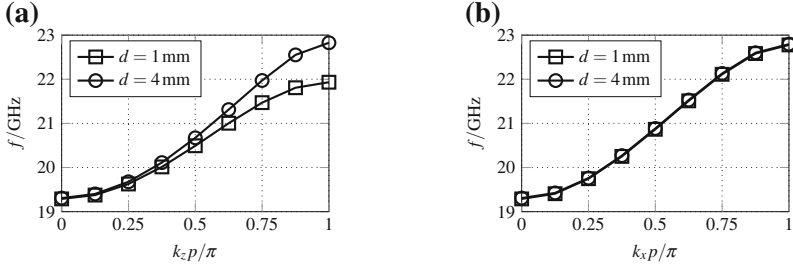


Fig. 6.37 Dispersion diagram of the fishnet unit cell for propagation parallel to the axes: **a** in z -direction ($k_x = 0$), **b** in x -direction ($k_z = 0$)

For a wave propagating in x -direction ($k_z = 0$), the transmission band between 19.3 and 22.8 GHz cannot be tuned by the cavity diameter (Fig. 6.37b). This confirms the theoretical considerations since in x -direction, a constant effective permeability and Drude dispersion for the effective permittivity are expected and variation of permittivity in the dielectric layer has a negligible impact on the electric plasma frequency.

If k_x and k_z have moderate values, i.e. for small scanning angles and for regions with small spatial dispersion, the iso-frequency lines are nearly circular with respect to the origin. Hence, $k_x \approx k_z$ and the anisotropy can be neglected.

Although the iso-frequency plots show transmission bands and propagating eigenmodes depending on frequency and propagation direction, they do not offer information about the Bloch impedance. Hence, the existence of a transmission band does not necessarily mean that the fishnet impedance matches the freespace impedance η_0 . Therefore, scattering parameter simulations for different incident angles θ , i.e. for a varying phase shift ϕ_x of the periodic boundary condition in x -direction, are carried out. The resulting transmission $|S_{21}|$ in dB is shown in Fig. 6.38 for the minimum and maximum cavity diameter. Corresponding with eigenmode results, by increasing the cavity diameter, the transmission band is shifted to higher frequencies due to the smaller permittivity between the RF metallization of the fishnet. Furthermore, the transmission depends on the incident angle θ . Transmission through the array at the operation frequency of 22.5 GHz is possible for oblique angles up to $\theta = 75^\circ$ for all tuning states. It can be observed that the transmission band, especially for a cavity diameter of 4 mm, is wider than in the eigenmode results. This is due to the coupling of higher order modes that are not considered in the scattering parameters of the single-layer.

To investigate the beam scanning properties, an array consisting of 5×5 unit cells transversal to the incident beam and 1 unit cell in propagation direction is designed. The array consists of the unit cell with the dimensions in Fig. 6.31. The cavity diameter is set to $\mathbf{d} = (4, 2.63, 1.95, 1.437, 1)$ mm as shown in Fig. 6.39. This yields a phase gradient of $\frac{\Delta\phi}{\Delta x} = 15.89 \frac{\pi}{\text{m}}$ and, according to (6.2), a radiation angle of $\psi = 6.1^\circ$. This is confirmed by the fullwave simulation result shown in Fig. 6.40.

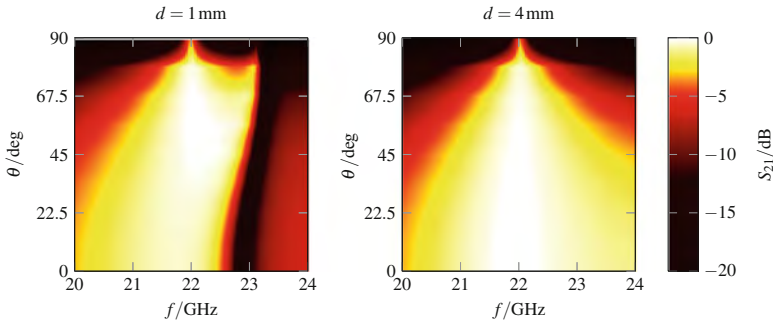


Fig. 6.38 Simulated forward transmission $|S_{21}|$ in dB of the fishnet unit cell for different propagation angles θ in the xz -plane and for different cavity diameters (TE case)

Fig. 6.39 One line of the static fishnet with varying cavity diameter

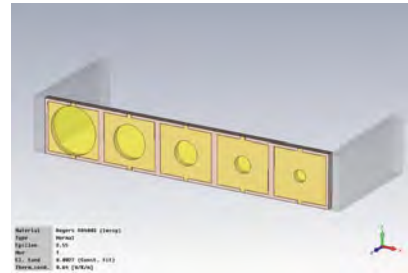
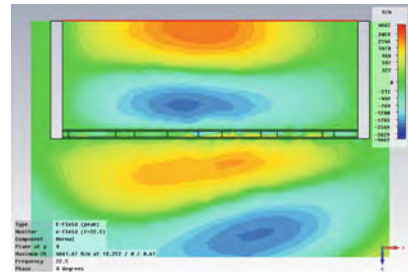


Fig. 6.40 Simulated electric near field distribution of a single layer fishnet array with a gradient cavity diameter d at 22.5 GHz



The normal incident beam is refracted due to the constant phase gradient over the array aperture.

A photo of the manufactured, opened fishnet array is shown in Fig. 6.41. Two Rogers RO5880 substrates contain the RF copper metallization with a thickness of $17 \mu\text{m}$. The middle dielectric layer contains the cavities with varying diameter to create the phase gradient over the aperture width. To obtain a high accuracy of the cavity positions and diameters, the dielectric layer is fabricated using a computer controlled milling machine. All layers are clamped together using an FR4 frame. The excitation is done with an open waveguide 10 cm behind the fishnet array and the phase gradient can be changed by replacing the middle dielectric layer.

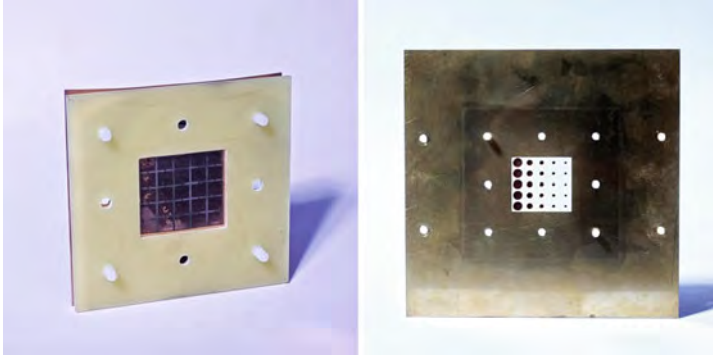
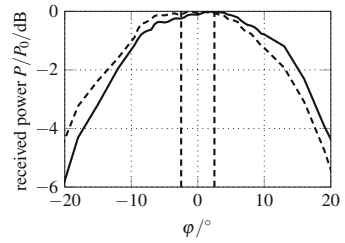


Fig. 6.41 Photos of one opened fishnet unit cell layer consisting of 5×5 transversal unit cells and varying cavity diameter

Fig. 6.42 Measured normalized far field patterns at 22.5 GHz for positive and negative phase gradient



The measured far field pattern for a positive and negative phase gradient of $\frac{\Delta\phi}{\Delta x} = \pm 15.89 \frac{\pi}{\text{m}}$ is shown in Fig. 6.42. Due to the small aperture size of the array, the half-power beam width of 30° is large compared to the beam scanning angle of $\pm 3^\circ$. The beam scanning is smaller compared to the simulation result due to boundary effects and variations of the gradient caused by fabrication tolerances. Because flexible Teflon-based substrates with a small thickness are used for the outer dielectric layers containing the RF metallizations, the distance between them shows variations over the aperture which results in a non-constant phase gradient.

According to (6.2), to increase the beam scanning angle, the phase gradient $\frac{\Delta\phi}{\Delta x}$ has to be increased by either increasing the differential phase or by decreasing the aperture size. However, a reduced aperture size yields an even larger half-power beam width so that the more convenient approach is to increase the differential phase shift by increasing the number of unit cell layers in propagation direction.

6.4.2 Voltage Tunable Gradient-Index Fishnet Structure

As demonstrated in the above section and in [49], the fishnet structure can be exploited for the design of gradient-index metamaterials by varying the permittivity of the dielectric layer. However, for many applications tunability of the dispersion characteristics and hence, of the phase gradient, is desired, e.g. to operate at multiple frequencies or to change the phase shift at a certain frequency. Liquid crystals (see Sect. 5.2) with their suitable properties concerning tunability and losses for frequencies above 10 GHz have been employed to design tunable devices in the terahertz regime [50–52], e.g. by using temperature tuning of the LC permittivity.

The static gradient-index fishnet from the previous section is modified. The non-uniform dielectric layer is replaced by a layer of liquid crystal material to implement voltage tunability and to control the phase distribution over the aperture.

For this proof-of-concept prototype, a relatively small array with 8×8 transversal unit cells and 2 unit cell layers in propagation direction is designed. This is a compromise in terms of achievable beam scanning range, half-power beam width, size limitation for fabrication, and amount of necessary LC material.

In Fig. 6.43, the proposed voltage tunable fishnet unit cell and its dimensions are presented. The Rogers RO4003-substrate layers contain the RF metallization of the fishnet unit cell. They are separated by a layer of LC with a voltage tunable permittivity. Since all unit cells are connected in vertical direction, a tuning voltage can be applied between two metallic layers of each column in the array. Thus, no additional biasing network is necessary and parasitic effects are minimized. Furthermore, technological demands are drastically reduced compared to solutions with a dedicated resistive or inductive biasing network.

To investigate the dispersion properties and their tuning, fullwave simulations of the fishnet unit cell including all metallic and dielectric losses are carried out in CST

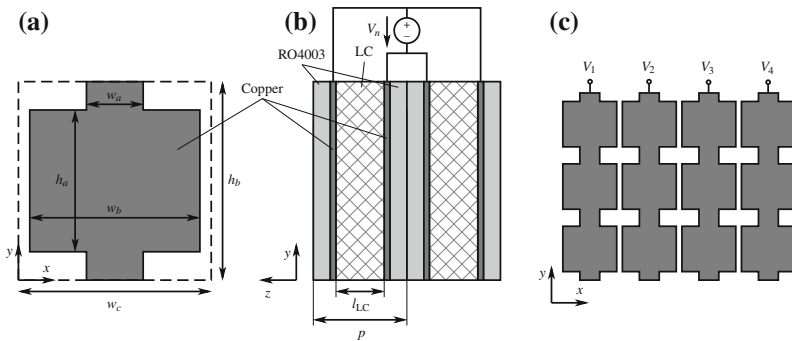


Fig. 6.43 Schematic view of the fishnet unit cell. **a** Front view of the unit cell metallization, **b** side view of two unit cell layers consisting of the substrates and liquid crystal layer (dimensions in mm: $w_a = 1$, $w_b = 4.5$, $w_c = 4.7$, $h_a = 3$, $h_b = 4.5$, $l_{LC} = 0.762$, $p = 3l_{LC}$), **c** front view of the array metallization with applied tuning voltages

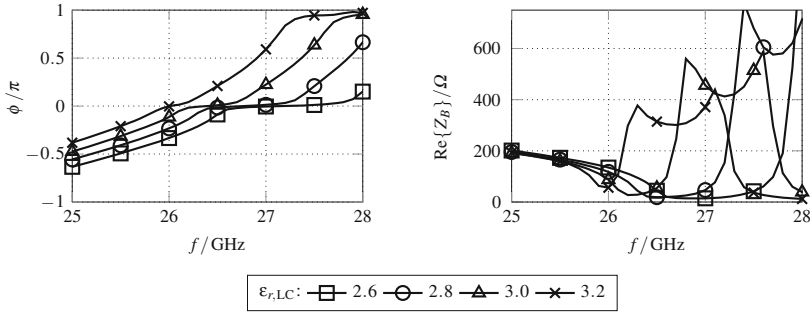
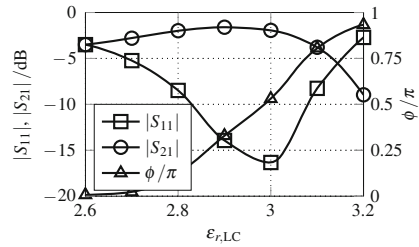


Fig. 6.44 Simulated phase shift and realpart of the Bloch impedance of two fishnet unit cell layers for different LC permittivities

Fig. 6.45 Simulated scattering parameters and phase shift of two unit cell layers at 27.4 GHz for different LC permittivities



Microwave Studio using plane wave excitation at the input and output plane. The extracted phase shift and real part of the Bloch impedance of two unit cell layers for different tuning states, i.e. for different permittivities of the LC layer, are shown in Fig. 6.44. A backward and forward wave transmission band are separated by a stop band with tunable cutoff frequencies. This yields a maximum phase tuning close to 1π above 27.4 GHz. By stacking five unit cell layers, a differential phase shift of more than 2π can be obtained which is necessary to achieve arbitrary phase gradients (6.3) and a beam scanning range that is not limited by the aperture size.

The extracted phase shift and the scattering parameters of two unit cell layers are shown in Fig. 6.45 for different LC permittivities at a frequency of 27.4 GHz. The transmission for two unit cell layers is better than -5 dB for LC permittivities between 2.6 and 3.1 and decreases for high permittivities. Due to the dispersive response of the unit cell, the Bloch impedance is not constant and thus, matching is not possible for all tuning states. The mismatch, caused by the decreased Bloch impedance, can be neglected for the presented application since it only occurs for the boundary unit cell elements with the maximum LC permittivity. However, improvement of the matching would be possible by optimizing the unit cell dimensions with compromises in the phase tuning response.

With the investigated unit cell, a fishnet consisting of two unit cell layers in propagation direction and 8×8 unit cells in the aperture plane is designed. Taking the simulated phase shift of two unit cell layers and (6.2), the maximum radiation

Fig. 6.46 Maximum radiation angle for the maximum phase gradient over the array aperture consisting of 8 transversal unit cell elements

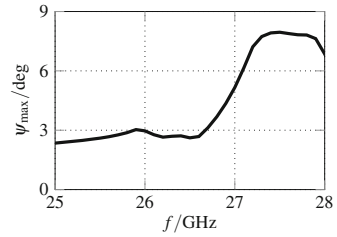
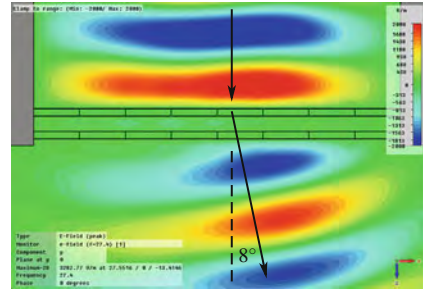


Fig. 6.47 Simulated electric near field distribution of the two-layer fishnet array with maximum gradient of the LC permittivity at 27.4 GHz [16], © 2014 IEEE



angle for this configuration can be calculated which is shown in Fig. 6.46 over the frequency of the incident wave. The relative permittivity of the LC layer is increased from 2.6 to 3.2 in x -direction, yielding a positive gradient in the phase distribution at the output plane of the fishnet array and hence, a tilt of the radiated beam. According to (6.2), beam scanning is symmetric with the normal direction in the xz -plane. With a decreasing LC permittivity from 3.2 to 2.6 in x -direction, the sign of the phase gradient and hence, the sign of the maximum radiation angle, changes while the magnitude is unaffected. The maximum beam scanning of $\pm 8^\circ$ is achieved at 27.4 GHz, which is confirmed by the fullwave simulation of the array as shown in Fig. 6.47. In the electric nearfield distribution it can be seen that the incident beam is refracted by $\psi = 8^\circ$ with respect to the normal direction of the fishnet.

Figure 6.48 shows a photo of the fabricated substrate layers that are used to build one unit cell layer of the fishnet. Each column of the fishnet is connected to a separate biasing pad, allowing independent tuning of each column of unit cells in the array. Two substrates carry the RF metallizations with the fishnet structure. Another RO4003 substrate with a thickness of 0.762 mm is used as spacer. It contains a cavity for the LC, and filling channels for the injection of the LC in the cavity. The final fishnet prototype consists of two of these unit cells in propagation direction. Due to the employment of RO4003 substrates with drilled holes, bolts can be used for precise alignment of the different layers and at the same time they apply the necessary force to seal the cavity against leakage of LC. With this approach it is easily possible to adjust the number of unit cell layers without any adaption of the design.

A photo of the complete fishnet including the DC connector for the tuning voltages and an open waveguide excitation is shown in Fig. 6.49.

Fig. 6.48 Photo of one opened voltage tunable fishnet unit cell layer

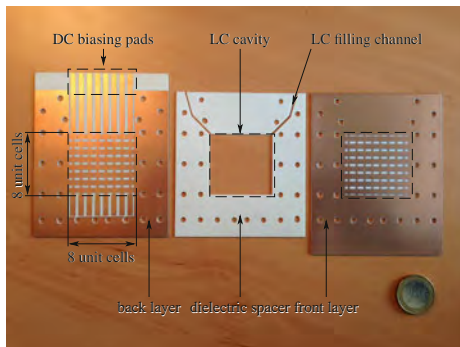


Fig. 6.49 Photo of the finished fishnet with DC connector for the tuning voltages and open waveguide excitation

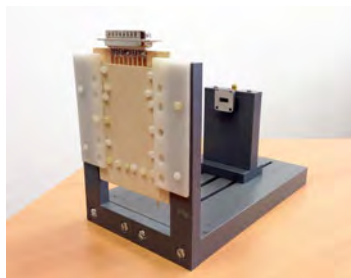
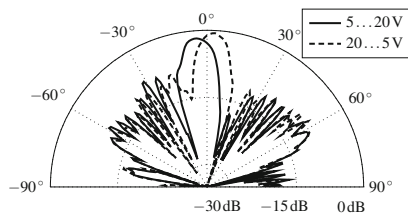
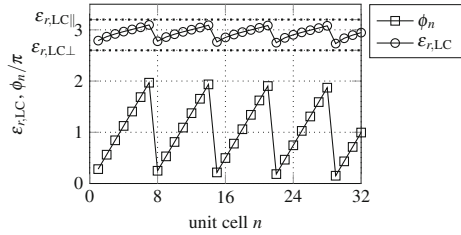


Fig. 6.50 Measured normalized far field patterns at 27.5 GHz for two tuning states [16], © 2014 IEEE



The measured normalized far field pattern at 27.5 GHz for two tuning states $V_{DC} = (5 \text{ V} \dots 20 \text{ V})$ and $V_{DC} = (20 \text{ V} \dots 5 \text{ V})$ is shown in Fig. 6.50. The maximum achieved measured scan angle of $\pm 5^\circ$ is smaller than predicted by the fullwave simulation. This is due to the fact that the phase shift ϕ_n is not linearly connected to the tuning voltage. Hence, although V_{DC} is changed linearly, the phase distribution over the array width is not linear. By measuring the phase shift depending on the tuning voltage, e.g. with a near field measurement setup, the connection between ϕ_n and the tuning voltage can be found. With that relation, a linear phase distribution over the array aperture can be adjusted, yielding a larger beam scanning range close to the simulated value.

Fig. 6.51 Phase and LC permittivity distribution for an array width of 32 unit cells and a radiation angle of 20° at 27.4 GHz



Concluding from the phase tuning range in Fig. 6.45, with five unit cell layers in propagation direction the possible phase tuning $\Delta\phi$ becomes larger than 2π and by exploiting the phase periodicity, the aperture size does not limit the maximum beam scanning angle. A Fresnel lens profile with the phase gradient (6.3) can be introduced over the fishnet aperture yielding a maximum beam scanning range of $\pm 90^\circ$. As an example, such a phase profile applied is to a $32 \times 32 \times 5$ fishnet array. It consists of the unit cell geometry depicted in 6.48. For a radiation angle of 20° , the phase profile according to (6.3) and the required LC permittivity in each unit cell column is shown in Fig. 6.51. The permittivity in each column is within the material tuning range of the employed LC. Hence, the phase is increased linearly over the aperture and is wrapped at multiples of 2π .

The simulated electric field distribution of this array configuration with a Fresnel phase profile is presented in Fig. 6.52. The normal incident beam is refracted by 20° . Due to the increased aperture size, the approximation of a plane wavefront is better than for the small array consisting of 8×8 unit cells.

Since each unit cell column can be addressed independently, arbitrary phase profiles can be realized as well. That way, not only beam scanning, but also beam forming is possible, e.g. to create gradient-index lenses or transmit arrays with a tunable effective concave or convex shape to focus an incident in one point. Furthermore, the phase distribution can be varied to adaptively optimize the shape of the transmitted

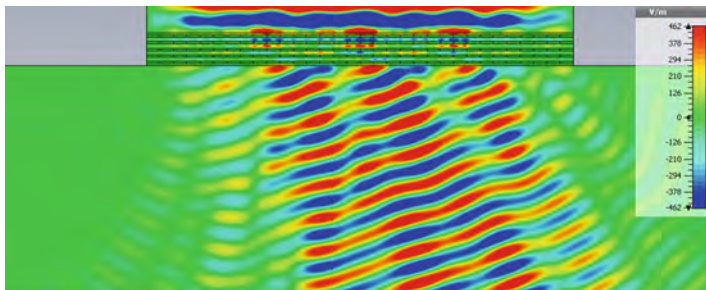


Fig. 6.52 Simulated electric near field distribution of the five-layer fishnet array with a Fresnel profile at 27.4 GHz

wave for a desired application, e.g. for multiple beam patterns or to optimize the pattern of different excitation sources.

References

1. D.R. Smith, J.J. Mock, A.F. Starr, D. Schurig, Gradient index metamaterials. *Phys. Rev. E* **71**, 036609 (2005)
2. R. Liu, X.M. Yang, J.G. Gollub, J.J. Mock, T.J. Cui, D.R. Smith, Gradient index circuit by waveguided metamaterials, **94**(7), 073506 (2009)
3. H. Ma, X. Chen, X. Yang, H. Xu, Q. Cheng, T. Cui, A broadband metamaterial cylindrical lens antenna. *Chin. Sci. Bull.* **55**(19), 2066–2070 (2010)
4. C. Pfeiffer, A. Grbic, Metamaterial huygens' surfaces: Tailoring wave fronts with reflectionless sheets. *Phys. Rev. Lett.* **110**(19), 197401 (2013)
5. N.I. Landy, S. Sajuyigbe, J.J. Mock, D.R. Smith, W.J. Padilla, Perfect metamaterial absorber. *Phys. Rev. Lett.* **100**, 207402 (2008)
6. D. Schurig, J.J. Mock, B.J. Justice, S.A. Cummer, J.B. Pendry, A.F. Starr, D.R. Smith, Metamaterial electromagnetic cloak at microwave frequencies. *Science* **314**(5801), 977–980 (2006)
7. R. Liu, C. Ji, J.J. Mock, J.Y. Chin, T.J. Cui, D.R. Smith, Broadband ground-plane cloak. *Science* **323**(5912), 366–369 (2009)
8. J. Pendry, A. Holden, D. Robbins, W. Stewart, Magnetism from conductors and enhanced nonlinear phenomena. *IEEE Trans. Microw. Theory Tech.* **47**, 2075–2084 (1999)
9. J.B. Pendry, A.J. Holden, D.J. Robbins, W.J. Stewart, Low frequency plasmons in thin-wire structures. *J. Phys. Condens. Matter* **10**(22), 4785 (1998)
10. M.M.I. Saadoun, N. Engheta, A reciprocal phase shifter using novel pseudochiral or ω medium. *Microw. Opt. Technol. Lett.* **5**(4), 184–188 (1992)
11. C.R. Simovski, S. He, Frequency range and explicit expressions for negative permittivity and permeability for an isotropic medium formed by a lattice of perfectly conducting ω particles. *Phys. Lett. A* **311**(2–3), 254–263 (2003)
12. H. Chen, L. Ran, J. Huangfu, X. Zhang, K. Chen, T.M. Grzegorzczuk, J.A. Kong, Left-handed materials composed of only S-shaped resonators. *Phys. Rev. E* **70**, (2004)
13. H. Chen, L.-X. Ran, J.T. Huang-Fu, X.-M. Zhang, K.S. Chen, T.M. Grzegorzczuk, J.A. Kong, Magnetic properties of s-shaped split-ring resonators. *Progr. Electromag. Res.* **51**, 231–247 (2005)
14. M. Kafesaki, I. Tsiapa, N. Katsarakis, T. Koschny, C.M. Soukoulis, E.N. Economou, Left-handed metamaterials: The fishnet structure and its variations. *Phys. Rev. B* **75**, (Jun 2007)
15. V.M. Shalaev, W. Cai, U.K. Chettiar, H.-K. Yuan, A.K. Sarychev, V.P. Drachev, A.V. Kildishev, Negative index of refraction in optical metamaterials. *Opt. Lett.* **30**, (December, 2005)
16. M. Maasch, M. Roig, C. Damm, R. Jakoby, Voltage-tunable artificial gradient-index lens based on a liquid crystal loaded fishnet metamaterial. *IEEE Antennas Wirel. Propag. Lett.* **13**, 1581–1584 (2014)
17. D. Black, J.C. Wiltse, Millimeter-wave characteristics of phase-correcting fresnel zone plates. *IEEE Trans. Microw. Theory Tech.* **35**, 1122–1129 (1987)
18. L. Baggen, M. Herben, Design procedure for a fresnel-zone plate antenna. *Int. J. Infrared Millim. Waves* **14**(6), 1341–1352 (1993)
19. A. Petosa, A. Ittipiboon, Design and performance of a perforated dielectric fresnel lens. *IEE Proc. Microw. Antennas Propag.* **150**(5), 309–314 (2003)
20. I. Gil, J. García-García, J. Bonache, F. Martín, M. Sorolla, R. Marqués, Varactor-loaded split ring resonators for tunable notch filters at microwave frequencies. *Electr. Lett.* **40**, 1347–1348 (2004)

21. M. Gil, C. Damm, M. Sazegar, M. Maasch, A. Giere, M. Schüßler, F. Aznar, A. Velez, J. Bonache, R. Jakoby, F. Martín, Tunable sub-wavelength resonators based on barium-strontium-titanate thick-film technology, *IET Microw. Antennas Propag.*, **5**, 316–323 (February, 2011)
22. I.V. Shadrivov, S.K. Morrison, Y.S. Kivshar, Tunable split-ring resonators for nonlinear negative-index metamaterials. *Opt. Express* **14**(20), 9344–9349 (2006)
23. T.H. Hand, S.A. Cummer, Frequency tunable electromagnetic metamaterial using ferroelectric loaded split rings. *J. Appl. Phys.* **103**, 066105 (March, 2008)
24. I. Gil, J. Bonache, J. García-García, F. Martín, Tunable metamaterial transmission lines based on varactor-loaded split-ring resonators. *IEEE Trans. Microw. Theory Tech.* **54**, 2665–2674 (June, 2006)
25. K. Aydin, E. Ozbay, Capacitor-loaded split ring resonators as tunable metamaterial components. *J. Appl. Phys.* **101**(2), 024911 (2007)
26. M. Bayindir, K. Aydin, E. Ozbay, P. Markoš, C.M. Soukoulis, Transmission properties of composite metamaterials in free space. *Appl. Phys. Lett.* **81**(1), 120–122 (2002)
27. G. Lubkowski, C. Damm, B. Bandlow, R. Schuhmann, M. Schüßler, T. Weiland, Waveguide miniaturization using spiral resonators and dipole arrays, in *Proceedings of the 36th European Microwave Conference* (2006), pp. 1312–1315
28. G. Lubkowski, R. Schuhmann, T. Weiland, Extraction of effective metamaterial parameters by parameter fitting of dispersive models. *Microw. Opt. Technol. Lett.* **49**(2), 285–288 (2007)
29. G. Lubkowski, C. Damm, B. Bandlow, R. Schuhmann, M. Schüßler, T. Weiland, Experimental study of subwavelength waveguides loaded by electric and magnetic resonant scatterer arrays, in *Proceedings of the 38th European Microwave Conference* (2008), pp. 1050–1053
30. K. Nicholson, W. Rowe, K. Ghorbani, Design and demonstration of a metamaterial with electronically tunable negative refraction across the c microwave band. *IET Microw. Antennas Propag.* **5**(6), 631–636 (2011)
31. K. Nicholson, W. Rowe, P. Callus, K. Ghorbani, Split-ring resonator loading for the slotted waveguide antenna stiffened structure. *IEEE Antennas Wirel. Propag. Lett.* **10**, 1524–1527 (2011)
32. R. Marqués, J. Martel, F. Mesa, F. Medina, Left-handed-media simulation and transmission of em waves in subwavelength split-ring-resonator-loaded metallic waveguides. *Phys. Rev. Lett.* **89**, 183901 (2002)
33. S. Hrabar, J. Bartolic, Backward-wave waveguide based on uniaxial anisotropic negative permeability meta-material, in *17th International Conference on Applied Electromagnetics and Communications, 2003, ICECom 2003* (October, 2003), pp. 251–254
34. N. Engheta, R. Ziolkowski, *Metamaterials: Physics and Engineering Explorations* (Wiley, New Jersey, 2006)
35. C.R. Simovski, Plane-wave reflection and transmission by grids of conducting ω -particles and dispersion of ω electromagnetic crystals. *AEU Int. J. Electr. Commun.* **57**(5), 358–364 (2003)
36. J. Huangfu, L. Ran, H. Chen, X.-M. Zhang, K. Chen, T.M. Grzegorzczuk, J.A. Kong, Experimental confirmation of negative refractive index of a metamaterial composed of ω -like metallic patterns. *Appl. Phys. Lett.* **84**(9), 1537–1539 (2004)
37. E. Lheurette, O. Vanbesien, D. Lippens, Double negative media using interconnected omega-type metallic particles. *Microw. Opt. Technol. Lett.* **49**(1), 84–90 (2007)
38. F. Zhang, S. Potet, J. Carbonell, E. Lheurette, O. Vanbesien, X. Zhao, D. Lippens, Application of omega-type and related metamaterials for beam steering in x-ku, in *Proceedings of the European Microwave Conference* (2007), pp. 909–912
39. F. Zhang, G. Houzet, E. Lheurette, D. Lippens, M. Chaubet, X. Zhao, Negative-zero-positive metamaterial with omega-type metal inclusions. *J. Appl. Phys.* **103**(8), 084312 (2008)
40. F. Zhang, L. Kang, Q. Zhao, J. Zhou, X. Zhao, D. Lippens, Magnetically tunable left handed metamaterials by liquid crystal orientation. *Opt. Express* **17**, 4360–4366 (2009)
41. J. Zhou, T. Koschny, M. Kafesaki, E.N. Economou, J.B. Pendry, C.M. Soukoulis, Saturation of the magnetic response of split-ring resonators at optical frequencies. *Phys. Rev. Lett.* **95**, 223902 (2005)

42. R.S. Penciu, M. Kafesaki, T. Koschny, E.N. Economou, C.M. Soukoulis, Magnetic response of nanoscale left-handed metamaterials, *Phys. Rev. B*, **81**, 235111 (June, 2010)
43. F. Zhang, Q. Zhao, W. Zhang, J. Sun, J. Zhou, D. Lippens, Voltage tunable short wire-pair type of metamaterial infiltrated by nematic liquid crystal. *Appl. Phys. Lett.* **97**(13) (2010)
44. F. Zhang, W. Zhang, Q. Zhao, J. Sun, K. Qiu, J. Zhou, D. Lippens, Electrically controllable fishnet metamaterial based on nematic liquid crystal. *Opt. Express* **19** (January, 2011)
45. T.M. Grzegorzczak, M. Nikku, X. Chen, B.-I. Wu, J.A. Kong, Refraction laws for anisotropic media and their application to left-handed metamaterials. *IEEE Trans. Microw. Theory Tech.* **53**(4), 1443–1450 (2005)
46. A. Fang, T. Koschny, C.M. Soukoulis, Optical anisotropic metamaterials: Negative refraction and focusing. *Phys. Rev. B* **79**(24), 245127 (2009)
47. L. Jelinek, R. Marqués, J. Machac, Fishnet metamaterials—rules for refraction and limits of homogenization. *Opt. Express* **18**, 17940–17949 (2010)
48. S.S. Kruk, D.A. Powell, A. Minovich, D.N. Neshev, Y.S. Kivshar, Spatial dispersion of multi-layer fishnet metamaterials. *Opt. Express* **20**(14), 15100–15105 (2012)
49. M. Maasch, O. Karabey, C. Damm, M. Roig, R. Jakoby, Investigation on the beam-scanning capability of a gradient index fishnet structure, in *2012 IEEE Antennas and Propagation Society International Symposium (APSURSI)* (July, 2012), pp. 1–2
50. I.C. Khoo, D.H. Werner, X. Liang, A. Diaz, B. Weiner, Nanosphere dispersed liquid crystals for tunable negative-zero-positive index of refraction in the optical and terahertz regimes. *Opt. Lett.* **31**, 2592–2594 (2006)
51. S. Xiao, U.K. Chettiar, A.V. Kildishev, V. Drachev, I.C. Khoo, V. M. Shalaev, Tunable magnetic response of metamaterials. *Appl. Phys. Lett.* **95**(3), 033115 (2009)
52. A. Minovich, D.N. Neshev, D.A. Powell, I.V. Shadrivov, Y.S. Kivshar, Tunable fishnet metamaterials infiltrated by liquid crystals. *Appl. Phys. Lett.* **96**(19), 193103 (2010)

Chapter 7

Conclusion and Outlook

Voltage tunable metamaterials for microwave frequencies have been investigated, designed, and manufactured within this work. The concept of metamaterials, where the electromagnetic response of sub-wavelength unit cells, which are arranged in periodic lattices, is described by effective material parameters, has been applied to design different planar and three-dimensional unit cell configurations considering their realizability and technological constraints. Based on the presented approaches, metamaterials with independently voltage tunable electric and magnetic properties can be designed.

A major part of the presented work has been focused on the description of periodic structures in terms of dispersion parameters and transmission line models. This allows a description of lattices consisting of complex sub-wavelength geometries with dispersion parameters such as effective material parameters or transmission line parameters known from conventional materials. However, due to the particle size, which cannot generally be neglected, spatial dispersion has to be taken into account. This discretization effect on effective material parameters and transmission line parameters has been derived. Furthermore, it has been demonstrated that, although the transmission line model of a unit cell can consist of any combination of resistive and reactive elements, only a subset of possible combinations is physically realizable. Based on causality and passivity conditions, a general frequency response of material parameters has been derived. These conditions have been transformed into the transmission line representation yielding a general model of physically realizable unit cell configurations. Due to the equivalence between effective material parameters and transmission line parameters, these considerations are valid for one-dimensional artificial transmission lines as well as for two- and three-dimensional periodic arrays. Hence, concepts such as transmission line transformation, or electric and magnetic response described by material parameters can be utilized, yielding an abstract representation of the unit cell independent of its actual physical implementation. Consequently, at the beginning of a design process, theoretical considerations can be done by means of dispersion analysis and dispersion engineering. Thereafter, the actual geometry to implement the required dispersion is determined.

The relation between dispersion parameters and the implementation of a unit cell is an important factor in the design process. Hence, different methods to extract effective material parameters from existing unit cells have been compared. Methods that are based on the evaluation of scattering parameters can be employed to determine dispersion parameters of manufactured and measured structures. Additionally, methods like scattering parameter simulations with multiple modes or field averaging methods, that have been extended within this work, can be used to obtain dispersion properties from fullwave simulations. Due to computational constraints and the sub-wavelength size of unit cells with a high level of geometrical detail, full-wave simulations of complex arrays are time consuming or even not possible so that simulations commonly are performed for a single unit cell. The resulting dispersion parameters are used to approximately predict the response of the array. However, it has been demonstrated that with eigenmode methods and higher order scattering parameters, simulations can be performed on the basis of a single unit cell without losing accuracy compared to simulations of large arrays. Hence, the computational effort for periodic structures can be significantly reduced.

A method to predict farfield radiation patterns of large periodic antennas like leaky-wave antennas or gradient-index metamaterials has been developed within this work. The method is based on the evaluation of propagating eigenmodes by means of fullwave eigenmode simulation of a single unit cell. Compared to conventional methods, where an assumption of the field distribution of a unit cell has to be made, the developed method shows a higher accuracy since it considers higher order mode coupling between adjacent unit cells and the actual electric and magnetic field distribution of the unit cell. Furthermore, the evaluation of eigenmodes and the corresponding field distribution is performed for a single unit cell so that the simulation effort is reduced drastically.

Based on the presented theoretical foundations and methods, different planar and three-dimensional metamaterials with voltage tunable properties have been designed. Realizability of the unit cell has been an important factor in the design process of all configurations. A general objective has been the application of the presented unit cells for complex artificial transmission lines and two- and three-dimensional configurations yielding strict requirements for the unit cell, especially in terms of the biasing network and its complexity. Considering this aspect, several planar transmission line metamaterials with tunable dispersion properties have been designed for different microwave frequency bands up to 30 GHz. A double series transmission line has been designed for 2.4 GHz. It exhibits a transmission band, which can be configured to exhibit positive or negative phase velocity. It has been demonstrated that by voltage tuning it is possible to change the sign of phase velocity as well as the cutoff frequencies of the transmission band. Furthermore, artificial transmission lines, which use liquid crystals as voltage tunable dielectric, have been realized for frequencies of 16 and 30 GHz. The unit cells are based on open split-ring resonators and the double series unit cell configuration. With a prototype at 30 GHz, the impact of the biasing network on the frequency response has been investigated and

independent voltage tuning of the electric and magnetic response has been demonstrated. Potential applications include continuously voltage tunable filters, phase shifters, leaky-wave antennas, or matching networks based on artificial transmission lines. Due to the employment of discrete, concentrated circuit elements, these artificial lines yield a size reduction compared to conventional transmission line structures. Despite the use of lumped elements, parameters such as propagation constant and characteristic impedance known from transmission line theory, and concepts based on the transmission line transformation, can be utilized in the design process.

Finally, three-dimensional unit cell configurations based on split-ring resonators, omega resonators, and fishnet metamaterials have been investigated and voltage tunability has been introduced. Arrays of split-ring resonators and omega resonators have been loaded with varactor diodes to tune their magnetic response for microwave frequencies between 1 and 3 GHz. Due to the biasing network that is mainly integrated within the RF structure, it is possible to reduce parasitic effects introduced by the DC voltage distribution network. Hence, three-dimensional metamaterials with tunable properties can be realized where the impact of the biasing network merely influences the RF response. An application of such three-dimensional metamaterial configurations is the gradient-index fishnet structure that has been developed and implemented in this work. By employing liquid crystal material as dielectric layer in a fishnet metamaterial, the magnetic RF response and hence, the phase response can be locally controlled by a tuning voltage of up to 20 V and beam scanning of an incident wave can be obtained. This has been experimentally demonstrated with a proof-of-concept prototype that consists of 5×5 transversal unit cells at a frequency of 27.4 GHz yielding a beam scanning range of $\pm 5^\circ$. This scanning angle is limited by the array size of the manufactured prototype. However, theoretical analysis and fullwave simulations have shown that the general concept of artificial gradient-index lenses as well as the gradient-index fishnet can be applied for larger arrays, where by applying a Fresnel profile, arbitrary scanning angles can be achieved. Additionally, by applying a non-constant phase gradient, further transformations like beam focusing or defocusing, or beam forming are possible. Both, the fishnet structure and liquid crystals, are usable for frequencies up to the optics regime. Hence, the presented concepts and results for voltage tunable components are a promising approach for implementations in the mm- and THz-range. A further field of study is the implementation of a fishnet metamaterial with a polarization independent unit cell where, by introducing a tuning voltage matrix similar to LC displays, each unit cell can be addressed independently enabling beam scanning in the complete half-space behind the artificial lens. Moreover, a modification of the unit cell could enable voltage control of the magnetic and electric response independently of each other. Hence, not only the phase distribution, but also the impedance distribution over the aperture could be controlled so that reconfigurable lenses with perfect matching could be realized. Potential applications of such tunable three-dimensional metamaterials include beam steering and beam forming for imaging or communication systems for the mm- and THz-regime. Furthermore, the application of the fishnet as continuously

tunable frequency selective surface is possible even with a small longitudinal number of unit cell layers. Using transformation optics, i.e. the relation between trajectories of waves and the spatial variation of material parameters, complex transformations of an incident wave are possible and the realization of components beyond artificial gradient-index lenses, e.g. components with tunable properties for cloaking and field concentration, are conceivable.

Appendix

A.1 Kramers–Kronig Relation for Wavenumber

Assuming that the magnetic and electric susceptibility

$$\chi_m(\omega) = \chi_m(\omega)' - j\chi_m''(\omega), \quad (\text{A.1})$$

$$\chi_e(\omega) = \chi_e(\omega)' - j\chi_e''(\omega) \quad (\text{A.2})$$

describe the causal response to a magnetic and electric field in the frequency domain, then $\chi'(\omega)$ and $\chi''(\omega)$ is an even and odd function, respectively, so that

$$\chi_m(-\omega) = \chi_m(\omega)^*, \quad \chi_e(-\omega) = \chi_e(\omega)^*. \quad (\text{A.3})$$

With the susceptibilities, the square of the wavenumber is

$$k^2(\omega) = k_0(\omega)^2 [1 + \chi_m(\omega)][1 + \chi_e(\omega)] \quad (\text{A.4})$$

and hence,

$$\frac{k^2(\omega)}{k_0^2(\omega)} = 1 + \chi_m' + \chi_e' + \chi_m'\chi_e' - \chi_m''\chi_e'' - j(\chi_m'' + \chi_e'' + \chi_m'\chi_e'' + \chi_m''\chi_e'). \quad (\text{A.5})$$

The product of two even functions (two real parts) and the product of two odd functions (two imaginary parts) yields an even function while the product of an odd and an even function (product of a real and imaginary part) yields an odd function. Hence, with (A.3), the real part in (A.5) is an even function and the imaginary part an odd function and it shows the same symmetry

$$\frac{k^2(\omega)}{k_0^2(\omega)} = \left(\frac{k^2(-\omega)}{k_0^2(-\omega)} \right)^*. \quad (\text{A.6})$$

Since (A.3) and (A.6) are a consequence of Titchmarsh's theorem [1, 2], it has to hold

$$\frac{k^2(\omega)}{k_0^2(\omega)} = 1 - \frac{j}{\pi} \oint_{-\infty}^{\infty} \frac{k^2(\Omega)/k_0^2(\Omega)}{\omega - \Omega} d\Omega. \quad (\text{A.7})$$

With the approximation

$$\sqrt{1+a} \approx 1 + \frac{a}{2} \quad \text{for } |a| \ll 1, \quad (\text{A.8})$$

the wavenumber for small susceptibilities can be approximated by

$$k(\omega) \approx k_0(\omega) \left[1 + \frac{\chi_m(\omega)}{2} \right] \left[1 + \frac{\chi_e(\omega)}{2} \right] \quad (\text{A.9})$$

which yields

$$\frac{k^2(\omega)}{k_0^2(\omega)} \approx 1 + \frac{\chi'_m}{2} + \frac{\chi'_e}{2} + \frac{\chi'_m \chi'_e}{4} - \frac{\chi''_m \chi''_e}{4} - j \left(\frac{\chi''_m}{2} + \frac{\chi''_e}{2} + \frac{\chi'_m \chi''_e}{4} + \frac{\chi''_m \chi'_e}{4} \right). \quad (\text{A.10})$$

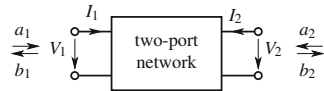
It shows the same symmetry properties for the real and imaginary part as (A.5) so that the Kramers–Kronig relation has to hold for the approximation of the refractive index:

$$\frac{k(\omega)}{k_0(\omega)} \approx 1 - \frac{j}{\pi} \oint_{-\infty}^{\infty} \frac{k(\Omega)/k_0(\Omega)}{\omega - \Omega} d\Omega. \quad (\text{A.11})$$

A.2 Relation Between Two-Port Parameters

Figure A.1 shows the port-currents and voltages as they are used for all two-port networks in this work. In the following, important relations between different matrix representations are summarized.

Fig. A.1 Definition of voltages and currents for a two-port network



A.2.1 Chain Parameters of a Transmission Line

The chain parameter matrix \mathbf{A} with the voltages and currents as defined in Fig. A.1 for a transmission line section of the length l follows

$$\begin{pmatrix} V_1 \\ I_1 \end{pmatrix} = \mathbf{A} \cdot \begin{pmatrix} V_2 \\ -I_2 \end{pmatrix} = \begin{pmatrix} \cosh \gamma l & Z_c \sinh \gamma l \\ \frac{1}{Z_c} \sinh \gamma l & \cosh \gamma l \end{pmatrix} \cdot \begin{pmatrix} V_2 \\ -I_2 \end{pmatrix}. \quad (\text{A.12})$$

A.2.2 Relation Between Transmission Line Parameters and Scattering Parameters

The generalized scattering parameters based on the definition of complex power waves [3–6]

$$a_i = \frac{V_i + Z_{0i} I_i}{2\sqrt{\text{Re}\{Z_{0i}\}}}, \quad (\text{A.13})$$

$$b_i = \frac{V_i - Z_{0i}^* I_i}{2\sqrt{\text{Re}\{Z_{0i}\}}} \quad (\text{A.14})$$

are calculated from the transmission line parameters by

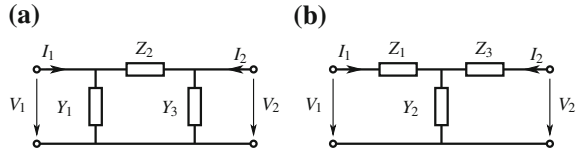
$$S_{11} = \frac{b_1}{a_1} = \frac{(Z_{02} - Z_{01}^*) \cosh(\gamma l) + \left(Z_c - \frac{Z_{01}^* Z_{02}}{Z_c}\right) \sinh(\gamma l)}{(Z_{01} + Z_{02}) \cosh(\gamma l) + \left(Z_c + \frac{Z_{01}^* Z_{02}}{Z_c}\right) \sinh(\gamma l)}, \quad (\text{A.15})$$

$$\begin{aligned} S_{12} = \frac{b_1}{a_2} = S_{21} = \frac{b_2}{a_1} \\ = \frac{2\sqrt{\text{Re}\{Z_{01}\}\text{Re}\{Z_{02}\}}}{(Z_{01} + Z_{02}) \cosh(\gamma l) + \left(Z_c + \frac{Z_{01}^* Z_{02}}{Z_c}\right) \sinh(\gamma l)}, \end{aligned} \quad (\text{A.16})$$

$$S_{22} = \frac{b_2}{a_2} = \frac{(Z_{01} - Z_{02}^*) \cosh(\gamma l) + \left(Z_c - \frac{Z_{01} Z_{02}^*}{Z_c}\right) \sinh(\gamma l)}{(Z_{01} + Z_{02}) \cosh(\gamma l) + \left(Z_c + \frac{Z_{01}^* Z_{02}}{Z_c}\right) \sinh(\gamma l)}. \quad (\text{A.17})$$

If not noted otherwise in this work, the reference impedance Z_{0i} is purely real so that the scattering parameters based on the power wave definition and the scattering parameters based on the traveling wave definition [7, 8] are equivalent.

Fig. A.2 Two-port circuit: **a** in Π -configuration, **b** in T-configuration



A.2.3 Two-Port Parameters of Circuits in Π - and T-Configuration

The unit cell configurations investigated in this work can be represented by a two-port circuit in Π - or T-configuration (Fig. A.2). They yield the impedance and admittance matrix

$$\begin{pmatrix} I_1 \\ I_2 \end{pmatrix} = \mathbf{Y}_\Pi \cdot \begin{pmatrix} V_1 \\ V_2 \end{pmatrix} = \begin{pmatrix} Y_1 + 1/Z_2 & -1/Z_2 \\ -1/Z_2 & 1/Z_2 + Y_3 \end{pmatrix} \cdot \begin{pmatrix} V_1 \\ V_2 \end{pmatrix}, \quad (\text{A.18})$$

$$\begin{pmatrix} V_1 \\ V_2 \end{pmatrix} = \mathbf{Z}_\text{T} \cdot \begin{pmatrix} I_1 \\ I_2 \end{pmatrix} = \begin{pmatrix} Z_1 + 1/Y_2 & 1/Y_2 \\ 1/Y_2 & 1/Y_2 + Z_3 \end{pmatrix} \cdot \begin{pmatrix} I_1 \\ I_2 \end{pmatrix}. \quad (\text{A.19})$$

and the chain parameter matrices

$$\mathbf{A}_\Pi = \begin{pmatrix} 1 + Z_2 Y_3 & Z_2 \\ -(Y_1 + Y_1 Z_2 Y_3) & 1 + Y_1 Z_2 \end{pmatrix}, \quad (\text{A.20})$$

$$\mathbf{A}_\text{T} = \begin{pmatrix} 1 + Z_1 Y_2 & Z_1 + Z_1 Y_2 Z_3 \\ Y_2 & 1 + Y_2 Z_3 \end{pmatrix}. \quad (\text{A.21})$$

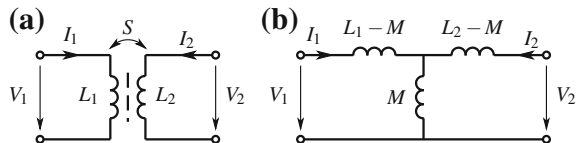
A.2.4 Two-Port Representation of a Transformer

A magnetic coupling between two inductors can be represented by the transformer with the coupling factor S in Fig. A.3a. The T-configuration of the transformer in Fig. A.3b takes the mutual inductance

$$M^2 = S^2 L_1 L_2 \quad (\text{A.22})$$

into account.

Fig. A.3 **a** Transformer with two coupled inductors. **b** T-configuration with the mutual inductance M



A.3 Photolithography Steps

In this work, different voltage tunable structures are manufactured on glass substrates. The main lithography steps, following the works [9–12], are:

- evaporation of NiCr and Au on glass substrate
- RF structure:
 - AZ4533 photo resist mask for Au plating: spin coat, softbake
 - exposure of mask for RF structure, development with AZ400K
 - hardbake (result: Fig. A.4a)
 - electroplating of Au
 - remove photo resist layer (result: Fig. A.4b)
- resistive biasing network:
 - AZ4533 photo resist mask for NiCr: spin coat, softbake
 - exposure of mask for bias lines, development with AZ400K
 - hardbake (result: Fig. A.4c)
- Selective wet etching:
 - Au etching
 - NiCr etching
 - remove photo resist layer
 - Au etching (result: Fig. A.4d)

If LC is used as tunable material, following steps are the processing and rubbing of the polyimide alignment layer and glueing of glass substrates to form the LC cavity.

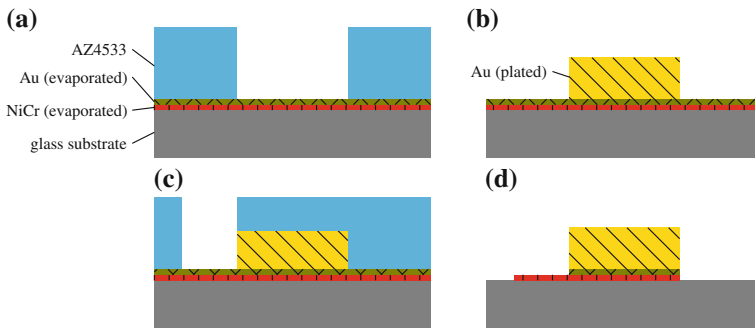


Fig. A.4 Glass substrates with Au and NiCr metallization after different manufacturing process steps: **a** photo resist for Au plating, **b** electroplated Au layer, **c** photo resist for etching of Au and NiCr, **d** final structure after wet etching

References

1. J.S. Toll, Causality and the dispersion relation: logical foundations. *Phys. Rev.* **104**, 1760–1770 (1956)
2. R.L. Weaver, Y.-H. Pao, Dispersion relations for linear wave propagation in homogeneous and inhomogeneous media. *J. Math. Phys.* **22**(9), 1909–1918 (1981)
3. D. Youla, On scattering matrices normalized to complex port numbers (1961)
4. K. Kurokawa, Power waves and the scattering matrix. *IEEE Trans. Microw. Theory Tech.* **13**(2), 194–202 (1965)
5. D. Frickey, Conversions between s, z, y, h, abcd, and t parameters which are valid for complex source and load impedances. *IEEE Trans. Microw. Theory Tech.* **42**, 205–211 (1994)
6. J. Freeman, On the interpretation of scattering parameters, Technical report, NASA Technical Reports Server, 1999
7. R.B. Marks, D.F. Williams, A general waveguide circuit theory. *J. Res.-Natl. Inst. Stand. Technol.* **97**, 533 (1992)
8. R.B. Marks, D.F. Williams, D. Frickey, Comments on conversions between s, z, y, h, abcd, and t parameters which are valid for complex source and load impedances [with reply]. *IEEE Trans. Microw. Theory Tech.* **43**(4), 914–915 (1995)
9. A. Mössinger, R. Marin, S. Müller, J. Freese, R. Jakoby, Electronically reconfigurable reflectarrays with nematic liquid crystals. *Electron. Lett.* **42**(1), 899–900 (2006)
10. F. Gölden, A. Gäbler, S. Müller, A. Lapanik, W. Haase, R. Jakoby, Liquid-crystal varactors with fast switching times for microwave applications. *Electron. Lett.* **44**(7), 480–481 (2008)
11. F. Gölden, Liquid crystal based microwave components with fast response times: material, technology, power handling capability, Ph.D. thesis, Technische Universität Darmstadt, Fachgebiet Mikrowellentechnik, June 2010
12. O.H. Karabey, Electronic beam steering and polarization agile planar antennas in liquid crystal technology, Ph.D. thesis, TU Darmstadt, Cham, 2014. Zugl. Darmstadt, Techn. Univ., Diss., 2013